Differential Cross Section Distributions and Polarization Observables in the Reaction $\vec{p}p \to pK^0\Sigma^+$ at $p_{\vec{p}} = 2.95$ GeV/c

Dissertation
zur
Erlangung des Doktorgrades (Dr. rer. nat.)
der
Mathematisch-Naturwissenschaftlichen Fakultät
der
Rheinischen Friedrich-Wilhelms-Universität Bonn

vorgelegt von
Roman Dzhygadlo
aus
Zhytomyr-11

Bonn, 2012

Angefertigt mit Genehmigung der Mathematisch-Naturwissenschaftlichen Fakultät der Rheinischen Friedrich-Wilhelms-Universität Bonn

1. Gutachter : Dr. habil. Albrecht Gillitzer

2. Gutachter : Prof. Dr. Kai-Thomas Brinkmann

Tag der Promotion: 27.09.2012

Erscheinungsjahr: 2012

Abstract

The reaction $\vec{p}p \rightarrow pK^0\Sigma^+$ was studied with the upgraded COSY-TOF detector. A polarized proton beam with momentum 2.95 CeV/c of the Cooler Synchrotron at Forschungzentrum Jülich was focused on a liquid hydrogen target. The $pK^0\Sigma^+$ final state was identified based on the analysis of the delayed decays of the strange hadrons $K_s \rightarrow \pi^+\pi^-$ and $\Sigma^+ \rightarrow p\pi^0$, $n\pi^+$. The azimuthal symmetry and large acceptance of the detector as well as the excellent tracking capability provided by the silicon quirl and straw tube tracking subdetectors allows measuring the complete $pK^0\Sigma^+$ final state distribution.

To achieve the best possible precision in the reconstruction of the track parameters the whole detector setup was calibrated in iterative procedure. The experiment conditions, namely the target dimension and beam polarization where determined based on the analysis of pp elastic scattering events.

Two new reconstruction algorithms of the reaction $\vec{p}p \rightarrow pK^0\Sigma^+$ were developed. The combination of these two algorithms yield a reconstruction efficiency $\varepsilon_{reco} = 0.027 \pm 0.001$ which is more than two times better than that of previous COSY-TOF measurements.

All reconstruction and analysis algorithms were controlled by Monte Carlo simulations. The existing simulation software was extended by implementing the new subdetectors and by adding detector inefficiencies to obtain a more realistic detector response. An interface for EvtGen as an alternative particle generator was added to gain more flexibility in the generation of angular distributions.

A new COSY-TOF analysis framework was developed. It incorporates the best features of modern analysis frameworks and allows for straightforward implementation of reconstruction and analysis algorithms.

From about one week of data taking 905 events of the reaction $\vec{p}p \rightarrow pK^0\Sigma^+$ were reconstructed. The fraction of background in this data sample is estimated to be at most 5.9%. Based on this, the total cross section of the reaction $\vec{p}p \rightarrow pK^0\Sigma^+$ was determined to be $\sigma = (2.95 \pm 0.11_{stat} \pm 0.22_{syst})\ \mu b$.

From the analysis of the $pK^0\Sigma^+$ Dalitz plot it is concluded that the N(1710) P_{11} resonance significantly contributes to the production mechanism. A strongly attractive $p\Sigma^+$ final state interaction is excluded.

The polarization of the Σ^+ hyperon is determined to be positive as a function of the transverse momentum p_t. For the first time the analyzing power A_N and the spin transfer coefficient D_{NN} of the Σ^+ hyperon are determined. The analyzing power A_N has sine-like dependence of $\cos\theta^*_{\Sigma^+}$ with an amplitude of $(34 \pm 13)\%$. The spin transfer coefficient is found to be compatible with zero at large Σ^+ backward center-of-mass momentum $x_f < 0$ while at large Σ^+ forward center-of-mass momentum $x_f > 0$ it is $+1$ within the errors.

Contents

Chapter 1

Introduction

1.1 Structure of Matter

Based on current knowledge all matter is made of microscopic constituents which are either quarks or leptons. Both of them have spin 1/2 and thus are fermions. It is assumed that they are elementary and point like particles. The fundamental forces between these constituents are carried by gauge bosons with spin 1. The carriers of

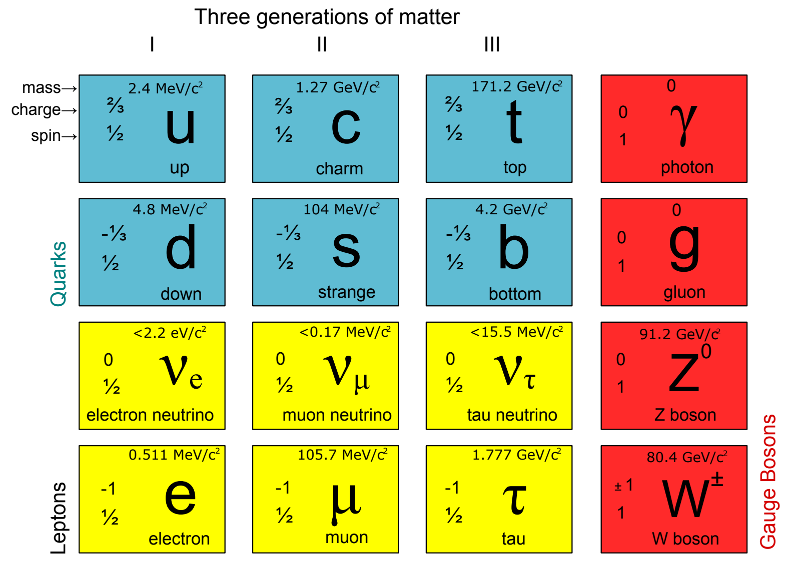

Figure 1.1 – The Standard Model of particle physics. Quarks are shown in light blue, leptons in yellow and gauge bosons in red.

the electroweak interaction are the photon γ and the $W^{\pm}$ and Z^0 bosons, whereas the carrier of the strong interaction is the gluon g. This is called the Standard Model of particle physics as illustrated in Fig. 1.1. Gravitation is not included in this model. Apart from spin the particles are classified by electric charge and color charge, baryon number and lepton number, quark flavor and lepton flavor. The matter constituents can be grouped into three generation which are represented by the first three columns in Fig. 1.1. The stable matter around us is only built from constituents of the first column.

Each elementary fermion has its antiparticle which is characterized by quantum numbers with opposite sign, except for the spin. Also the intrinsic parity of fermion and antifermion have opposite sign. Free quarks, antiquarks and gluons are not observed, but they are confined inside hadrons. Quarks can have three different values of color charge, but all observed hadrons are color neutral. Therefore, the minimum quark content of hadrons can only be quark-antiquark, which are called mesons, or three quarks, which are called baryons. It was found that the baryons made of the lightest three quarks flavors (u, d, s) obey a certain symmetry which is called SU(3) flavor symmetry. According to this symmetry ground state baryons can be grouped into an octet and into a decuplet, as shown in Fig. 1.2.

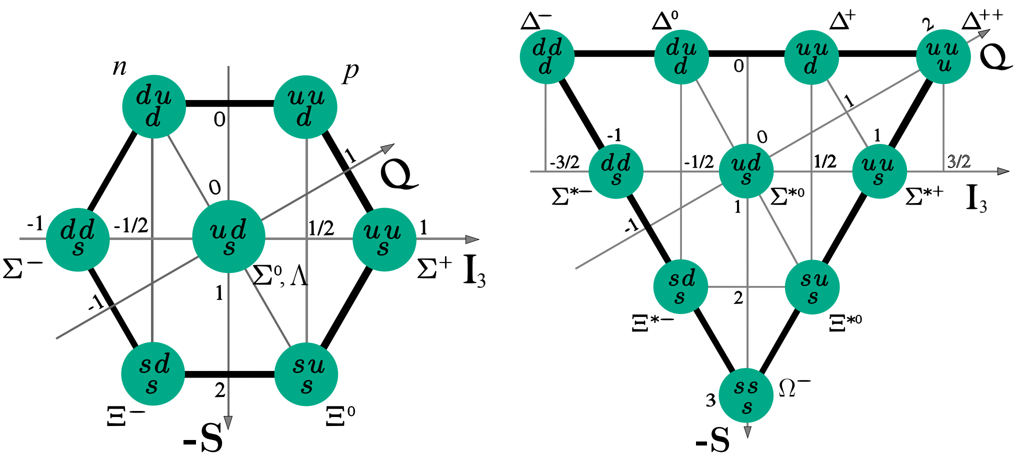

Figure 1.2 – SU(3) baryon octet (left) and decuplet (right). The x axis represents the third component of the isospin I_3 and the y axis represents the strangeness.

The baryons and mesons which contain s-quarks are called hyperons and K-mesons respectively. They can be produced in the strong interaction only via associated production in which each hadron in the final state has either strangeness or antistrangeness.

This is due to strangeness conservation in the strong interaction. The reaction investigated in this work is a good example:

$$\begin{array}{rccccc} & p + p & \to & N + & K + & Y \\ S = & 0 \quad 0 & & 0 & 1 & -1 \end{array} \tag{1.1}$$

where Y is either a Λ or Σ hyperon. The Λ is an isospin singlet state whereas the Σ is an isospin triplet. As a consequence, the spin orientation of the two light quarks is antiparallel in the Λ and parallel in the Σ.

The mechanism of strangeness production will be discussed in next section. The decay of strange particles proceeds via the weak interaction. Therefore, these particles have a long life time and do not decay at their production point. Since parity is not conserved in weak decays the angular distribution of the daughter nucleon has an asymmetry with respect to the spin orientation of the decaying hyperon. This can be used to measure the polarization of the hyperon (Sec. 1.3).

1.2 Production Mechanism of the $pp \to pK^0\Sigma^+$ Reaction

The mechanism of strangeness production in nucleon-nucleon collisions is still not understood. Existing models are grouped in two categories depending on the energy regime considered. At high energies the quark-gluon degrees of freedom are important and therefore quark models which take into account different elementary processes such as quark-quark and quark-gluon scattering, quark-antiquark pair annihilation, or gluon fusion are more applicable. However, at low energies close to the production threshold hadron degrees of freedom are relevant, and meson exchange models are more successful. Part of the considerations below applies to the more general case of the reaction $pp \to NKY$, but since the present work focuses on the $pK^0\Sigma^+$ final state, this reaction is discussed in the following.

1.2.1 Meson exchange models

In 1960 Ferarri [1] proposed kaon and pion exchange as mechanism for strangeness production in nucleon-nucleon collisions. Later this approach was extended by incorporating in addition the non-strange mesons η, σ, ρ and ω as well as the strange mesons K^* and K_1 [2], [3]. Separating the contribution of all individual channels is required to understand strangeness production; however, it was found in several studies [2], [4],

[5], [6] that it is not even possible to unambiguously separate the contribution from strange and from non-strange meson exchange on the basis of the existing data. It also was shown in Refs. [7], [8], [9] that to reproduce the existing experimental data kaon exchange may not be necessary.

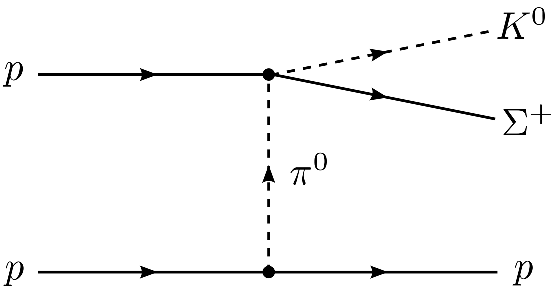

Figure 1.3 – π exchange.

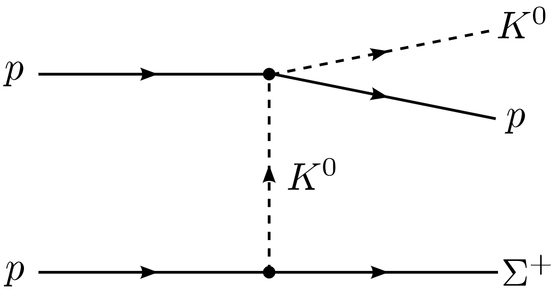

Figure 1.4 – K exchange.

Fig. 1.3 and Fig. 1.4 shows Feynman diagrams of pion and kaon exchange. Both of them can be also interpreted in terms of quark lines as shown in Fig. 1.5 and Fig. 1.6 for completeness.

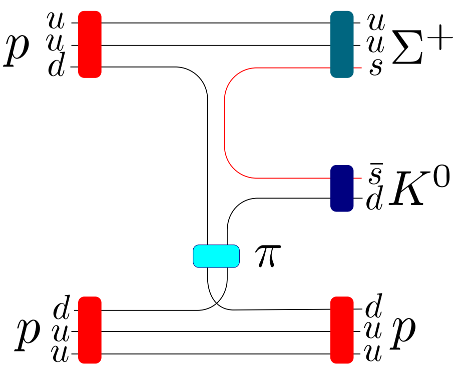

Figure 1.5 – π exchange.

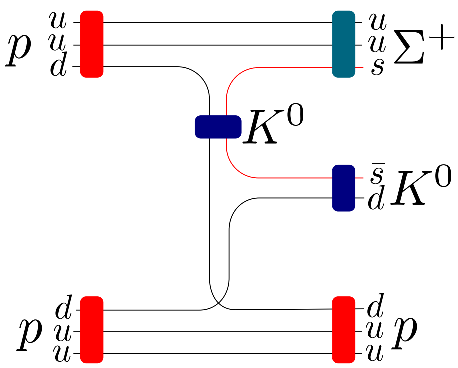

Figure 1.6 – K exchange.

Considering pion exchange the total cross section of the reaction $pp \to pK^0\Sigma^+$ can be obtained by integrating differential the differential cross section over phase space [10]:

$$\sigma = \frac{m_N^2}{2\pi^2 q_i^2 s} \int_{W_{min}}^{W_{max}} k\, W^2\, \sigma(\pi N \to KY, W)\, dW \int_{t_{min}}^{t_{max}} \frac{f_{NN\pi}^2}{\mu^2}\, F^2(t)\, D^2(t)\, t\, dt \quad (1.2)$$

where $\sqrt{s}$ and W are the invariant masses of the colliding protons and the produced kaon-hyperon system, respectively, and t stands for the squared four-momentum transfer from the initial to the final nucleon. $D(t)$ is the pion propagator, defined as

$D(t) = 1/(t - \mu^2)$ with μ being the pion mass. $f_{NN\pi}$ is the renormalized $NN\pi$ coupling constant which is related to the coupling constant by $f_{NN\pi} = g_{NN\pi}(\mu/2m_N)$. The monopole form factor $F(t)$ is used to account for off-shell modification and it is defined through the cut-off parameter Λ_π as $F(t) = (\Lambda_\pi^2 - \mu^2)/(\Lambda_\pi^2 - t)$.

Reference	$g^2_{N\Lambda K}$	$g^2_{N\Sigma K}$
Martin [11]	13.9 ± 2.6	3.3 ± 1
McGinley [12]	9.0	1.5
Dalitz [12]	20.7	1.0
Laget [2]	14	1
Sibirtsev [13]	19.6 ± 4.2	1.3 ± 0.3

Table 1.1 – Coupling constants from different studies. Collected by Ref. [13].

Similarly the cross section can be deduced for kaon exchange which is then defined by the g_{NYK} coupling constant. The value of g_{NYK} for Λ and Σ production from different studies is shown in Tab. 1.1. As we can see, the contribution of strange meson exchange is much larger for Λ hyperon production.

1.2.2 Resonance model

In previous studies of the reaction $pp \to pK^+\Lambda$ by COSY-TOF [14], [15] the Dalitz plot clearly shows the presence of N^* resonances. The contribution of N^* to hyperon production is taken into account in the so-called resonance model [16]. According to this model strangeness production in the $NN \to NYK$ reaction could be understood in terms of non-strange meson exchange followed by the excitation of an intermediate nucleon resonance as shown in Fig. 1.7. In Ref. [10] a method was proposed to distinguish

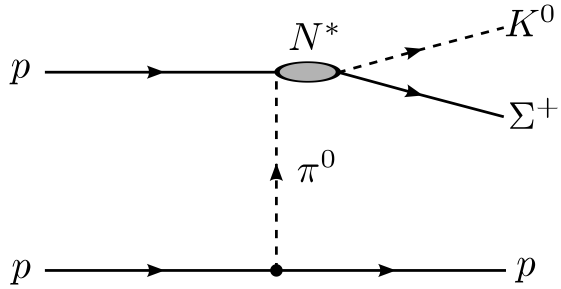

Figure 1.7 – Feynman diagram according to the resonance model.

the dominant meson exchange experimentally by reconstructing the invariant mass distribution of the hyperon-nucleon system. There it was shown that at low energies kaon exchange results in a final state distribution very close to an isotropic phase-space distribution. This allows to distinguish strange and non-strange meson exchange. In the latter case a deviation from an isotropic distribution indicates a contribution from nucleon resonance excitation.

In Ref. [3] different Σ production reactions $NN \to N\Sigma K$ were studied with the same one-meson exchange model as in Refs. [16], [9], [10], which includes π, η and ρ meson exchange (see Fig. 1.8).

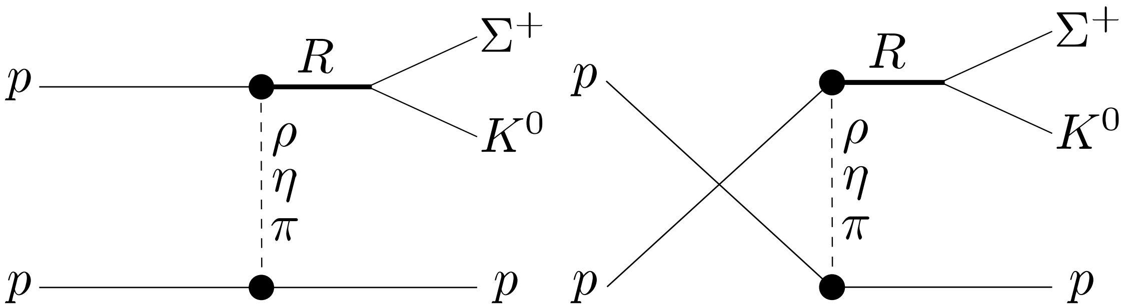

Figure 1.8 – Feynman diagrams taken into account in the calculation of Sibirtsev [3].

In Fig. 1.8 according to Ref. [3] R denotes the nucleon resonances $N(1710)$ P_{11}, $N(1720)$ P_{13}, $\Delta(1920)$ P_{33} for which the observation of decays to ΣK had been claimed.

From the experimental decay branching ratios of these resonances to πN, ηN and ρN the relevant coupling constants were calculated. The result showed the dominant contribution from the $N(1710)$ P_{11} resonance. In Fig. 1.9 the contribution of different resonances to the reaction $pp \to p\Sigma^0 K^+$ is shown.

A crucial question is the sensitivity of the results to the coupling constants and cut-off parameters which cannot be fixed solely from the experimental data within the model.

1.2.3 Final state interaction

The understanding of the YN interaction is needed to extend our knowledge of SU(3) flavor symmetry breaking of QCD and of the hypernuclei formation mechanism. Also the equation of state of nuclear matter is significantly constrained to the presence of

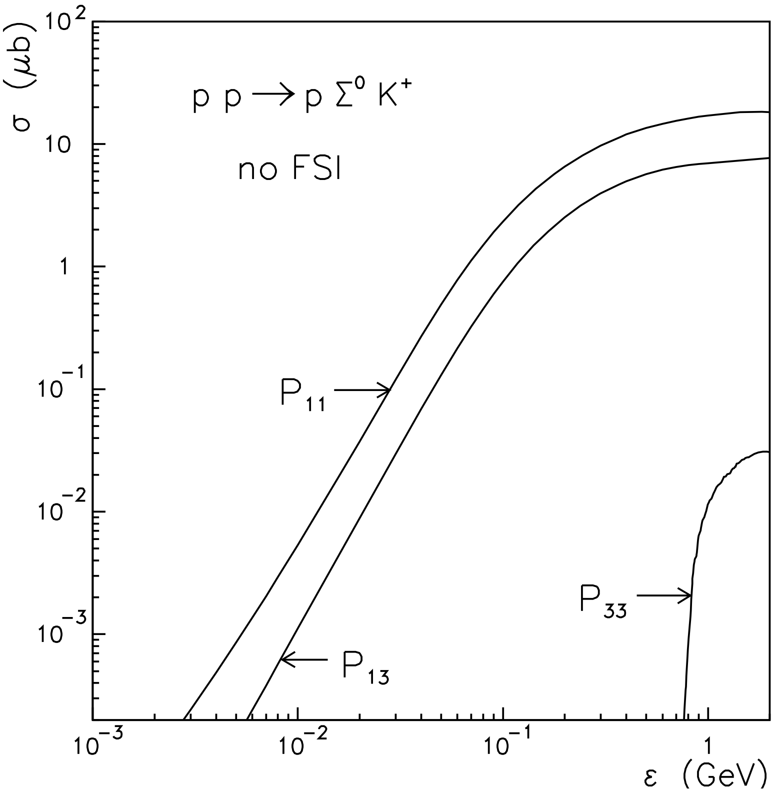

Figure 1.9 – Contribution of the different resonances, $N(1710)$ P_{11}, $N(1720)$ P_{13} and $\Delta(1920)$ P_{33}, to the $pp \to p\Sigma^0 K^+$ total cross section as a function of CMS energy above the threshold. Figure from Ref. [10].

hyperons, thus the YN interaction can help to understand the structure of neutron stars [17].

The study of $p\Sigma^+$ final state interaction (FSI) is especially interesting since within strict SU(3) flavor symmetry, it is generated by exactly the same mechanism as the $^1S_0$ interaction in the np system [18]. Therefore, differences in the corresponding FSI are directly related to effects of SU(3) breaking.

1.3 Hyperon Polarization

During the past decades a significant amount of hyperon and antihyperon polarization data has been collected in mostly inclusive experiments at high energies. Many theoretical models have been proposed and discussed [19]. None of them is able to explain the observed hyperon polarization phenomena consistently. Below two models are summarized which try to give a simple explanation for the polarization effects.

1.3.1 The Lund model

If one assumes that the Λ hyperon is described by a *uds* three-quark wave function based on SU(6) spin-flavor symmetry in which the *ud* diquark system is in a spin-isospin singlet state, then the Λ polarization is purely defined by the s quark. In the Lund model [20] an incoming *ud* system with spin S=0 and isospin I=0, stretches the confined color field in the collision region to produce a $s\bar{s}$ pair. Part of the momentum transfer to the Λ is provided by the s quark which has to be compensated by the $\bar{s}$ antiquark. Therefore, due to the finite extension the $s\bar{s}$ pair has orbital angular momentum which is assumed to be compensated by the spin of the $s\bar{s}$ pair. As a result of this consideration one expects a negative Λ polarization which is increases with Λ transverse momentum p_t. In the Σ hyperon consisting of two light quarks (*uu*, *ud*, *dd*) and one strange quark, the two light quarks are in an $I = 1$, $S = 1$ state, and thus the polarization is expected to be opposite to the that of the Λ. This result is in agreement with the experimental data. However, considering s and $\bar{s}$ quarks moving in opposite directions and observing the final state $K^+\Lambda$, where the direction of the K^+ meson is defined by the $\bar{s}$, one should expect that the Λ polarization is non zero only when K^+ and Λ are in opposite hemispheres. The E766 experiment at BNL has made exclusive measurements of the $pp \rightarrow p\Lambda K^+\pi^+\pi^-\pi^+\pi^-$ reaction at 27.5 GeV/c beam momentum [21] but found no correlation between the K^+ momentum direction and the Λ polarization.

1.3.2 The recombination model

In the recombination model [22] the Λ is also created by recombination of a fast *ud* diquark from the proton with a slow s quark from the sea. With $\vec{F}$ being the unspecified color force, the s quark of velocity $\vec{v}$ feels the effect of the Thomas precession given by $\vec{\omega}_t \simeq \vec{F} \times \vec{v}$, which has its direction along the normal vector of the production plane ($\vec{n} \propto \vec{p}_{beam} \times \vec{p}_\Lambda$). To minimize the energy $\vec{S} \cdot \vec{\omega}_t$, the spin $\vec{S}$ of the s quark must be opposite to $\vec{\omega}_t$, this leads to negative Λ polarization in $pp \rightarrow \Lambda X$, which is in agreement with experiment.

The biggest problem of this model is that it predicts the analyzing power and depolarization to be zero which is in strong contradiction to the experimental results [23], [24], [25], [26].

1.4 Experimental Observables in Σ^+ Production Experiments

1.4.1 Total cross section

The most obvious measurable quantity to test the validity of models for Σ^+ production is the total cross section σ. Fig. 1.10 shows a compilation of existing total cross section data for the reaction $pp \to pK^0\Sigma^+$. These data were obtained in bubble chamber [27] (black squares) and in recent COSY-TOF [28] (red triangles) experiments.

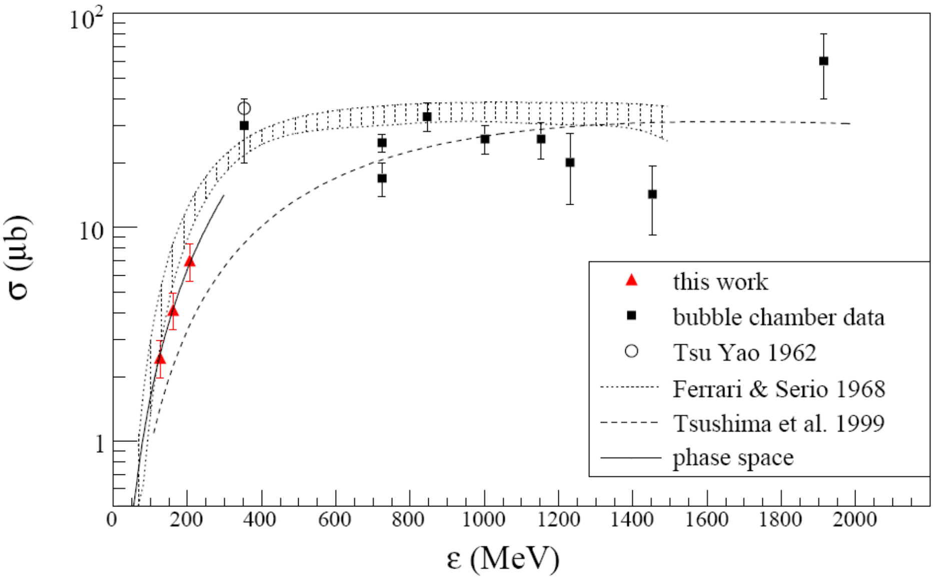

Figure 1.10 – Total cross sections of the reaction $pp \to pK^0\Sigma^+$. The triangles at low excess energies represent previous COSY-TOF measurements [28]. The solid square symbols are from bubble chamber experiments (compiled in Ref. [27]). The curves are explained in the text. Figure from Ref. [28].

The early (1968) calculations of Ferrari and Serio [29] are shown by the shaded area. In this calculations various $pp \to NKY$ channels were studied within the boson exchange model without taking into account nucleon resonances. Pure pion exchange is indicated by the lower limit of the shaded area while its upper limit corresponds to the maximum additional contribution by kaon exchange with a coupling constant of 1.6. The dashed line represents the result of the resonance model calculation of Ref. [30] (see Sec. 1.2.2) in which the hyperon channels ($pp \to pK^+\Lambda$, $pK^+\Sigma^0$, $pK^0\Sigma^+$) were investigated with common coupling constants and cut-off values. The solid line indicates an excitation function corresponding to pure s-wave phase space, normalized to the data.

1.4.2 Dalitz plot

The Dalitz plot [31] provide a possibility to extract information on the reaction mechanism. The presence of N^* resonances in the process as well as final state interaction will result in deviation from a uniform phase-space distribution.

Fig. 1.11 shows the $pK^0\Sigma^+$ Dalitz plot obtained in the previous COSY-TOF measurement with unpolarized proton beam at $p_{beam} = 3.059$ GeV/c [28].

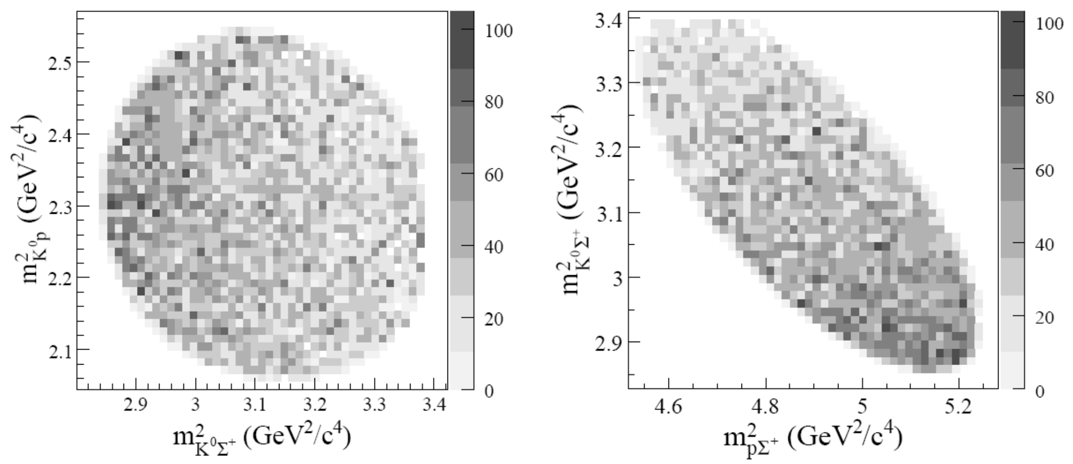

Figure 1.11 – Acceptance corrected Dalitz plot from a previous COSY-TOF measurement at $p_{beam} = 3.059$ GeV/c [28].

In the Dalitz plot no narrow structures due to nucleon resonances or due to final-state-interaction are observed.

1.4.3 Σ^+ polarization

Polarization of Σ^+ hyperons has been observed in inclusive measurements at high energies. Starting from 1983 at Fermilab a series of experiments was performed measuring the Σ^+ polarization with different targets and beam momenta [32], [33] as shown in Figs. 1.12 and 1.13. From the analysis of the data it was concluded that the Σ^+ polarization increases with transverse momentum p_t from zero up to a maximum of 0.16 at about 1.0 GeV/c [34]. For higher p_t the polarization decreases with p_t.

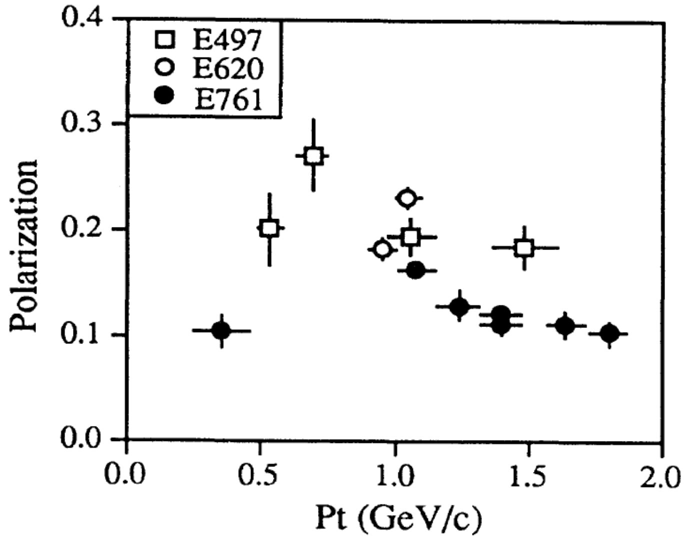

Figure 1.12 – Polarization of the Σ^+ as a function of transverse momentum p_t at 800 GeV/c proton beam momentum (E761) and at 400 GeV incident proton energy (E497, E620). E620 used a Be target, E497 and E761 used a Cu target. Figure from Ref. [33].

Perturbative QCD predicts zero polarization at high momentum transfer [39], [40]. However, no model is able to predict at which transverse momentum p_t the polarization will start to decrease. The polarization at 400 GeV is higher than at 800 GeV proton beam energy. The polarization obtained with a Be target is higher than obtained with a Cu target.

Fig. 1.14 shows the Σ^+ polarization measured in the reaction $\gamma p \to K^0\Sigma^+$ at E_γ = 1.30 GeV.

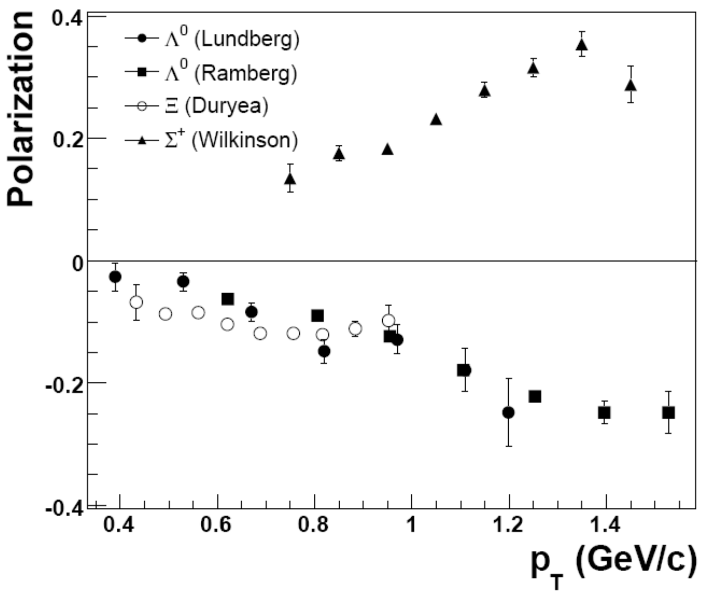

Figure 1.13 – Σ^+ polarization from Ref. [32] compared to Λ [35], [36] and Ξ [37] polarization. Figure from Ref. [38].

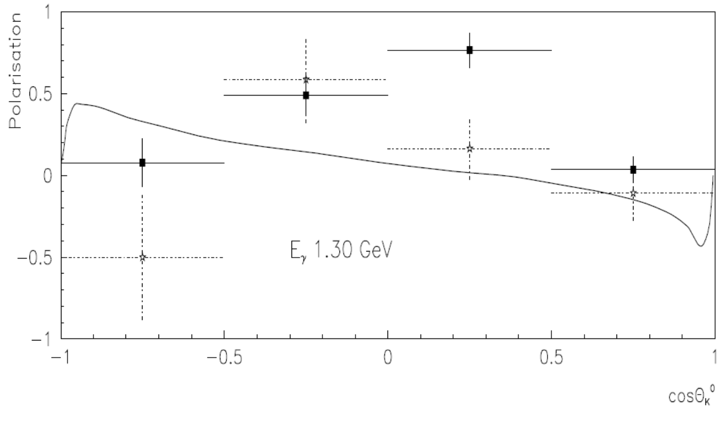

Figure 1.14 – Σ^+ polarization measured in the reaction $\gamma p \to K^0\Sigma^+$ at $E_\gamma = 1.30$ GeV. Black rectangles [41] and stars [42] are the results of measurements with the SAPHIR detector at ELSA. Solid line indicate model calculation from Ref. [43]. Figure from Ref. [41].

1.4.4 Spin transfer coefficient D_{NN}

Experiments with polarized beam provide additional observables, like analyzing power A_N and spin transfer coefficient (depolarization) D_{NN}. D_{NN} is particularly sensitive to the production mechanism. Within the Laget model [2] it provides distinct results

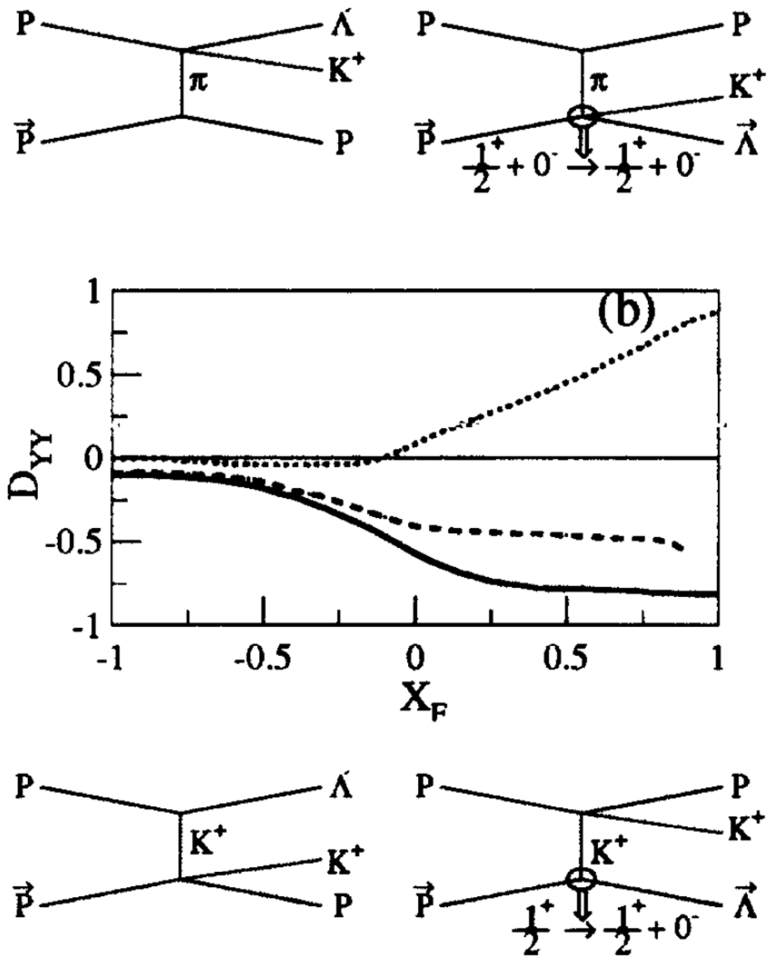

Figure 1.15 – The middle part represents the model calculation of Laget [2] for the spin transfer in the reaction $\vec{p}p \to pK^+\Lambda$ based on pion and kaon exchange. The upper and lower parts show the Feynman diagrams for pion and for kaon exchange, respectively. Figure from Ref. [44]

.

for strange and nonstrange meson exchange in the forward region.

The middle part of Fig. 1.15 shows D_{NN} of the reaction $\vec{p}p \to pK^+\Lambda$ as a function of the Feynman variable x_f for different meson exchange channels. The solid and dotted lines correspond to pure kaon and pion exchange, respectively. The dashed line denotes a mixture of both mechanisms.

In the forward region (positive x_f) the hyperon is preferably correlated with the polarized beam proton. Hence, in the case of kaon exchange, angular momentum and parity conservation at the polarized proton vertex (lower right diagram) require a spin flip leading to $D_{NN} \simeq -1$. Pion exchange (upper right diagram) ensures conservation of both quantities without spin flip, hence $D_{NN} \simeq 1$. The same arguments can be applied to the reaction $\vec{p}p \to pK^0\Sigma^+$ as shown in Fig. 1.16.

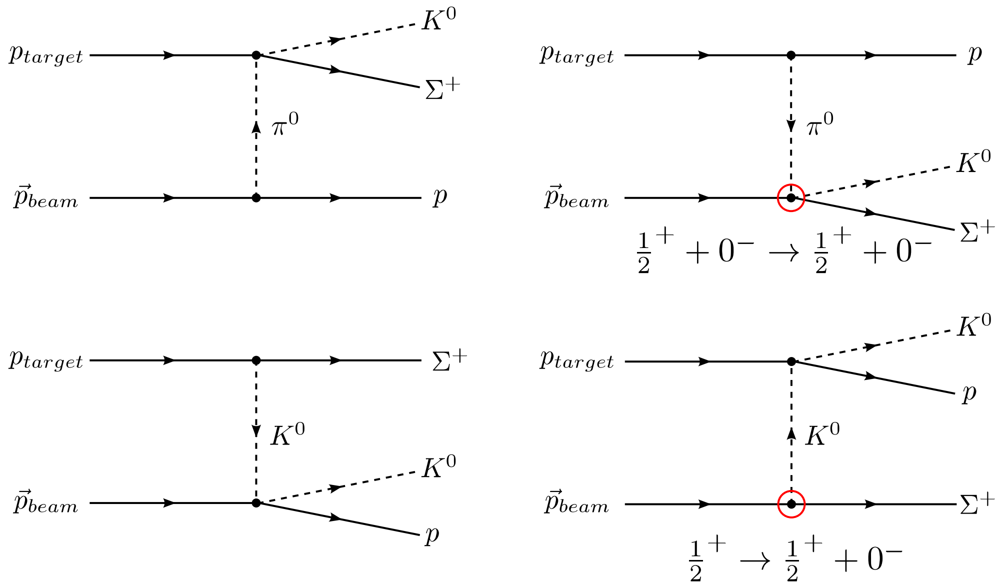

Figure 1.16 – Model for the depolarization value in the reaction $\vec{p}p \to pK^0\Sigma^+$ in case of pion (upper) and kaon (lower) exchange. The left and right diagrams correspond to negative and positive x_f, respectively.

In the backward region (negative x_f) the depolarization is predicted to tend towards zero for both mechanisms as in this case the hyperon is more connected with unpolarized target (left diagrams in Fig. 1.15 and Fig. 1.16).

1.5 Strangeness Production at COSY-TOF

The physics program of the COSY-TOF experiment [45] focuses on the associated production of Λ, Σ^0 and Σ^+ hyperons together with K^+ or K^0 mesons in proton-proton or proton-deuteron collisions. The concept of the detector allows for complete event reconstruction based on geometrical information. Additional constrains can be applied by using the time-of-flight measurement. Due to the large acceptance of the detector setup in most cases full phase space of the primary reaction products is covered. Thus, all differential distributions can be measured.

The first measurements of COSY-TOF were performed with unpolarized beam for the reaction $pp \rightarrow pK^+\Lambda$ at 2.50 GeV/c and 2.75 GeV/c beam momentum. The resulting differential cross-sections, $pK^+\Lambda$ Dalitz plot and Λ polarization are presented in Ref. [14]. Result of further measurements at 2.59 GeV/c, 2.68 GeV/c and 2.85 GeV/c are presented in Ref. [15]. Λ production at higher momenta 2.95 GeV/c, 3.059 GeV/c, 3.20 GeV/c and 3.30 GeV/c is presented in Refs. [46], [47], [48].

Additional measurements at 2.95 GeV/c, 3.059 GeV/c and 3.20 GeV/c were performed simultaneously for the reactions $pp \rightarrow pK^+\Lambda$ and $pp \rightarrow pK^+\Sigma^0$ [49].

Dedicated studies of the reaction $pp \rightarrow pK^0\Sigma+$ were performed at 2.95 GeV/c, 3.059 GeV/c and 3.20 GeV/c beam momentum [28], [50], [51], [52], [53].

The first measurements with polarized proton beam at 2.75 GeV/c and 2.95 GeV/c were performed to study the reaction $\vec{p}p \rightarrow pK^+\Lambda$, resulting in analyzing power and depolarization of the Λ hyperon [54].

The resent measurement at 2.95 GeV/c momentum with polarized proton beam using the upgraded COSY-TOF detector allows studying the final state interaction, polarization variables and differential distributions in the reaction $\vec{p}p \rightarrow pK^+\Lambda$ with better resolution [26]. In the current work this data set is analyzed to investigate the reaction $\vec{p}p \rightarrow pK^0\Sigma^+$. The azimuthal symmetry and large acceptance of the detector as well as the excellent tracking capability introduced by the recently installed silicon quirl and straw tube trackers allows measuring the complete $pK^0\Sigma^+$ final state distribution. The polarized proton beam allows measuring for the first time the analyzing power and depolarization of the Σ^+ hyperon.

Chapter 2

Experimental Setup

In this chapter the experimental setup is described. In particular the specific properties of the COSY-TOF detector and its advantages for the detection of hyperons are pointed out.

2.1 COoler SYnchrotron

The experiment was performed at the COoler SYnchrotron [55] at Forschungzentrum Jülich in Germany. The general layout of the accelerator complex is shown in Fig. 2.1,

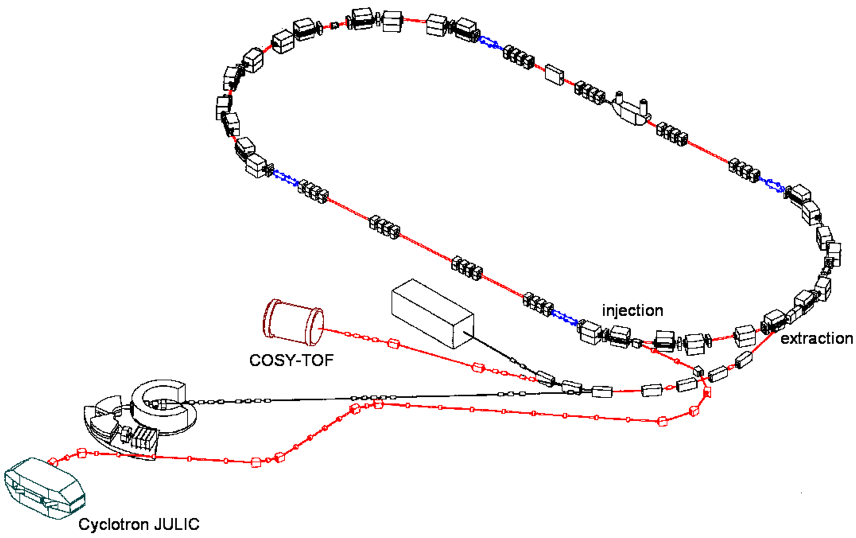

Figure 2.1 – Schematic view of the COSY accelerator.

where the path of the beam protons from the cyclotron JULIC as preaccelerator to the target of the COSY-TOF experiment is highlighted with red.

Negatively ionized hydrogen (H^-) is accelerated by the Cyclotron JULIC up to an energy of 40 MeV where it passes through a strip foil in order to remove the electrons. The resulting protons are accelerated in the 184 m circumference COSY ring to 2.95 GeV/c momentum for this experiment. The time required to accelerate protons is about 2 sec. An additional time of 10 sec is required for electron cooling. In total up to $2 \cdot 10^{11}$ transversely polarized protons can be stored in the ring. Due to the electron and stochastic cooling systems, the momentum deviation of the beam is improved to the order of $\Delta p/p < 10^{-4}$ and a beam divergence better than 2 mrad is achieved. After the beam is cooled down to equilibrium phase space density, it is extracted from the ring by the stochastic method and transported to the COSY-TOF detector. The extraction time can be varied. For this experiment it was adjusted in a way to obtain spills of about 10^6 particles per second. This corresponds to a typical spill length of 120 sec. To minimize time dependent asymmetries in the determination of polarization observables the spin of the beam was flipped every spill.

2.2 Detector Setup

COSY-TOF is a time-of-flight detector consisting of a tank of 3.5 m length and 3 m diameter (Fig. 2.2). To decrease the rate of secondary interactions and multiple scattering processes the tank is evacuated to $5 \cdot 10^{-3}$ mbar residual pressure. The material budget of all subdetectors is also reduced to the minimum possible value. The sensitive area of the detector covers the full azimuthal range and polar angles from 2° to 60°. For most hyperon production reactions this corresponds to full 4π acceptance in the center of mass frame (CMS). Apart from that, it has excellent tracking capability, in particular close to the interaction point.

COSY-TOF is a modularized detector consisting of several subdetectors which are organized in three logical units: time-of-flight (TOF), tracking systems and calorimeter.

2.2.1 Time-Of-Flight system

The TOF system consists of the start counter located 1.6 cm behind the target and the stop counter which covers the inner surface of the cylindrical wall and the downstream end cap of the tank.

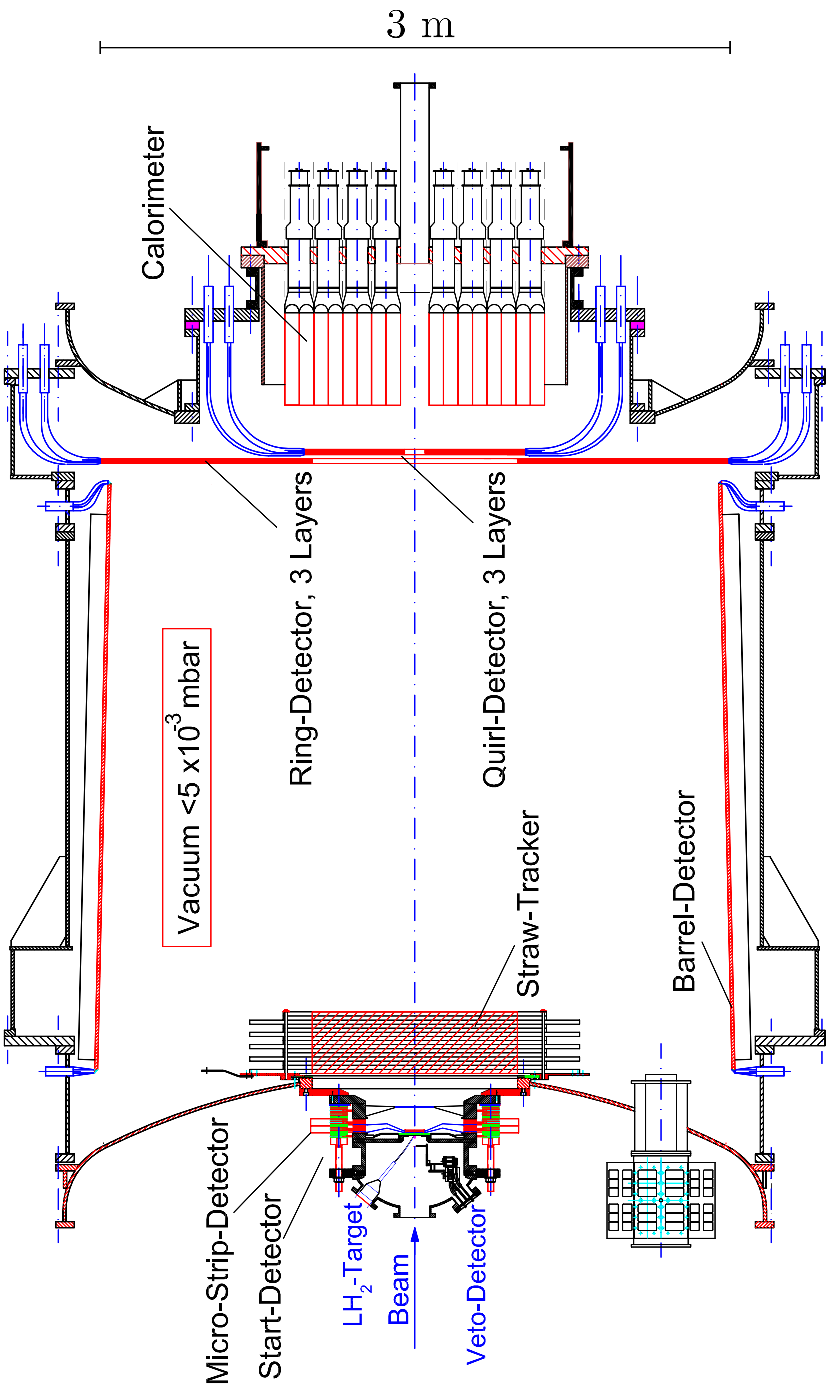

Figure 2.2 – Schematic view of the COSY-TOF detector. Figure from Ref. [56]

The start counter provides the start signal for the time-of-flight measurement. It consists of two scintillator discs of 1 mm thickness each with an outer diameter of 152 mm and an inner hole of 2.8 mm diameter. Each of the disks is segmented into 12 wedge-shaped sectors. The second disk is rotated with respect to first one by 15° around the beam axis. For a valid start signal a coincidence of two signals from partially overlapping sectors of front and backward discs is required.

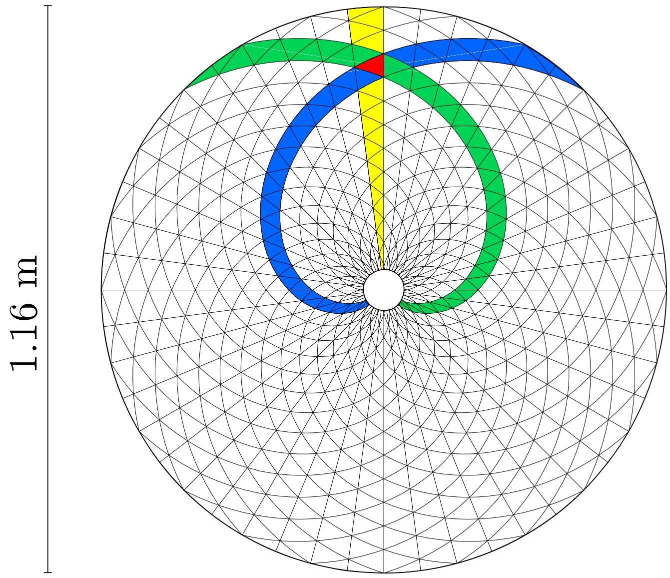

Figure 2.3 – Schematic view of Quirl. The red triangle is an example of a hit created by the combination of signals from different Quirl elements. The colored strips belong to different scintillator discs.

The part of the stop counter which covers the inner cylindrical surface of the tank, the Barrel Counter, consists of 96 scintillators bars of 2.8 m length and 15 mm thickness. The forward part covering the end cap consists of two subdetectors, Quirl and Ring. Both of them are composed of three segmented scintillator discs of 5 mm thickness each. The Quirl with an outer diameter of 1.16 m has 48 straight wedges and 2×24 Archimedian spirals bent in left and right directions for different layers as shown in Fig. 2.3. The Ring with outer diameter 3 m has 96 wedges and 2×48 Archimedian spirals.

As stop signal a coincidence of three signals from three discs of Quirl or Ring or a signal from the Barrel counter is required.

The resulting momentum resolution achieved based on the time-of-flight measure-

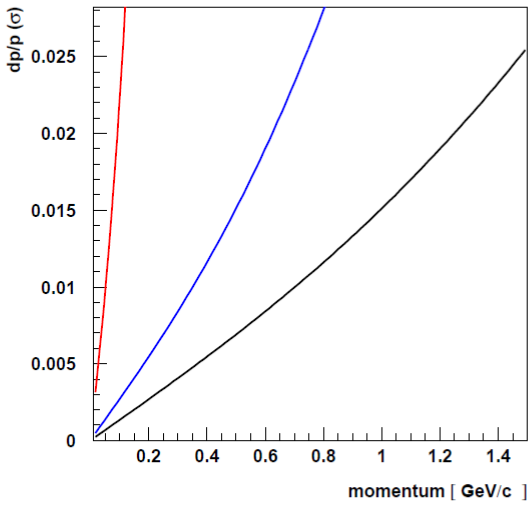

Figure 2.4 – Momentum resolution of single tracks archived by the time-of-flight measurement as a function of the particle momentum; red: pions, blue: protons, black: deuterons.

ment as a function of the particle momentum is shown in Fig. 2.4 for pions, protons, and deuterons.

2.2.2 Tracking system

2.2.2.1 The Silicon Quirl Tracker

The Silicon Quirl Tracker (SQT) [57] is located 2.6 cm behind the target and is the first subdetector providing tracking information. It is designed to measure the hit position and the energy loss of charged particles. The SQT is a segmented silicon wafer of 300 μm thickness which is mounted on an annular frame together with 16 preamplifiers blocks (Fig. 2.6). The sensitive area is a P-I-N type semiconductor with outer diameter of 70 mm and central hole of 5.5 mm diameter. The diameter of the central hole was chosen in such a way that it is large enough to avoid interactions of the beam with the SQT. The segmentation of the active area is achieved by dividing each side of the wafer into 256 Archimedian spirals. In the present configuration, however, only every second element is directly connected to the read-out. Each of the spirals covers an angular range of π, neglected the area of central hole. The small distance between the segments of 10 μm achieved by using the technique of plasma-etching, which induces only a negligible loss of active area. Because the bending directions of the spirals on

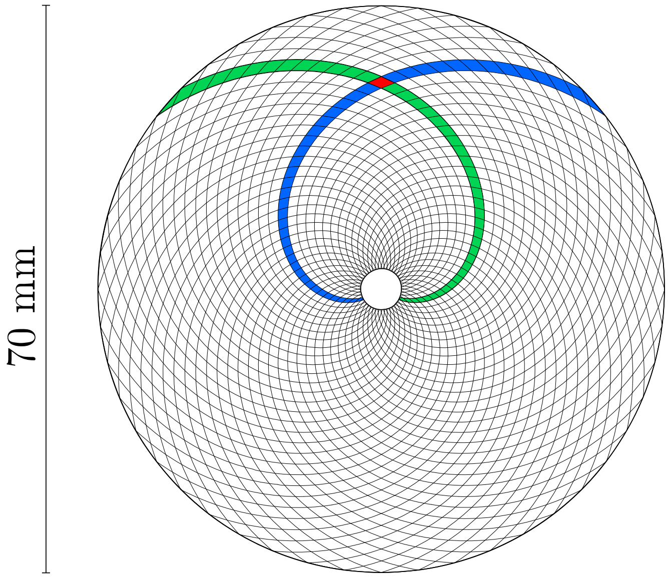

Figure 2.5 – Schematic view of the SQT. For clearness only 96 spirals are shown. The red diamond identify the hit position by combination of signals from two Archimedian spirals. The colored spirals belong to different sides of the SQT.

the front and the back sides are opposite to each other, each spiral on one side has exactly one crossing point with any spiral on other side as shown in Fig. 2.5.

Figure 2.6 – Photo of the Silicon Quirl Tracker (SQT). On the left side the SQT including the outer mounting frame and the preamplifier boxes is shown. The right side shows the inner part with silicon wafer, inner support ring, and read-out cables.

All spiral elements cover an identical amount of solid angle with the identical range in polar angle. Due to this, dead time effects do not contribute to the systematic uncertainty of the measured angular distributions, which is very important for polarization measurements.

2.2.2.2 The Straw Tube Tracker

The Straw Tube Tracker (STT) [58], [26] consists of 2704 straw tubes. Each tube has a diameter of 10 mm and a length of 1050 mm. The tubes are made of aluminized mylar film of 31 μm thickness serving as cathode, and are filled with $ArCO_2$ gas at 1.25 bar pressure. The anode is a 20 μm thick gold plated tungsten wire which is stretched along the straw axis and is fixed by two crimp pins in light-weight end caps closing the tube at both ends. A potential difference of 1820 V is applied between cathode and

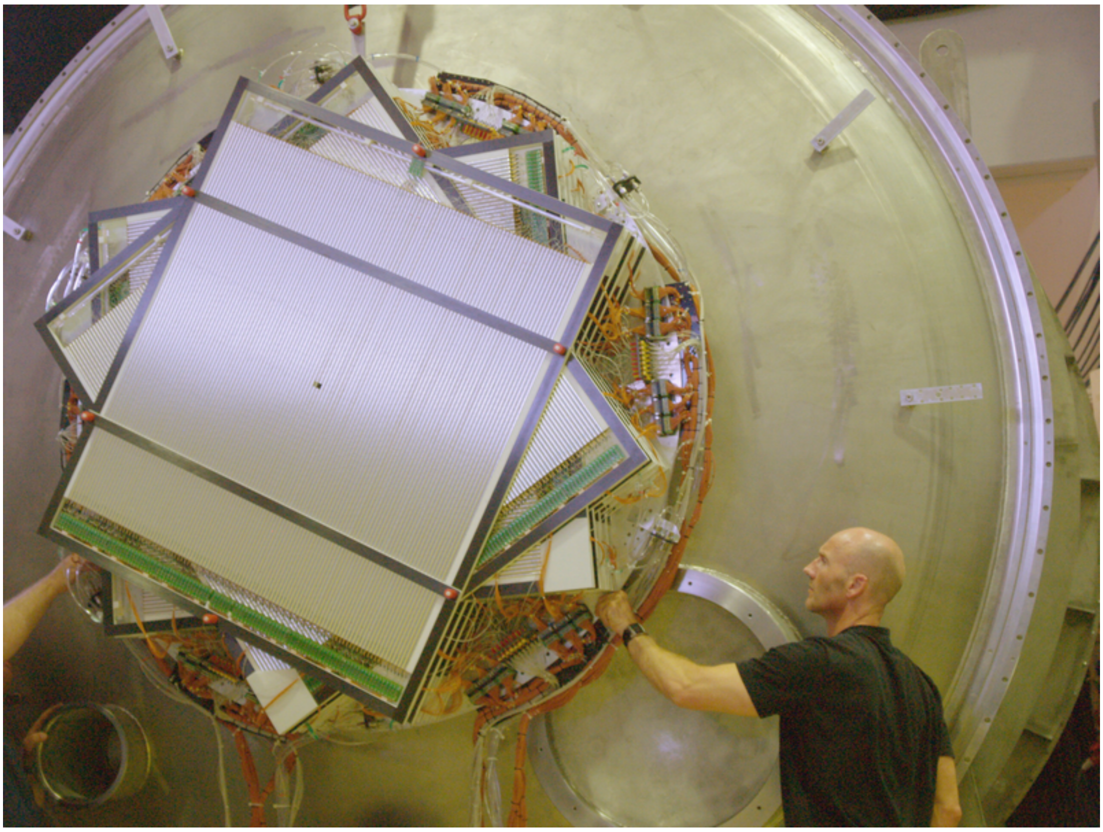

Figure 2.7 – Photo of the Straw Tube Tracker during the mounting it to the front cap of the barrel.

anode.

All tubes are organized in 13 double-layers and are fixed in three orientations with a relative angle of 60° as shown in Fig. 2.7. The rotation is needed for 3-dimensional track reconstruction. A central beam hole of 15×15 mm^2 dimension was realized by replacing the 4 central straws of each double-layer by 8 shorter (half-length) straws. The STT with a total active volume of 2230 liters is self supporting and contributes only about $X/X_0 \simeq 1\%$ to the total radiation length of the material which is on the path of the registered particles.

2.3 Trigger System

The trigger system is based on programmable electronics. Up to five different trigger conditions with different reduction factors can be applied simultaneously. A trigger condition is composed of a logical combination of charged particle multiplicities in the start counter and in the different stop counters. For hyperon detection as a trigger condition the increase of the number of charged particle tracks from the start to the stop counters was used. In particular, for the selection of the reactions $pp \to pK^+\Lambda$ and $pp \to pK^0\Sigma$ the $2 \to 4$ jump in multiplicity should be used. According to this only events with multiplicity more than 2 in the start counter and more than 4 in stop counter were recorded.

For calibration purpose and for the determination of the beam parameters elastic scattering events were also recoded. To select those the requirement of 2 hits each in start and stop counters was used. Since the rate of elastic events is too high to record all of them, it was reduced by a factor of 10.

Chapter 3

Monte Carlo Simulations

Monte Carlo simulations provide data based on our best knowledge of physical processes, detector configuration and detector performance. The simulated data are used to determine detection and reconstruction efficiencies, to estimate background, and to optimize the selection criteria of reconstruction algorithms in order to obtain an optimal signal to background ratio. For the COSY-TOF experiment a Monte Carlo simulation program called TOFMC was developed. It is written in Fortran. In this work it was extended by adding an alternative event generator and by implementing a new subdetector as well as by adding detector inefficiencies for a more realistic detector response.

3.1 General Scheme

The general scheme of the COSY-TOF Monte Carlo simulation program (TOFMC) is shown in Fig. 3.1. The initial parameters of the particles like momenta, decay vertices and angular distributions are generated by the event generator. Then these generated particles are transported through the experimental setup and the signal of the hit subdetectors is digitized for the simulation of the detector response.

The transport is done using GEANT 3.21 [59]. It allows to transport particles through the various regions of the detector setup, taking into account geometrical volume boundaries and physical effects according to the nature of the particles themselves and their interactions with the matter. During the transport multiple scattering according to Moliere theory is taken into account and hadronic interactions are generated.

As output of the TOFMC simulation program we obtain data equivalent to data from the COSY-TOF experiment. Thus, both type of data can be further analyzed in the same manner.

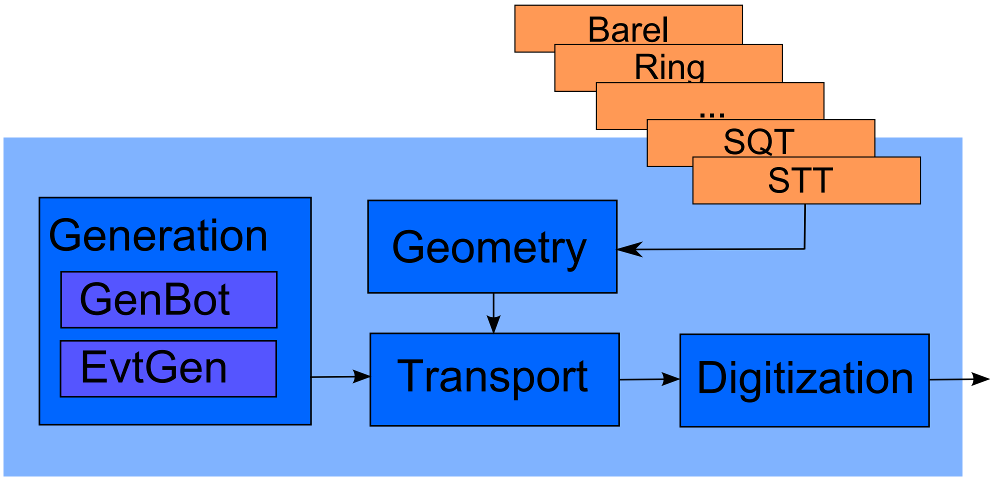

Figure 3.1 – The COSY-TOF Monte Carlo simulation framework.

3.2 Event Generator

GEANT 3.21 has a built-in phase space event generator called GENBOD. In the previous versions of TOFMC only this generator was used. To extend the simulation capabilities and meet further requirements to the particle generation an interface to the EvtGen [60] event generator was implemented as part of the TOFMC program.

EvtGen is an event generator primarily designed for the BaBar experiment, but is presently used in many modern experiments. EvtGen includes a spinor algebra to account for particle spins and to allow the accurate simulation of angular distributions, which is important for the simulation of polarization effects in the COSY-TOF experiment.

The EvtGen package provides a framework in which new decays can be added as modules. These modules, which perform the simulation of decays, are called models in EvtGen. One of the novel ideas in the design of EvtGen is that decay amplitudes, instead of probabilities, are used for the simulation of decays. The framework uses an amplitude for each node in the decay tree to simulate the entire decay chain, including all angular correlations. A user input mechanism allows using complex amplitudes to encapsulate the decay physics.

3.3 Detector Volume

The detector setup is described based on a structure of GEANT volumes. As an example, the STT is created using the GEANT TUBE volume. Each tube is rotated and placed appropriately to build the subdetector design as shown in Fig. 3.2.

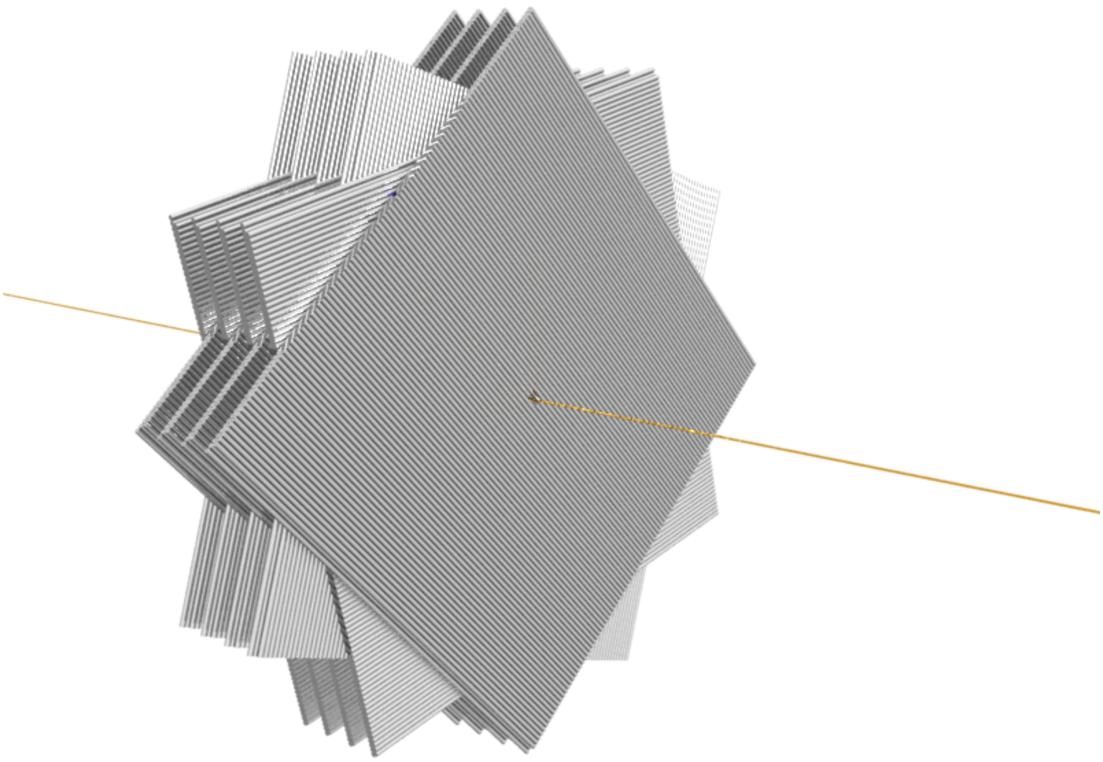

Figure 3.2 – Straw Tube Tracker as a structure based on GEANT TUBE volumes.

Another example is the SQT [61]. Its active volume is created as a cylinder, without separation into Archimedian spirals. During the particle transport through the detector volume GEANT returns spatial coordinates of the interaction points of the particle with the detector medium. Based on these coordinates, the spirals to which these points belong are calculated.

3.3.1 Simulation of Straw inefficiencies

It may happen that during the experiment some subdetector elements have low detection efficiency or do not provide a response at all. This may originate from problems with the mechanical setup or from problems with the electronics. To take this effects into account in the simulations the option of inefficiencies in particle detection is added. The base subdetector for track reconstruction is the STT. Therefore, inefficiencies of the straws are implemented in the simulation program TOFMC.

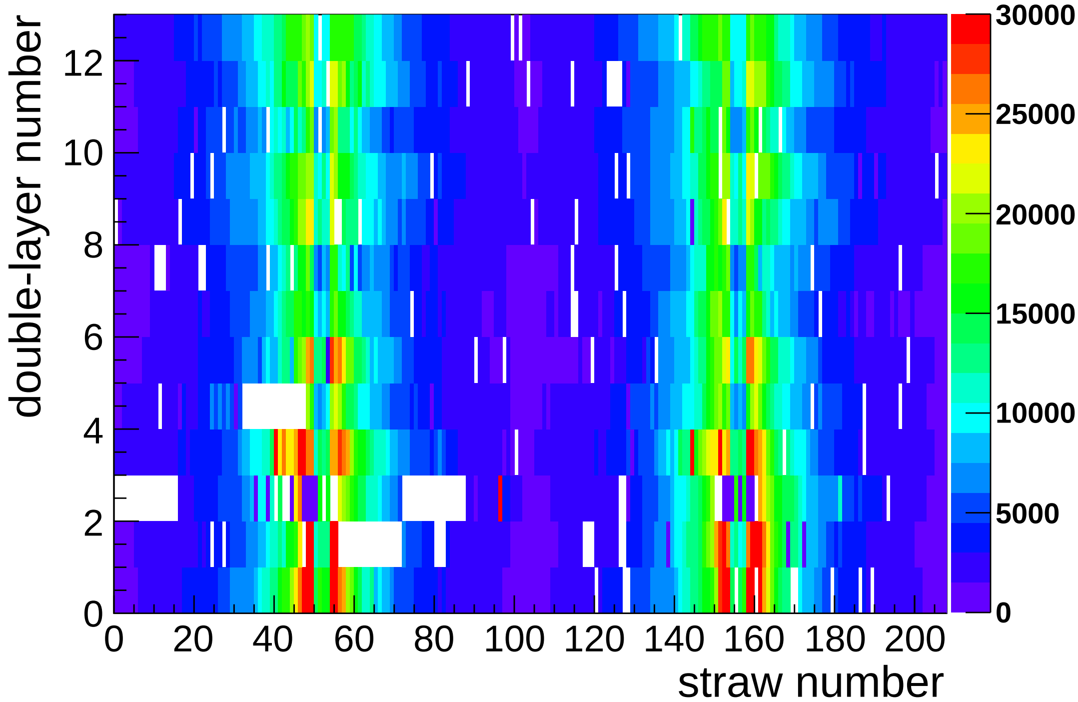

Figure 3.3 – Hit map of the STT plotted for 7×10^6 events obtained with the hyperon trigger.

About 7×10^6 events obtained with the hyperon trigger were used to plot the STT efficiency map which is shown in Fig. 3.3. The vertical axis shows the number of the double-layer plane while the horizontal axis shows the element number in the respective plane. The color code indicates the number of hits registered by the individual straw. Elements with straw number 50-53 and 154-157 are central elements of the front and backward layer of the double-layer plane, respectively.

There are four large inefficient regions created by a group of 16 straws each. These inefficiencies are explained by problems in the signal processing electronics since the straws signal are processed by 16-channel units. Other inefficiencies can be caused by mechanical damage of the straw wire as well as by other problems in the signal processing.

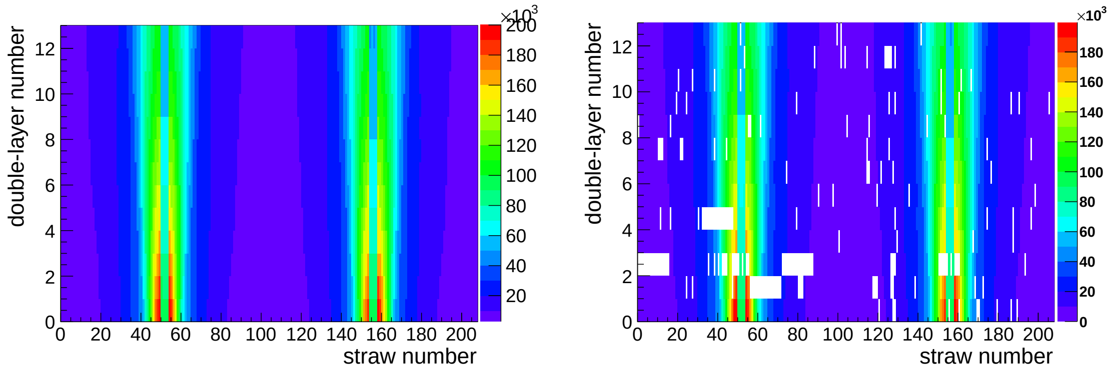

Figure 3.4 – Hit map of the STT for MC simulations without (left) and with (right) straw inefficiency.

Based on this map, elements with less than 1000 hits were marked as unresponsive. If a particle interacts with one of the marked straws then the signal from that straw is not recorded in the simulation.

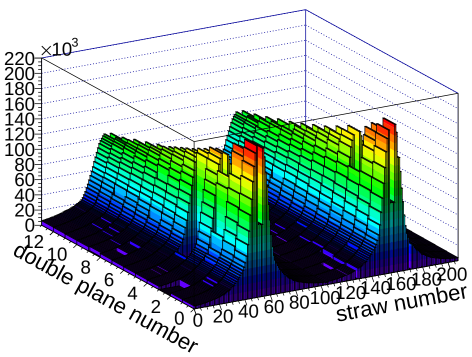

Figure 3.5 – 3D hit map of the STT for MC simulations including straw inefficiency.

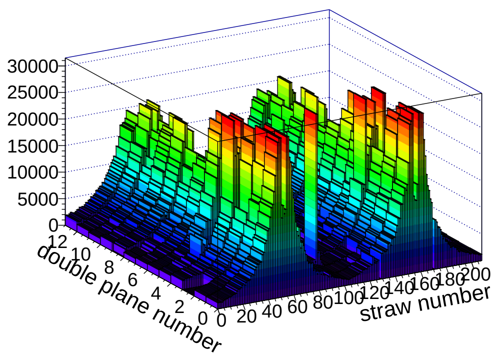

Figure 3.6 – 3D hit map of the STT for experimental data.

Figs. 3.4 show the simulated distribution of hits without (left) and with (right) straw inefficiency.

Fig. 3.5 and Fig. 3.6 show a 3D hits map for Monte Carlo events with implemented straw inefficiencies and for experimental data, respectively. In addition to unresponsive elements the experimental data also show noisy elements. Signals from those elements are ignored in track reconstruction.

3.3.2 Simulation of Σ^+ hyperon polarization

In the current analysis the polarization of the Σ^+ hyperon is determined. The polarization of the Σ^+ is generated in order to investigate the influence of the detector acceptance on the polarization observables and to control the algorithms of polarization determination. It is done in the EvtGen event generator framework by introducing a new model which includes the following steps:

- calculation of the polarization vector perpendicular to the production plane for each event;
- calculation of the Spin Density Matrix (SDM) r as follow:

$$r = 0.5(1 + s\vec{P}_N)$$

  where s is the Pauli matrix and $\vec{P}_N$ is the polarization vector;
- assigning the SDM to each event and performing the decay of the pp initial state to $pK_s\Sigma^+$ based on a phase-space distribution;
- performing the $\Sigma^+ \to p\pi^0$ and $\Sigma^+ \to n\pi^+$ decays with the HELAMP model [60], which allows the simulation of any two body decay by specifying the helicity amplitudes of the final state particles.

The helicity amplitudes of Σ^+ can be easily obtained knowing the asymmetry parameter α:

$$|H_{(1/2,0)}|^2 = \frac{1+\alpha}{2}\ , \quad |H_{(-1/2,0)}|^2 = \frac{1-\alpha}{2}$$

The absolute value of the polarization P_N can be set to any value within the range [-1,1].

3.4 Event Display

The event display is an important tool both for the online monitoring during the experiment and for the offline data evaluation and developing process. The online event display and data monitoring system developed for the COSY-TOF experiment is presented in Refs. [62], [63].

The offline event display can be used to control the detector geometry as well as the hit positions of simulated and experimental data. It also allows to visually control different stages of the reconstruction and fitting algorithms. Numerous physical tasks can be addressed to the event display (e.g. visual control of acceptance for different events types; control of secondary interactions). To achieve this performance the offline event display TofEve is developed on the base of the ALICE ESD track visualization software [64] as a part of current work. It is written in C++ with extensive use of the ROOT [65] classes.

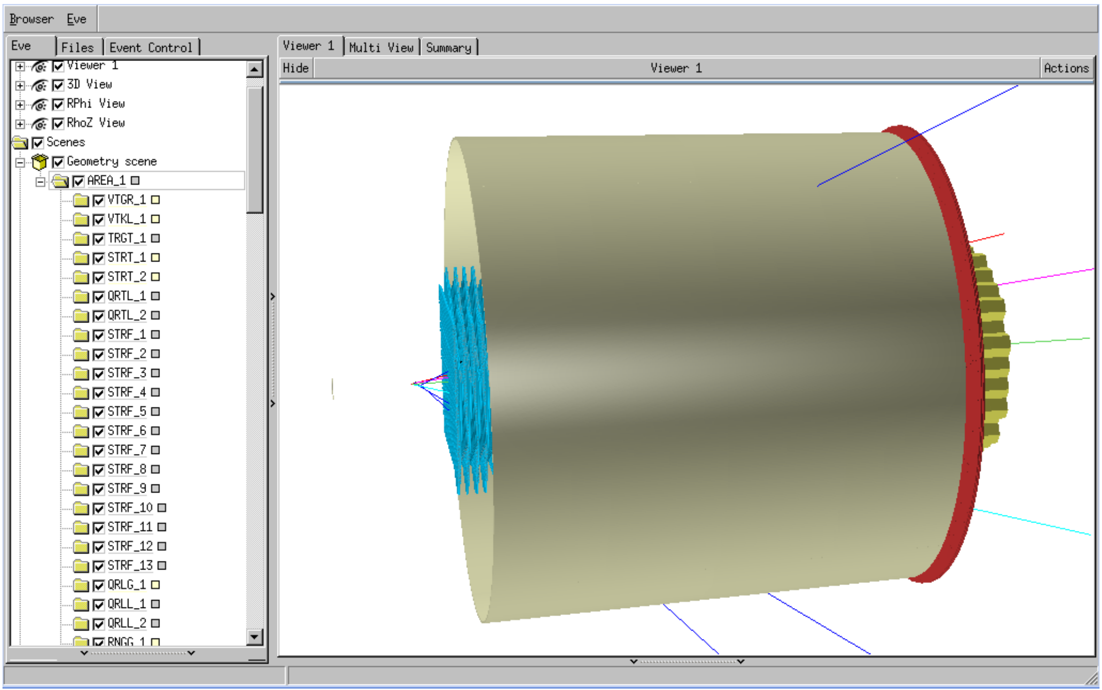

Figure 3.7 – Graphical user interface of TofEve. On the left side one can select subdetectors to be shown. On the right side the used GEANT volume of the COSY-TOF detector together with a $pK\Sigma^+$ final state is shown.

The geometry volume of the COSY-TOF detector is exported from the GEANT/ZEBRA RZ data format to ROOT by the *g2root* routine [66]. The obtained file can be loaded and displayed by TofEve with different options. Fig. 3.7 shows the user interface of the TofEve event display. On the left side the so-called detector geometry tree with checkable boxes is seen. Each element of this tree is a part of the detector, by checking or unchecking it the specified element can be shown or hidden in the display on the right side. As an example, the complete COSY-TOF detector setup, as it is used in simulations, is shown on the right side of Fig. 3.7. Here the beam is pointing

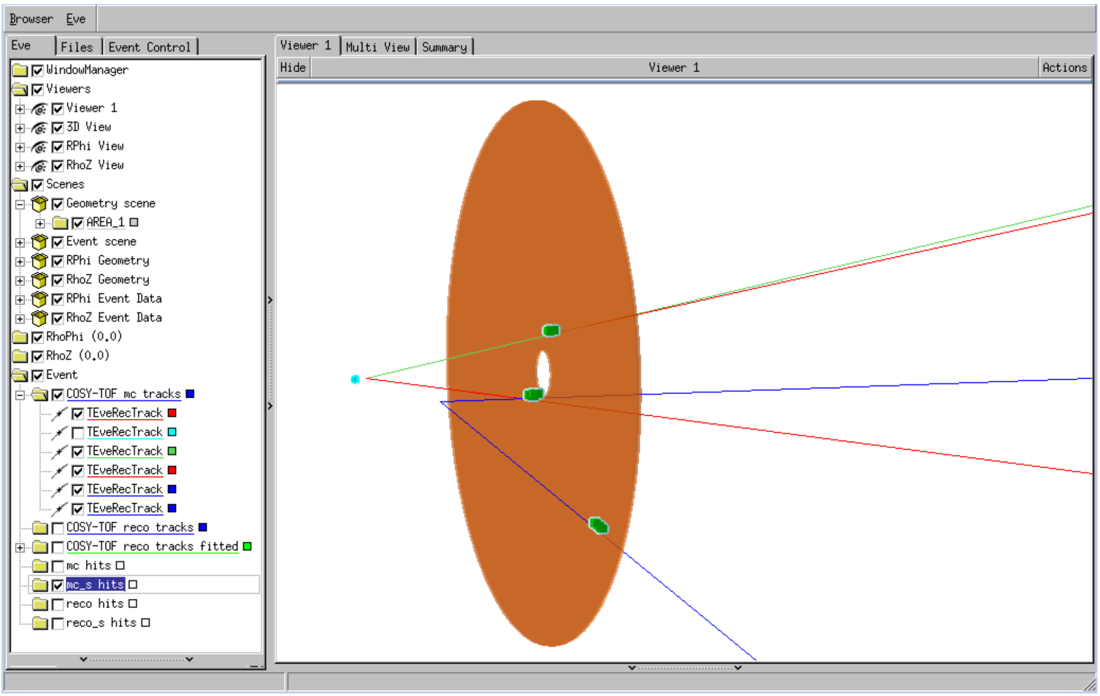

Figure 3.8 – TofEve - track and hit viewer. On the left side one can select tracks and hits to be shown. On the right side SQT subdetector together with the simulated $pK\Sigma^+$ event and with the corresponding hits is shown.

from left to right and lines of different color indicate the different final state particles of the simulated reaction $pp \to pK_s\Sigma^+$. TofEve allows to plot the event tracks from different stages of the reconstruction. For example, the MC reconstructed tracks before and after the kinematical fitter can be plotted together with the true MC events. This gives the possibility for visual tests of the reconstruction and fit algorithms.

In addition, hit information of the simulated or reconstructed events can be plotted.

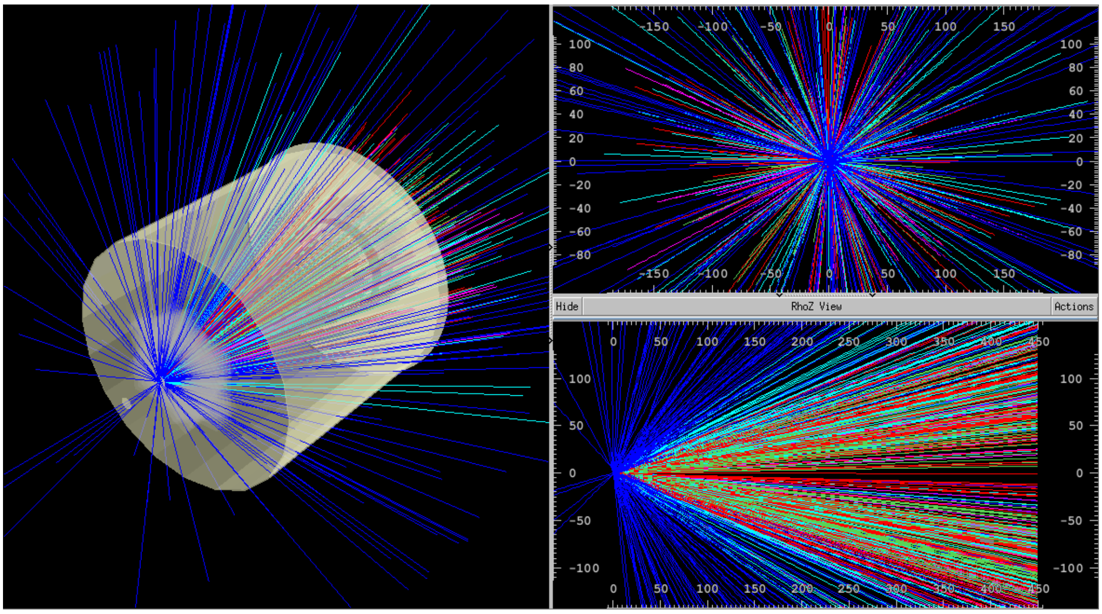

Figure 3.9 – 100 simulated $pK\Sigma^+$ events plotted together. The blue color stands for pions, the red for protons and the green tracks show the direction of Σ^+ hyperons.

On the right side of Fig. 3.8 the SQT is shown together with hits from the $pK_s\Sigma^+$ final state.

The events can be shown one by one or in accumulative mode where many events are superimposed. The accumulative mode gives the possibility to study the acceptance for different particles. For example, Fig. 3.9 shows 100 simulated $pp \rightarrow pK_s\Sigma^+$ events. In the figure, pions are shown in blue, protons in red and the green lines show the track directions of the Σ^+. Pions are emitted at large polar angles, sometimes in backward angles, while the protons and Σ^+ have small polar angle and fly preferable in the beam direction.

Chapter 4

Calibration

4.1 Straw Calibration

The Straw Tube Tracker (STT) is the most relevant subdetector for geometrical track reconstruction. This means that the errors (statistical or systematic) of measurements provided by this subdetector will directly induce errors to the determined track parameters. Therefore, the calibration of the STT is particulary important for the further analysis. Two items need to be calibrated:

- the relation of the TDC value and the isochrone radius;
- the position of the straw tubes.

4.1.1 Calibration of TDC to radius relation

A charged particle passing through a straw ionizes the gas inside the straw. The drift time needed to collect this ionization is digitized and stored in a time to digit (TDC) format. The start of this time measurement is triggered by the start counter (Sec. 2.2.1) which is located about 26 cm before the first double-layer of the STT. The time of flight for this distance induces a positive offset of the drift time measurement which can not easily be eliminated since its value depends on the speed of the detected particle which ranges from 25% to 99% of the speed of light, corresponding to about one to four ns. However, the drift time is much longer than the time needed for the particle to reach the STT, hence this offset can be neglected. The relation between the TDC value and the true time is defined by $t = 0.09259ns{\cdot}\mathrm{TDC}$, where the TDC is the channel number and the conversation factor is a property of the electronic hardware.

Fig. 4.1 shows the converted TDC time spectrum for 10^6 hits on a single straw. The drift time is directly correlated with the distance of closest approach of the particle trajectory to the anode wire of the straw. The value of this distance, called isochrone radius (Fig. 4.2), is needed to reconstruct the track parameters.

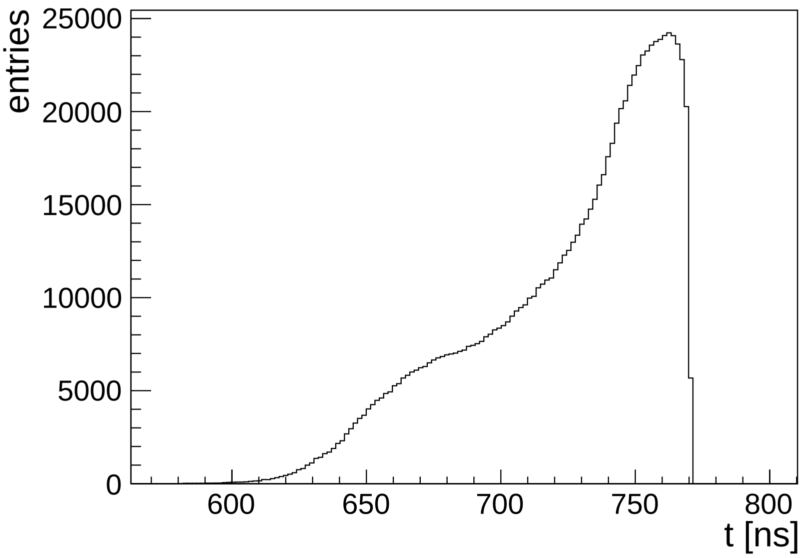

Figure 4.1 – TDC spectrum for 10^6 hits on single straw. Large times correspond to smaller distances between track and the anode wire.

The relation between the TDC time and the isochrone radius called "TDC-to-radius curve" from now on, is determined in two steps. In the first step the shape of this curve

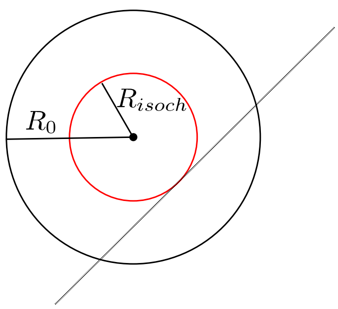

Figure 4.2 – Cross section of a straw tube perpendicular to the straw axis. $R_0 = 0.5$ cm is the radius of a straw. R_{isoch} - isochrone radius for displayed track.

is determined by a "self calibrating" method and then it is improved by the "distance to track" method, as described in the following sections.

4.1.1.1 "Self calibrating" method

With the assumption that the tracks hit the straws homogenously across the straw radius and that the detection efficiency is constant in that range we can write:

$$\frac{dN}{dr} = \frac{N_{tot}}{R_0} \tag{4.1}$$

where N_{tot} is the total number of tracks passing the straw and R_0 is the straw tube radius. We can write:

$$\frac{dN}{dt} = \frac{dN}{dr}\frac{dr}{dt} = \frac{N_{tot}}{R_0} v_{drift}(t) \tag{4.2}$$

Integration over the drift velocity results in the isochrone radius:

$$r(t_1) = \int_{t_0}^{t_1} v_{drift}(t)dt = R_0 \frac{N_{01}}{N_{tot}} \tag{4.3}$$

where N_{01} is the number of tracks with TDC time between t_0 and t_1. The value of t_0 is defined by largest drift time.

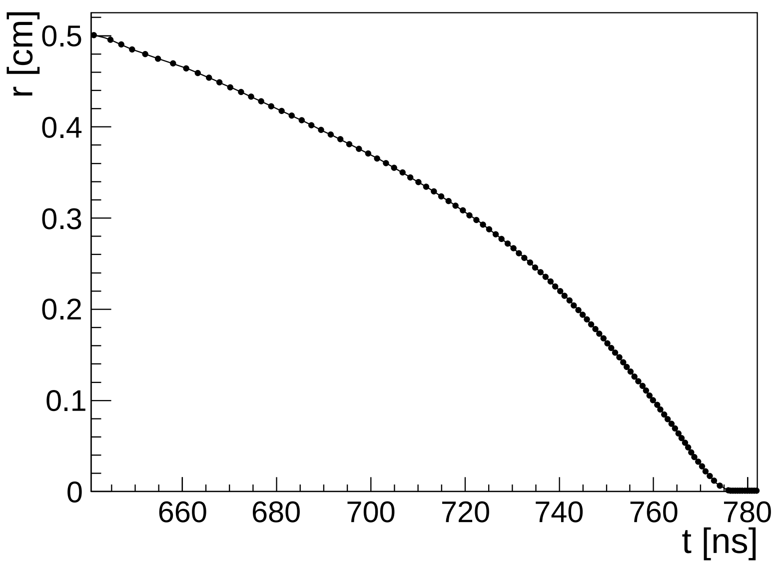

Figure 4.3 – Time to isochrone radius curve from the "self calibrating" method.

The drift time distribution (Fig. 4.1) is divided into 100 bins. For each bin Eq. (4.3) is evaluated (with t_1 equal to the central value of the bin). As result the relation between time and isochrone radius is obtained as shown in Fig. 4.3. The lower time on the plot is limited to 650 ns which corresponds to the outer diameter of the straw

$r = 0.5$ cm, although part of the hits, having the time value lower than 650 ns (see Fig. 4.1), give the isochrone radii larger than 0.5 cm. To account for this effect the radius of the straw used in the calibration is extended to 0.51 cm.

In Fig. 4.3 a first approximation is shown. We know that the detection efficiency is not constant over the full straw radius. If a track passes through the straw close to the tube wall, then it has a short path length in the active volume and as a result it cannot ionize enough atoms to create a signal. Another critical case occurs if a track passes through the straw close to the anode. Then the part of electrons which are created close to the anode do not have sufficient path length to trigger secondary ionizations and thus they introduce the systematical shift in TDC spectrum.

4.1.1.2 "Distance to track" method

Using the TDC to radius relation obtained by the "self calibrating" method the isochrone radii for all charged particles passing a straw tube are obtained and track reconstruction and fitting with the methods described in Ch. 5 is done. After obtaining the track parameters the correlation between the distance from the track to the anode of the straw and the TDC time is obtained as shown in Fig. 4.4 (left).

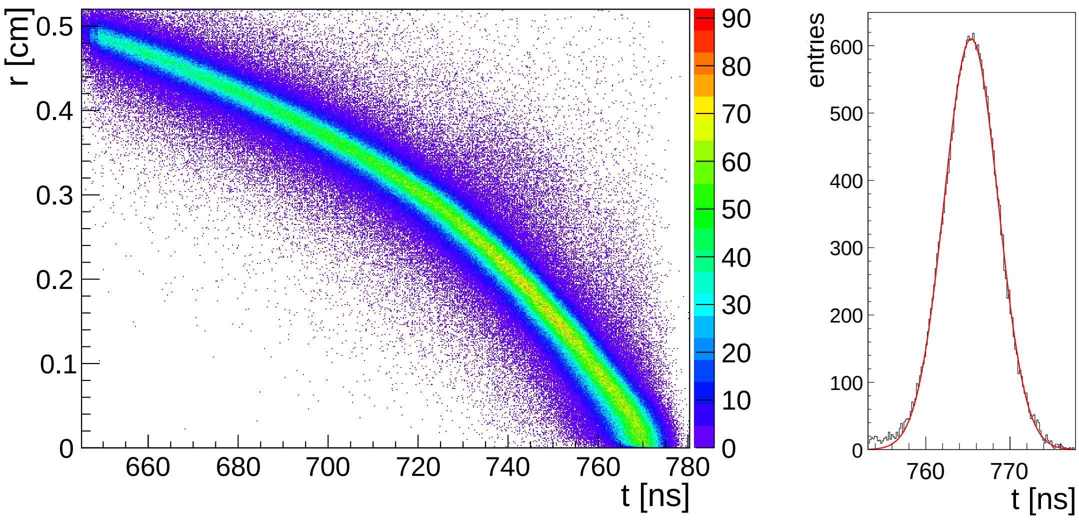

Figure 4.4 – Left: TDC time versus isochrone radius plotted for 1.5×10^6 hits on a single straw. Right: projection of one bin (out of 100) of r onto the t axis. The red line is a gaussian fit to the data.

The width of the radius distribution for a fixed TDC time is defined by the resolution of the drift distance determination and by imperfect TDC-to-radius curve from the "self calibration" method (Fig. 4.3). To find the most probable relation between the TDC time and the isochrone radius the spectrum shown in Fig. 4.4 (left) is divided into 100 bins in the r axis, and the content of each bin is projected on the t axis. Fig. 4.4 (right) shows such a projection for a single bin in the isochrone radius. The peak value of the gaussian fit is the most probable TDC time of the corresponding bin in r.

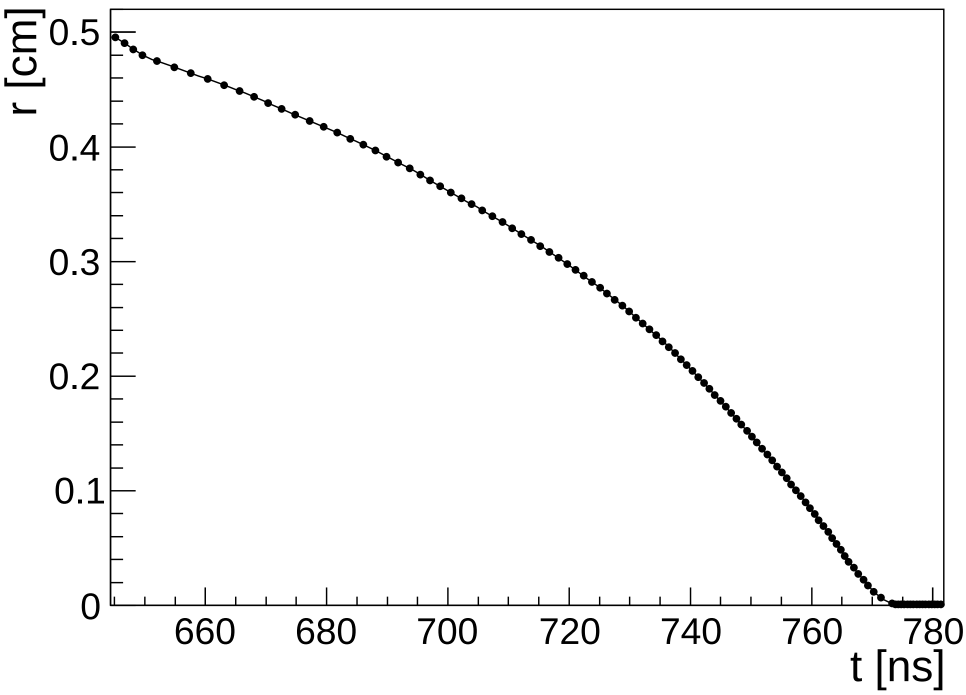

Figure 4.5 – TDC time to isochrone radius curve as a result of the "distance to track" method.

Repeating this procedure for all r bins generate a relation between the TDC time and the most probable isochrone radius, as illustrated in Fig. 4.5. The shape of this curve is similar to the one that was obtained by the "self calibrating" method. This means that the assumption of a homogenous detection efficiency across the full straw radius is close to reality.

In the ideal case the curve in Fig. 4.5 should be deduced for all straws. However obtaining a smooth distribution of the fit points as in Fig. 4.5 requires at least 10^6

hits per straw tube. In order to achieve this, the complete data set needs to be used. Even then, about 10% of all straws have less then 10^6 hits. Therefore, the evaluation is done in the following way: in the first step the curve is deduced according to Fig. 4.4 (left) for a complete double-layer. Afterwards for each individual straw it is determined whether the number of hits in this straw exceeds 10^6. If the number of hits is smaller than 10^6, the respective straw inherits the curve from the double-layer it is part of.

4.1.1.3 Correction for propagation time

Recorded TDC values do not only represent the drift time of ionization charge in a straw tube but also include the signal propagation time from the hit location to the readout electronics. The straw electronics of each double-layer is located at one side (green band in Fig. 2.6). For the next double-layer the configuration is rotated by 60° corresponding to the previous one. Let us consider the most critical case, namely two double-layers with opposite locations of their electronics (e.g the first and the forth double-layer) as shown in Fig. 4.6. In such a case to the true drift time of the hits H_1 and H_2 the additional time needed for the signal to propagate from H_1 to E_1 and from H_2 to E_2 is included in the measured TDC time.

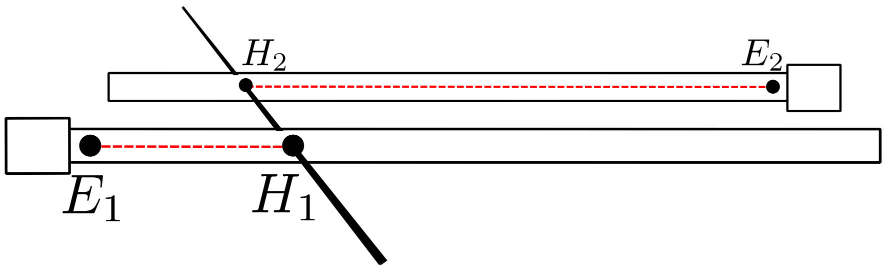

Figure 4.6 – Straws from two double-layers with opposite locations of the electronics hit by the same particle. Hits H_1 and H_2 have different signal propagation time to the read-out electronics E_1 and E_2, respectively.

The maximum possible difference in the TDC time introduced by this effect is given by the length of the straw tubes. For a 1.05 m long straw tube the signal propagation time is about 5 ns. Based on Fig. 4.5 this can contribute up to a 50 μm error to the determination of the isochrone radius. The effect cancels if the track passes through the straws at half of their length. Otherwise, in a situation as shown in Fig. 4.6, the drift time of the hit H_1 is underestimated and that of hit H_2 is overestimated.

To correct this effect, tracks are reconstructed as described in Ch. 5. Knowing the track direction, the hit positions in all hit straws are calculated and thus the distances from the hits to the electronics are determined. Then from each TDC time the signal propagation time for the determined distance is subtracted.

4.1.2 Calibration of straw positioning

Significant errors to the determination of the isochrone radius are introduced by insufficient knowledge of the exact geometrical location of the straws. The positioning of the straws within a double-layer due to its compact structure is known very exactly. The largest uncertainty in the position of individual straws originates from the uncertainty in the position of a whole double-layer. For further evaluations the position of a double-layer is defined by the x,y,z coordinates of its geometrical center and by its rotation around the x,y,z axes by the angles φ_x,φ_y,φ_z.

To find the most probable position and rotation of each double-layer, tracks need to be reconstructed and fitted. After the track directions and positions are found, the distances of closest approach between the tracks and the anode wires of the straws are calculated. The wire positions and rotations are parameterized as a function of double-layer shifts and rotations. The resulting distances are compared with the corresponding isochrone radii, and the differences are minimized as follows:

$$\chi^2 = \sum_{t=1}^{N_{trk}} \sum_{i=1}^{13} \sum_{j=1}^{N_{ti}} \frac{(r_{tij} - d_{tij})^2}{\sigma_{tij}^2} \tag{4.4}$$

where: N_{trk} - total number of tracks.

N_{ti} - number of hits created by tth track in ith double-layer.

σ_{tij} - resolution of isochrone radius measurement.

r_{tij} - determined isochrone radius.

d_{tij} - distance of closest approach between track and straw anode wire. It is calculated after track reconstruction (Ch. 5) as follows:

$$d_{tij} = \frac{[\vec{v}_{tij} - (\vec{w}_{ij} + \vec{c}_i)]\vec{t}_{ij} \times (\vec{s}_{ij} r_i)}{|\vec{t}_{tij} \times (\vec{s}_{ij} r_i)|} \tag{4.5}$$

where : $\vec{v}_{tij}$ is any space point lying on the track

$\vec{w}_{ij}$ - any space point lying on straw wire.

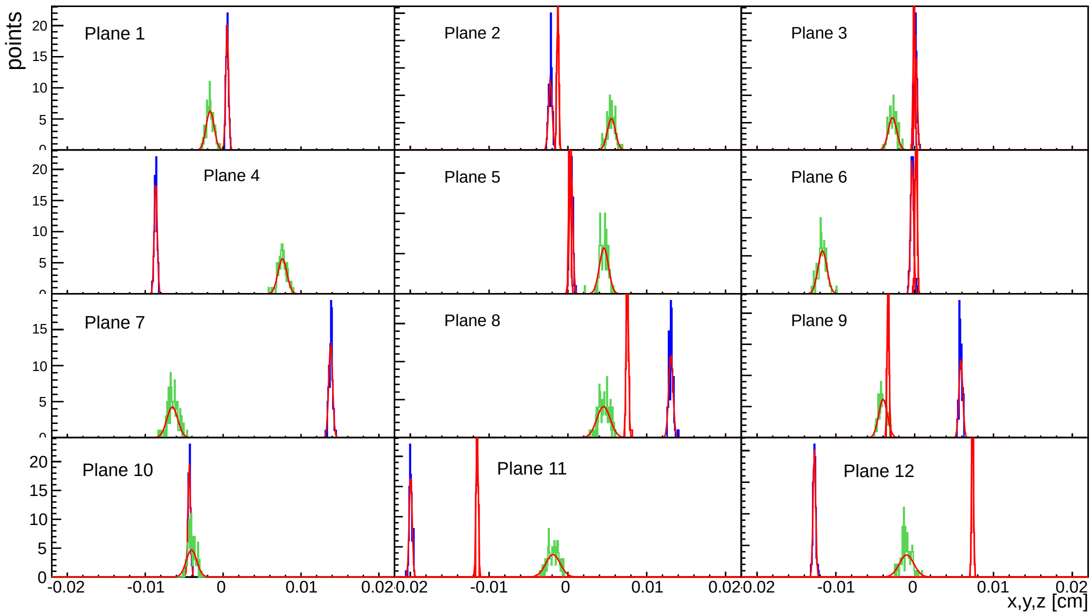

Figure 4.7 – Position shift of double-layer planes before correction. The color defines the coordinate axis: x - red, y - blue, z - green.

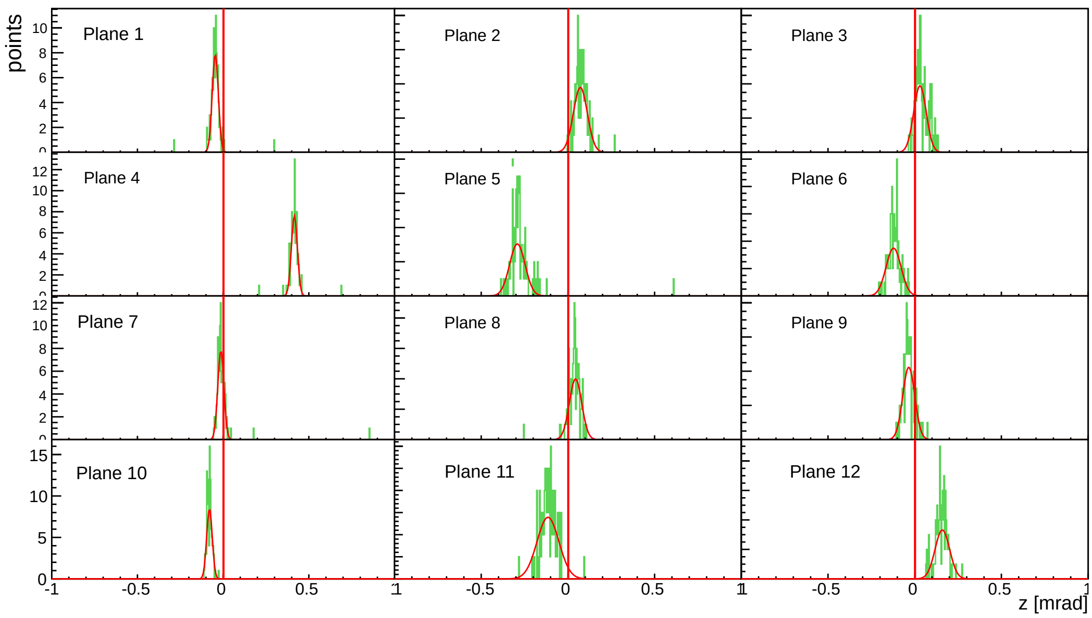

Figure 4.8 – Rotation shift of double-layer planes before correction. The color defines the coordinate axis: x - red, y - blue, z - green. The rotation around the x and y axes are negligibly small.

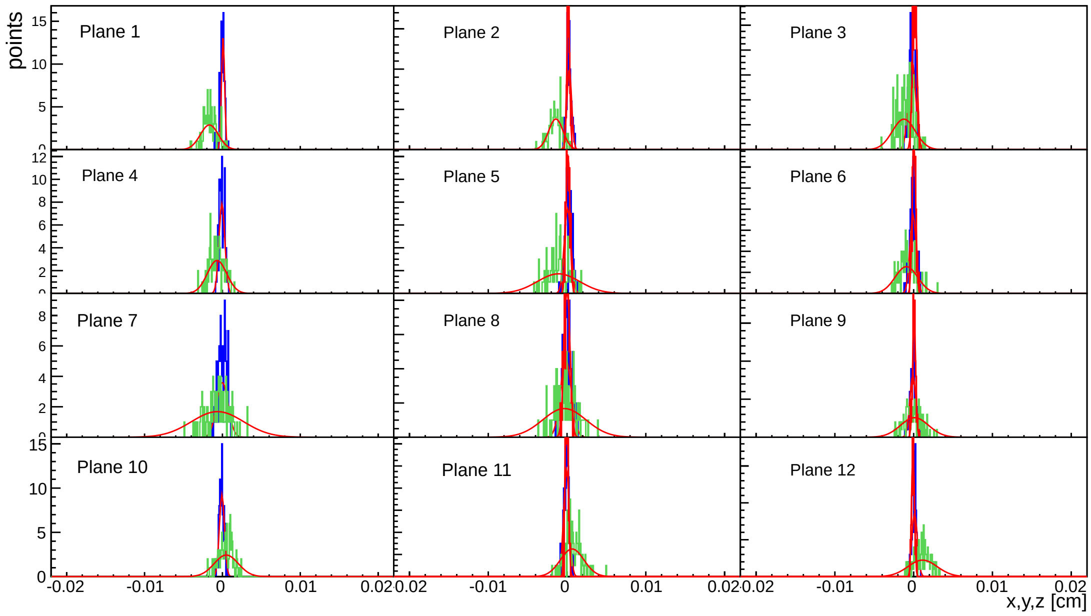

Figure 4.9 – Position shift of double-layer planes after correction. The color defines the coordinate axis: x - red, y - blue, z - green.

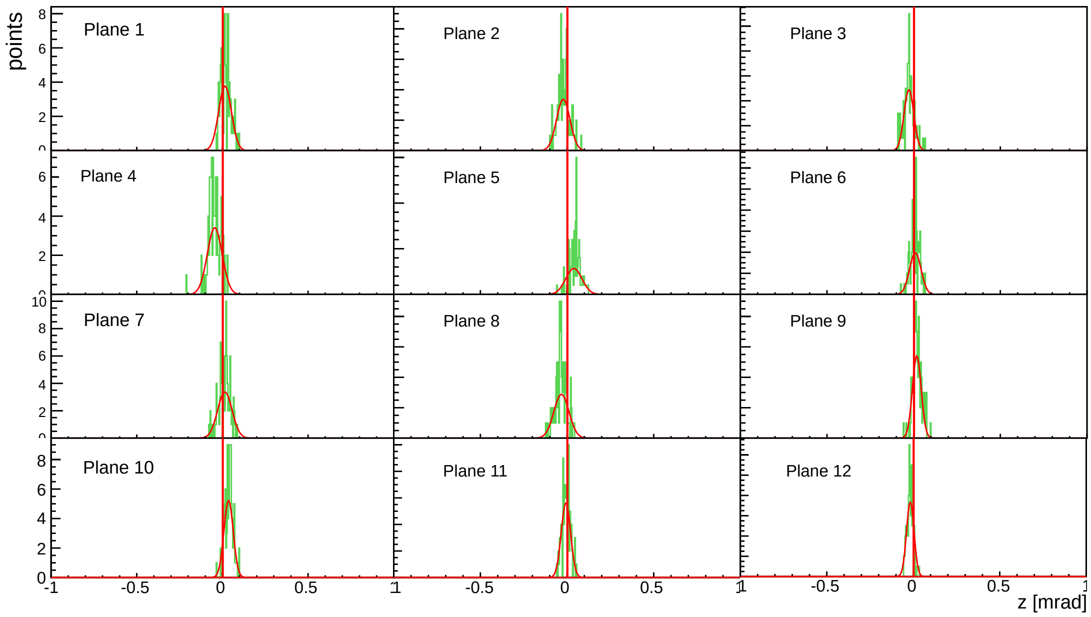

Figure 4.10 – Rotation shift of double-layer planes after correction. The color defines the coordinate axis: x - red, y - blue, z - green.

$\vec{c}_i$ - shift of double-layer corresponding to its nominal position (Δx_i,Δy_i,Δz_i).

$\vec{t}_{tij}$ - direction of the track.

$\vec{s}_{ij}$ - direction of the straw anode wire.

r_i - rotation matrix created by $\Delta\varphi_{x_i}$,$\Delta\varphi_{y_i}$,$\Delta\varphi_{z_i}$ which define the rotation of the double-layer corresponding to its nominal orientation.

Free parameters of the minimization are the shift of each double-layer Δx_i, Δy_i, Δz_i and the rotation of each double-layer $\Delta\varphi_{x_i}$, $\Delta\varphi_{y_i}$, $\Delta\varphi_{z_i}$ with respect to its nominal orientation. All together it results in $6 \times 13 = 72$ fit parameters. The wire direction of four double-layers is parallel to the x axis, thus the shift in the x direction will not influence the distance from the track to the wire.

To test the stability of the minimization procedure, 100 data samples with 100,000 events each were evaluated. As a result, the distribution of each minimized parameter is distributed like a gaussian the maximum of which represents the most probable value of the parameter (Figs. 4.7 and 4.8).

As one can see in Fig. 4.7 the mechanical installation of the STT is so precise that the measured position differs by no more than 200 μm from the nominal position. Rotation angles around the z axis are less than 0.5 mrad, around x and y axis are negligibly small. as seen in Fig. 4.8.

The shifts and rotation parameters for position and orientation of the straw double-layers are determined in an iterative procedure. Starting with the nominal position and orientation, the TDC to isochrone radius relation deduced with the "distance-to-track" method is used to obtain improved value for the position and orientation of the straw double-layers. After 8 iterations the recalibration procedure converged, and final values for the shift and rotation parameters are obtained. The distribution of the shifts and rotations angles after the correction are shown in Figs. 4.9 and 4.10.

The minimization of the χ^2 value according to Eq. (4.4) is not sensitive to a proportional change of the distance between the double-layers d_l. That is the extension of the STT in z direction can be proportionally squeezed or expanded as compared to the nominal extension. A possible deviation of this kind can be examined with pp elastic scattering events (Sec. 6.1). A proportional change of d_l cause a change of the apparent opening angle of two protons and thus affect the kinematic variables. Fig. 4.11 shows the systematic shift in the average missing energy of pp elastic scattering events caused by this effect. The same behavior is observed in the MC simulations by introducing a proportional change of d_l in reconstruction.

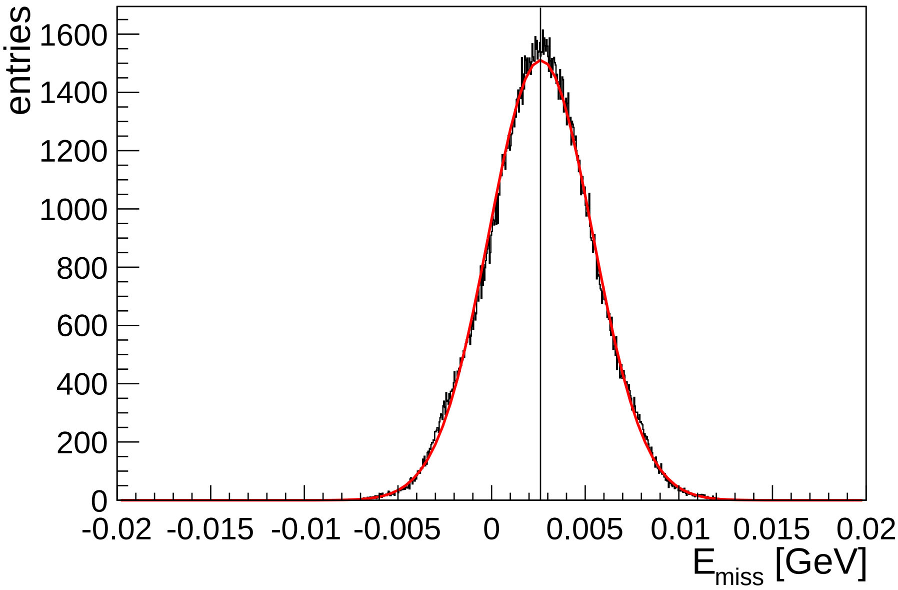

Figure 4.11 – Systematic shift in the missing energy of pp-elastic events caused by a proportional change of the distance between double-layers. The mean value of a gaussian fit is shifted from the expected value by 2.6 MeV.

Based on the found shift in the average missing energy of pp elastic scattering events of 2.6 MeV the scale factor for d_l is determined to be 0.97. A final test shows that this correction to the straw double-layer position induces no changes to Figs. 4.9 and 4.10.

4.1.3 Estimate of errors from different effects

To estimate errors which can be introduced by different effects the TDC to isochrone radius curve is plotted with and without taking into account these effects. Fig. 4.12 shows the TDC to isochrone radius curve obtained for the first double-layer which we will call the "central curve".

Fig. 4.13 shows the TDC to radius curves obtained for individual straws of the first double-layer. From the comparison of Fig. 4.13 with Fig. 4.12 the following conclusion can be drawn: about 95% of the curves have deviations in the range up to 70 μm and about 5% have deviations in the range between 70 μm and 200 μm. The deviations

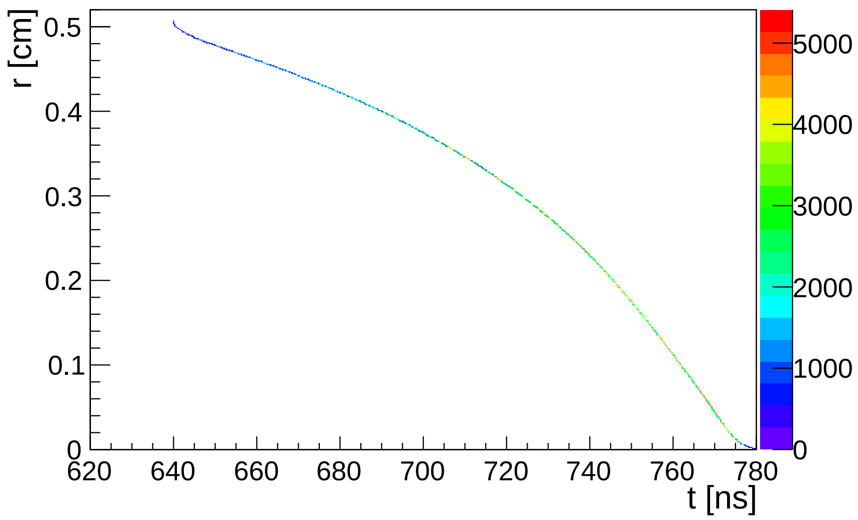

Figure 4.12 – TDC to isochrone radius curve obtained for the first double-layer referred to as the "central curve".

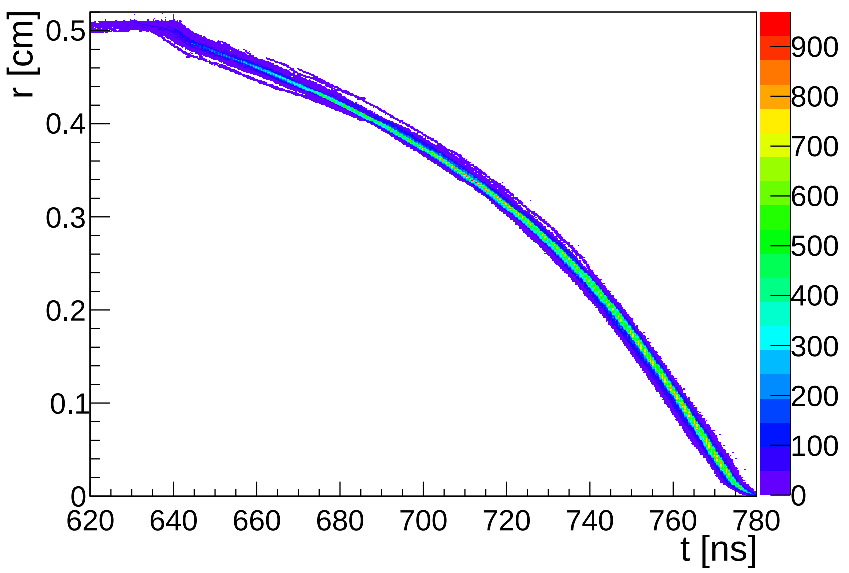

Figure 4.13 – TDC to radius curves obtained for each individual straw tube of the first double-layer. The color defines the density distribution of hits.

may be due to small shifts of the straw tube positions within a double-layer, as well as to differences in the electronic read-out.

Fig. 4.14 shows the TDC-to-radius curve obtained for the complete first double-layer, taking into account the signal propagation time in the straw tube. Applying this correction, about 95% of the hits deviate from the "central curve" in the range up to 30 μm and about 5% deviate in the range between 30 μm and 80 μm.

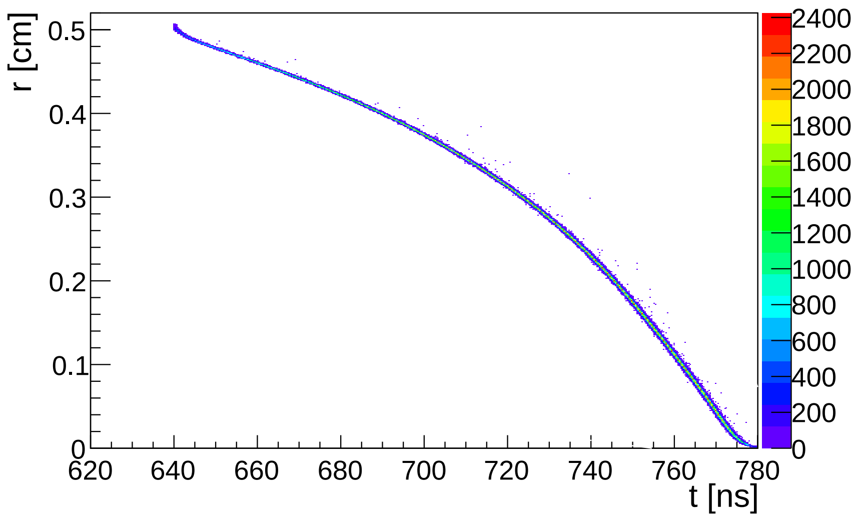

Figure 4.14 – TDC to radius curve obtained for the complete first double-layer, taking into account the signal propagation time in the straw tube.

These results show that the TDC-to-radius curve obtained for each individual straw can significantly improve the resolution of radius determination in comparison to the TDC-to-radius curve obtained for the whole double-layer. The larger deviation of hits in Fig. 4.13 from the "central curve" than that of hits from Fig. 4.14 indicates that using the signal propagation time in the straw tube is not so critical as using the TDC-to-radius curve obtained for each individual straw.

4.1.4 Results of the STT calibration

To determine the spatial resolution of a single straw tube the distance from a track to the isochrone radius versus the isochrone radius is plotted in Fig. 4.15.

The obtained distribution is divided into 100 bins in the r axis and the content of each bin is projected on the d axis as shown in Fig. 4.16. The resulting spectrum is fitted with a gaussian function which reproduces the distribution well except the tails. The deviation in the tails may originate from:

- insufficient hits for the calibration of straw tubes at the edges of the double-layers;
- wrong hit assignment to tracks in the track finding procedure;
- emission of δ-electrons which causes several straw tubes in one layer to fire.

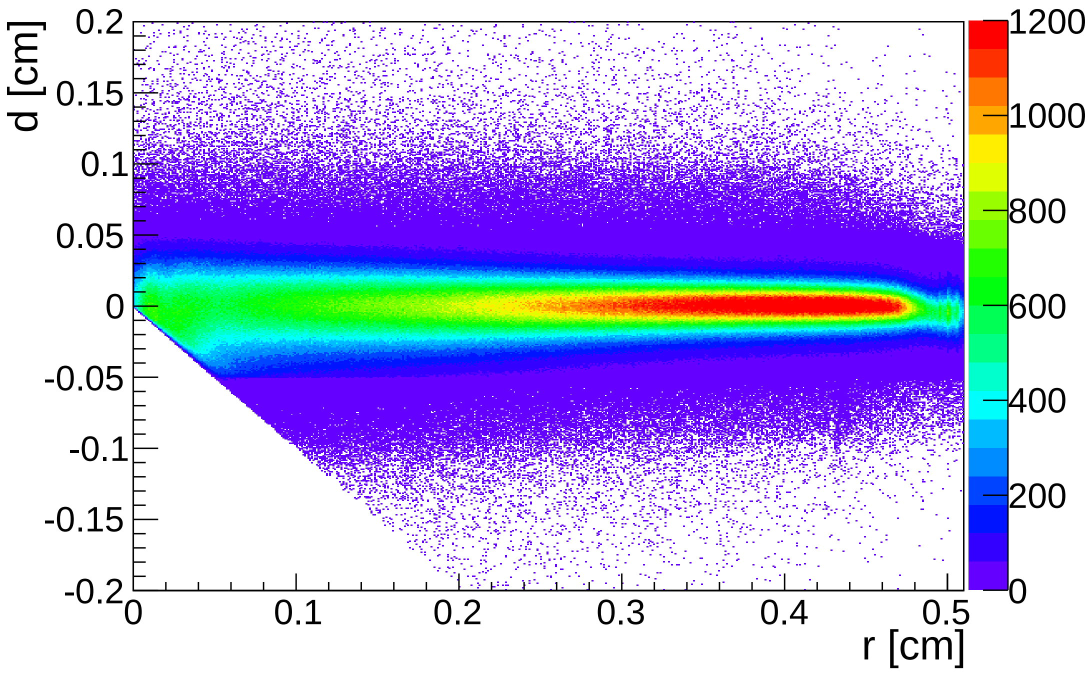

Figure 4.15 – The distance from track to isochrone radius versus isochrone radius, combined for all planes and for 21.5×10^6 hits.

A deviation from zero of the peak value of the gaussian fit would induce a systematic error in the determination of the isochrone radius. The amount of this deviation as a function of the drift radius is shown in Fig. 4.17. At distances from the wire between 0.05 cm and 0.48 cm, representing 95% of the full radius, the deviation is smaller than 5 μm.

The σ width of the gaussian fit functions to the distributions in d for the 100 projected bins as a function of the drift radius are shown in Fig. 4.18 for the first double-layer plane.

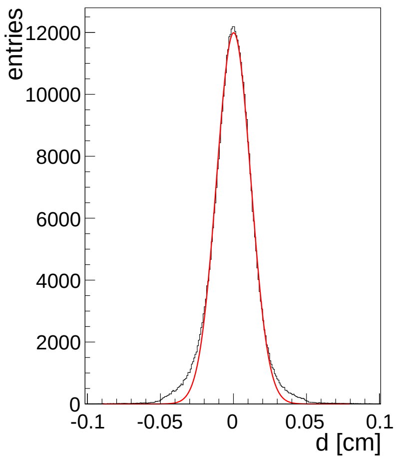

Figure 4.16 – One bin in r axis (out of 100) of Fig. 4.15 projected on the d axis and fitted with a gaussian function.

The distribution is fit with a polynomial function of second order. The result of the fit is given in Eq. (4.6).

$$\sigma(r) = 0.02709 - 0.06671r + 0.05747r^2 \tag{4.6}$$

This width determines the average position resolution of a single straw tube. The obtained fit result (Eq. (4.6)) was used in the Monte Carlo simulation of the drift time resolution as well as for further analysis of the experimental data.

Plane	1	2	3	4	5	6	7	8	9	10	11	12	13
$\sigma_{0.25}$, [μm]	140	142	136	146	160	146	164	161	146	141	144	135	139

Table 4.1 – Drift radius resolution at 0.25 cm radius for all 13 double-layer planes. The average value over all 13 planes is 146 μm.

To control the quality of the calibrated double-layer position and orientation, in the same way as described above and shown for the first double-layer in Fig. 4.18 the resolution is determined for all double-layers as shown in Fig. 4.19. There is no significant difference in the shapes of the curves as well as in absolute values of the spatial resolution. This means that the position and orientation correction are done equally well for all double-layers and all TDC-to-radius curves are determined with

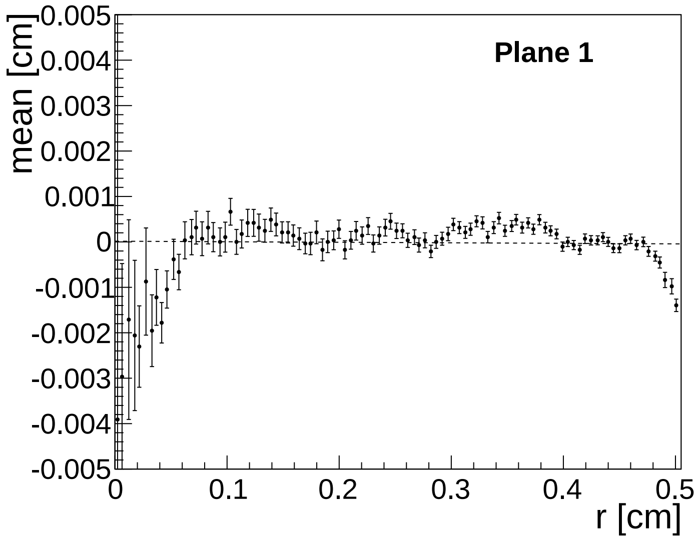

Figure 4.17 – Mean track to isochrone distance determined from the gaussian fits (shown for one bin in Fig. 4.16) as a function of the isochrone radius for the first double-layer.

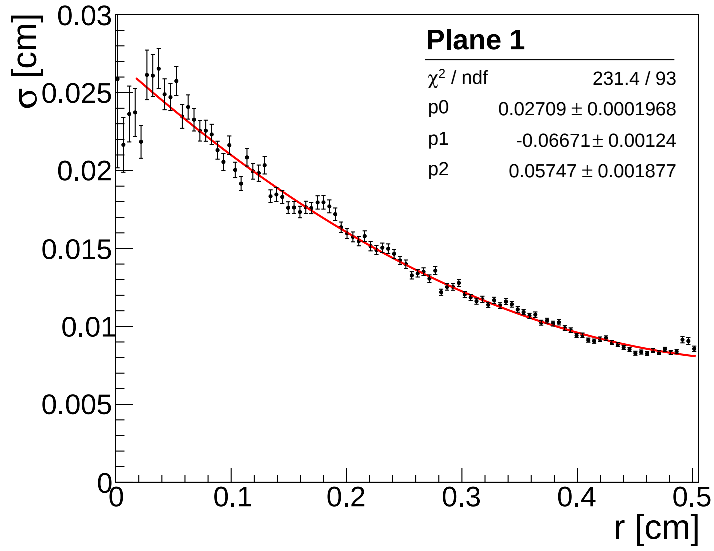

Figure 4.18 – Resolution of the determined drift distance for the first double-layer as a function of the isochrone radius. The distribution is fitted with a polynomial function of second order.

good precision. The resolutions obtained at 0.25 cm radius for each plane are collected in Tab. 4.1.

The average resolution over all planes is 146 μm. This is in good agreement with the expected value of about 150 μm [67].

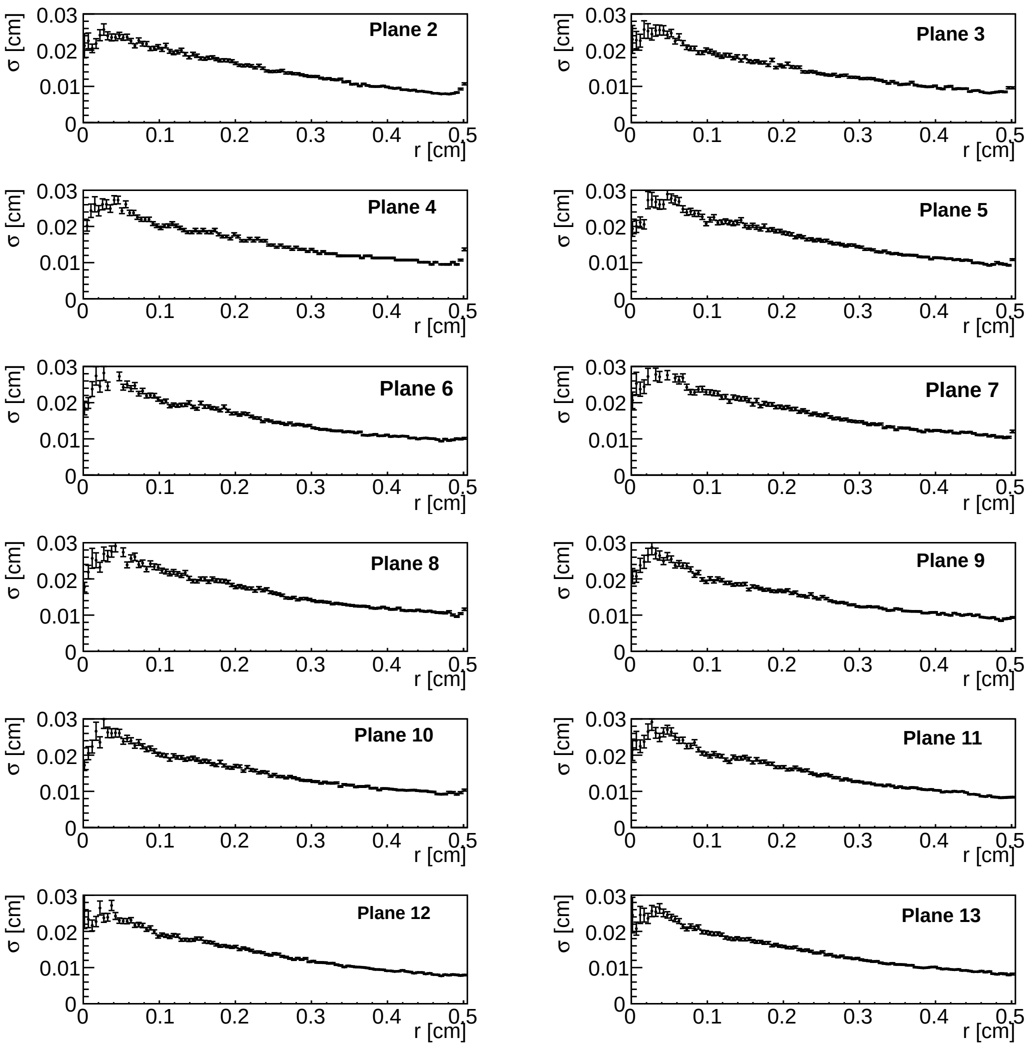

Figure 4.19 – Drift radius resolution determination for planes 2 to 13. No significant difference in the shape of the curves as well as in the absolute values of the spatial resolution is observed.

4.2 SQT Calibration

The calibration of the Silicon Quirl Tracker (SQT, see Sec. 2.2.2.1) positioning is done after track reconstruction with the STT and after pixel hit assignment to the reconstructed track as described in Ch. 5. Corrections to position and orientation of the SQT are determined as result of the minimization of the distances of closest approach between the tracks and their assigned SQT hits. Eq. (4.7) shows the minimized χ^2 function.

$$\chi^2 = \sum_{i=1}^{N} \frac{d_i^2}{\sigma_i^2} \tag{4.7}$$

where:

d_i - distance of closest approach between tracks and SQT hit.

σ_i - resolution of SQT hit position given by the geometrical width of the pixel, as illustrated in Fig. 4.20.

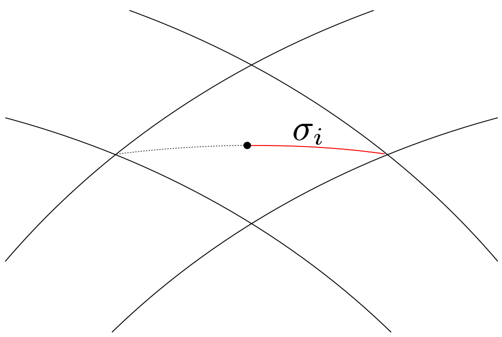

Figure 4.20 – Pixel geometry of the SQT. For the position resolution σ_i the geometrical pixel dimension is used.

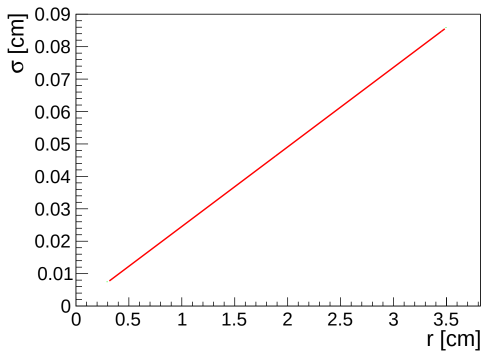

Figure 4.21 – Width of the SQT pixel as a function of the radius.

The width of the SQT hit is defined based on its geometry as:

$$\sigma = \frac{1}{2} \cdot \frac{2\pi r}{128} \tag{4.8}$$

where r is the distance between the center of the hit pixel and the center of the SQT subdetector, $r \in [0.3, 3.5]$.

The result of the minimization shows a deviation of position and orientation of the SQT from its nominal position and orientation as given in Tab. 4.2.

Δx [cm]	Δy [cm]	Δz [cm]	$\Delta\varphi_x$ [mrad]	$\Delta\varphi_y$ [mrad]	$\Delta\varphi_z$ [mrad]
0 ± 0.002	0 ± 0.002	0.045 ± 0.002	-4 ± 1	-11 ± 2	-28 ± 2

Table 4.2 – Correction to the nominal position and orientation of the SQT. Shifts in x and y direction are consistent with zero.

The correction of the SQT position and orientation provides significant improvement to the distance between the tracks and their assigned SQT pixel, as shown in Fig. 4.22. The blue distribution shows the distance before the correction, red one afterwards. The maximum of the corrected distribution is around $d = 400$ μm which is comparable to the dimension of the SQT pixel.

Taking into account the symmetry of the SQT subdetector, its position resolution in the x and y coordinate is determined as follows:

$$d = \sqrt{d_x^2 + d_y^2} \Rightarrow d_x = d_y = \frac{d}{\sqrt{2}} = 280\mu m \tag{4.9}$$

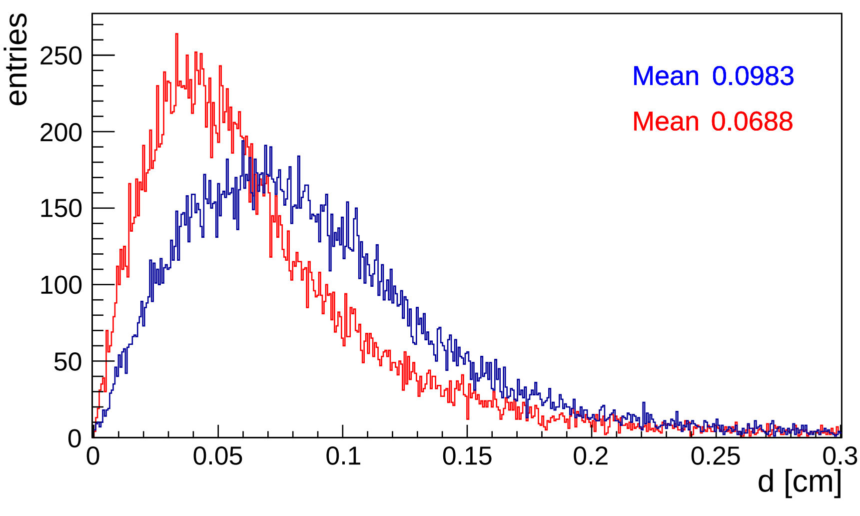

Figure 4.22 – Result the calibration of the SQT position and orientation. The blue distribution shows the distance between the track and the SQT hit before the correction, the red one afterwards.

Chapter 5

Event reconstruction

5.1 General Scheme

For all charged particles emitted within the detector acceptance the subdetectors of COSY-TOF provide information on the hit position in different regions of the detector volume. This information is used by track finder to identify the tracks. In the next step the tracks are fitted by the track fitter in order to improve the track position and direction to values as close as possible to reality, as it is allowed by position resolution of the subdetectors. The position and orientation of the detector components are calibrated in the iterative procedure as described in Ch. 4. After the tracks are fitted, the event finder is used to reconstruct the selected type of events.

5.2 Track Finder

The COSY-TOF detector delivers two different type of hits: pixel like hits and hits from the STT. The former provides three-dimensional space point information on the hits smeared by the pixel size, whereas the latter provides only the cylinder surface around the central anode wire of the straw tube with the isochrone radius based on the measured drift time. These very different types of information makes it complicated to use the STT together with the other subdetectors in the track finding procedure. However, in order to reconstruct charged particle tracks with the optimum efficiency and precision, both types of hit information have to be combined in the track finding algorithms.

Two different algorithms are used to find tracks in the most efficient and fastest way: a global track finder and a Hough track finder.

5.2.1 Global track finder

The STT can be considered as a structured combination of blocks. Each of such blocks consists of three double-layers of straw tubes rotated by an angle of 60° relative to each other around the beam axis. For the global track finding [68], the STT hits within each block are converted to pixel hits which then can be easily combined with the pixel hit information from other subdetectors.

If charged particles pass a block of the STT, the straws in each of the planes defined by the three double-layers fire. In the ideal case one straw per single layer and per particle delivers a signal (see Fig. 5.1). Neglecting the differences in the z coordinates

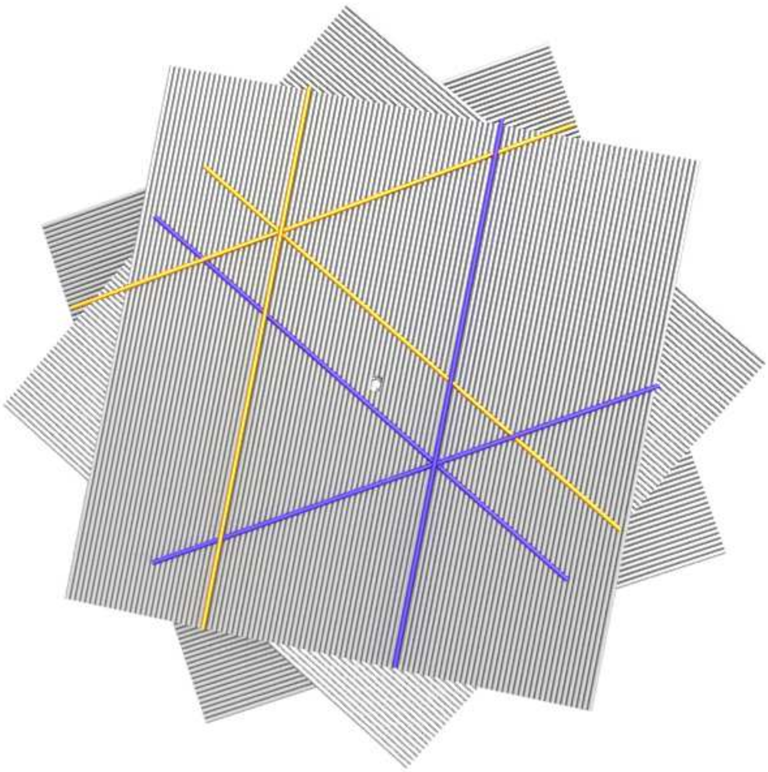

Figure 5.1 – Fired straws (colored) within one block for two incident charged particles.

of the different planes within one block, the intersections of the fired straws define a pixel hit. This hit has a transverse dimension given by the straw tube diameter of 1 cm. After repeating this procedure for all STT blocks and adding the obtained hit pixels to the hit pixels of the other subdetectors the tracks are searched as straight lines to which the given hits can be assigned in the optimum way.

5.2.2 Hough track finder

Hits based on isochrone information from three different orientations of straw double-layers are shown in Fig. 5.2. The axes u', v' and w' are perpendicular to the straws axes (u, v, w) and to the beam direction.

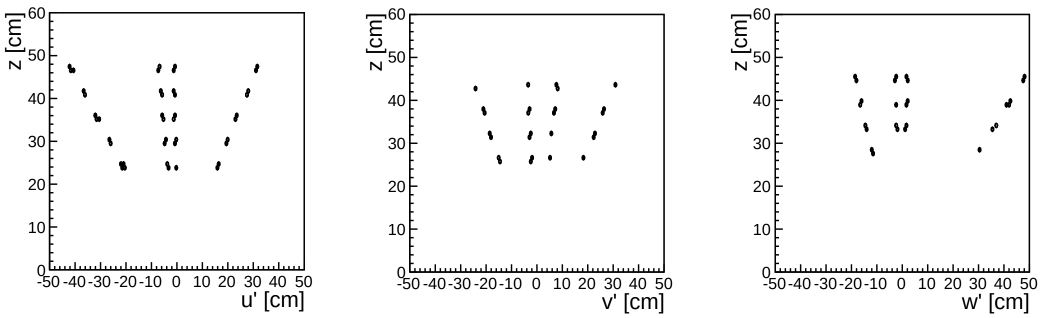

Figure 5.2 – Straw isochrones ordered into three projections corresponding to the three orientations of the straw double-layers. The axes u', v' and w' are perpendicular to the straw tube axes and to the beam direction. As an example a four-track event is shown.

To identify hits belonging to the same track the Hough method is used [69], [70]. Following this method, tangent lines to the isochrones of each hit straw are determined as illustrated in Fig. 5.3 by the dashed lines.

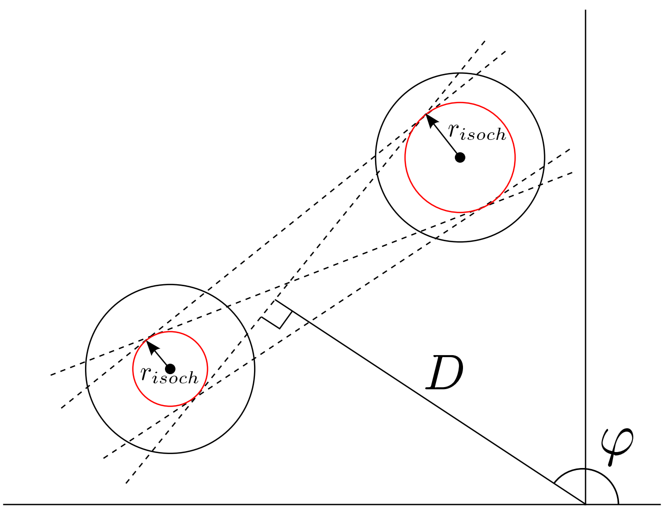

Figure 5.3 – D and φ parameters of Hough accumulator space.

Each obtained line is parameterized by the angle φ of its normal and by its distance D to the origin which is chosen to be the geometrical center of the STT. The equation of the tangent line corresponding to this geometry can be written as:

$$D = q\cos(\varphi) + z\sin(\varphi) \tag{5.1}$$

where q is u' ,v' ,w'. The parameter φ is restricted to the interval [0.2,2.8] radian in order to get a unique transformation between the q-z coordinate space and the D-φ Hough space. With this restriction, every line in the q-z plane corresponds to a unique point in the D-φ plane. The allowed value of the parameter D is also limited by the STT geometry to the range between -40 cm and 40 cm.

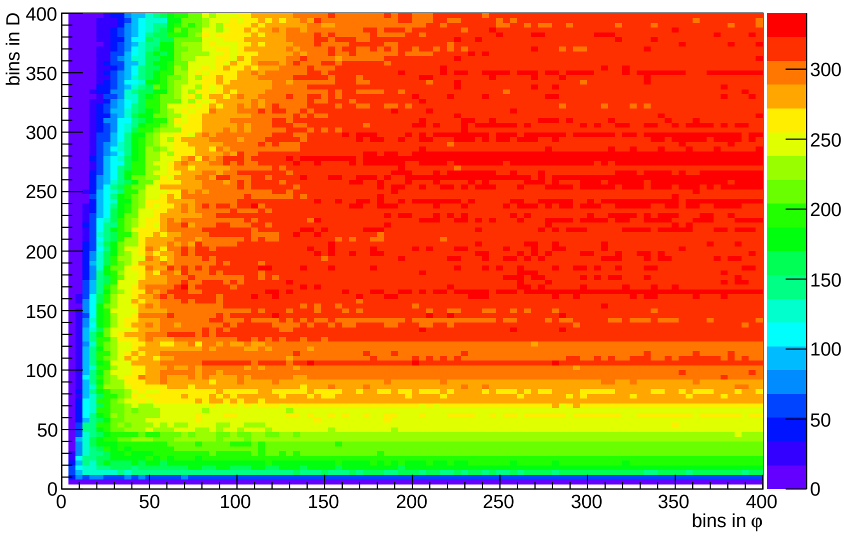

Figure 5.4 – Reconstruction efficiency in arbitrary units of pp elastic scattering events as a function of the D and φ binning. The "working point" is chosen as the combination (D,φ) = (140,150).

The Hough space is a two-dimensional accumulator with a bin size of $n \times m$. The binning of the accumulator is chosen small enough to ensure that overlap of contribution of different hits in Hough space is always small. On the other hand multiple scattering of charged particles distorts the trajectory causing a deviation from a straight line and, as a result, the hits lines can not overlap in a single accumulator point in Hough space if the bin size is too small.

The performance of the Hough method strongly depends on the number of bins in the accumulator. The time needed to fill the Hough accumulator is proportional to $N_{tracks} \times N_{\varphi bins}$, where N_{tracks} is the number of tracks and $N_{\varphi bins}$ is the number of bins in φ. Additional time is needed to find the maxima in Hough space, in the general case this time is proportional to $N_D \times N_{\varphi bins}$.

The analysis is done off-line. Therefore, the priority is devoted to the highest possible track finding efficiency together with the smallest background fraction. To find the optimum binning, a map of reconstruction efficiency as a function of D and φ binning is generated.

Fig. 5.4 shows this efficiency map for pp elastic scattering events. The tracks of the elastic scattering events are quite well separated in space. As a result, a fine binning is not required for their reconstruction. Fig. 5.5 shows the analogue efficiency map for the $pK_s\Sigma^+$ final state.

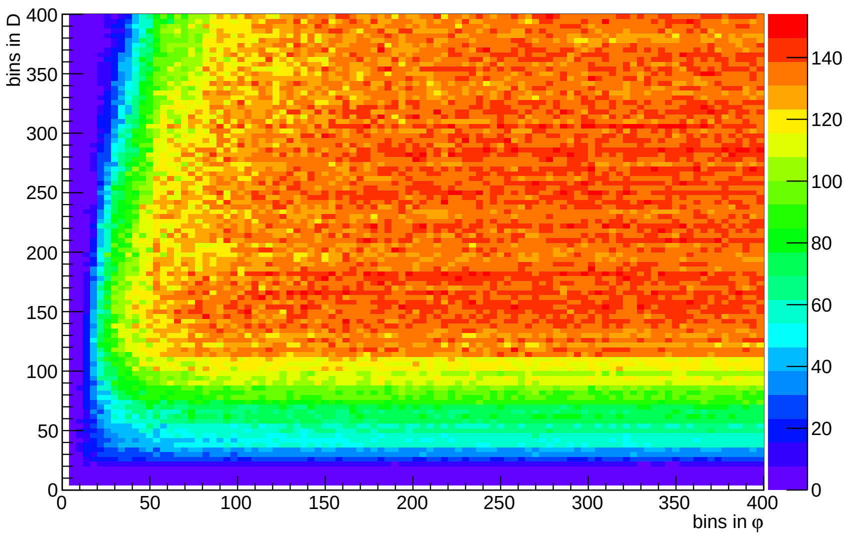

Figure 5.5 – Reconstruction efficiency in arbitrary units of $pp \rightarrow pK_s\Sigma^+$ events as a function of the D and φ binning. The ”working point” is chosen as the combination (D,φ) = (200,160).

The topology of $pK_s\Sigma^+$ events allows tracks to be close to each other and as a result a finer binning is needed to separate tracks, as can be seen from Fig. 5.5. A shift of the region with high reconstruction efficiency towards finer binning in D and ϕ as compared to pp elastic scattering events is observed. For a set of hits $\{(q_1, z_1), (q_2, z_2), ..., (q_n, z_n)\}$

Eq. (5.1) becomes:

$$D_i = q_i \cos(\varphi_i) + z_i \sin(\varphi_i) \tag{5.2}$$

Each hit (q_i, z_i) is transformed into a sinusoidal curve in D-φ space. Isochrones lying on the same line, that is these belonging to the same track, have a common intersection point in this space.

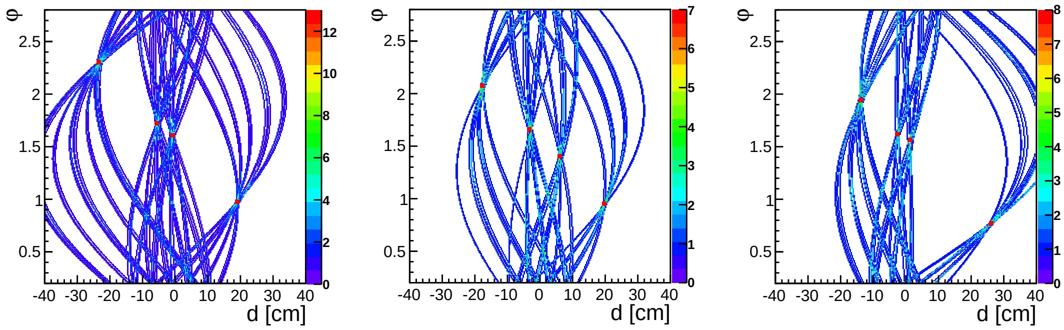

Figure 5.6 – Hough spaces for the three straw tube orientations: u' (left), v' (middle), w' (right). In each of the projections four maxima corresponding to four tracks.

Fig. 5.6 shows the Hough spaces for the three orientations of straw tube double-layers for the hit pattern of Fig. 5.2. Each track candidate emerges as a maximum in this plots. To suppress ghost tracks a lower threshold to the the maxima is applied. For accepted track candidate at least 4 entries are required.

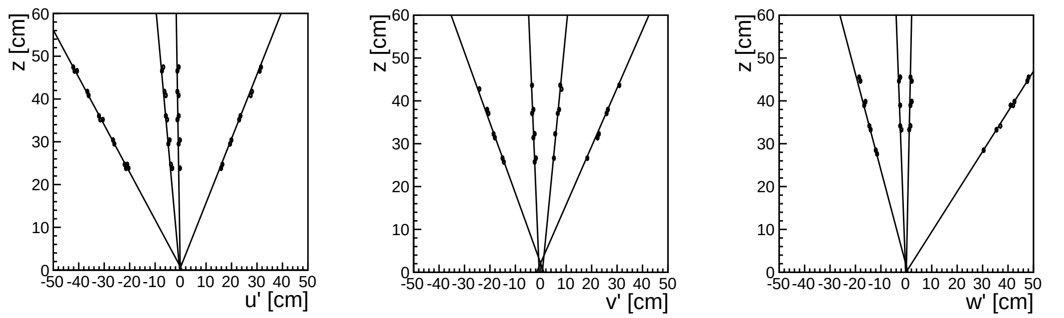

Figure 5.7 – Reconstructed track direction and the hits assigned to it. Track parameters are determined based on the maxima in Hough space.

Each point in D-φ space defines a straight line in the q-z space. Thus the maxima in D-φ space corresponds to lines which represent the track orientation in the corresponding projection. To improve the accuracy in defining the line directions they are fit to the assigned isochrone radii. At this stage the track direction is determined and the hit assignment is done only within the respective projection as shown in Fig. 5.7.

In the next step the track parameters need to be determined in three-dimensional space. To achieve this, each line in respective q-z space is transformed to a plane in 3D space. In the ideal case the intersection of the planes from all three projections results in one straight line which defines the track in 3D space, see Fig. 5.8. Since the STT has a finite position resolution and charge particle trajectories are effected by multiple scattering the planes do not intersect in one line, instead they always have three slightly different intersections. The geometrical average line of the three obtained intersecting lines is used as a track candidate.

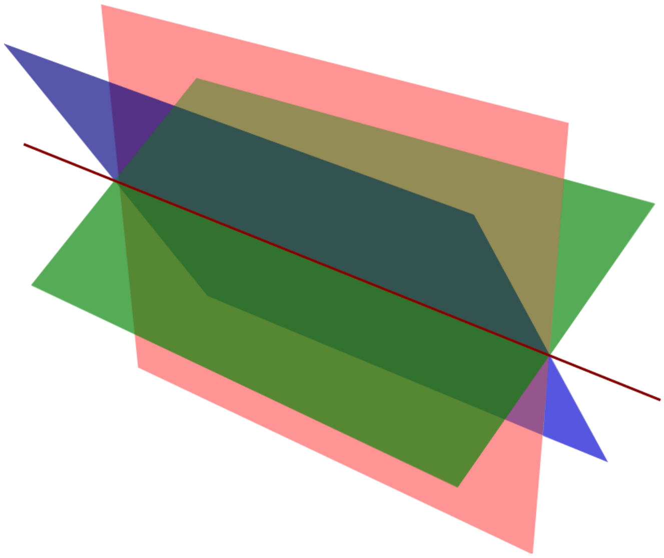

Figure 5.8 – A track in 3D space is defined as the intersection of the planes from all three projections.

If two maxima in the Hough space overlap in one of the projections, then the track is reconstructed from the intersection of the planes deduced from the two remaining projections.

When a proper intersection is found the hits from the planes which create the intersection are assigned to the 3D track as shown in Fig. 5.9 with different colors indicating the different tracks. At this stage the track parameters are determined and the STT hits are assigned to the tracks. The pixel hits from other subdetectors are assigned to the found tracks based on the distance of closest approach in the pixel

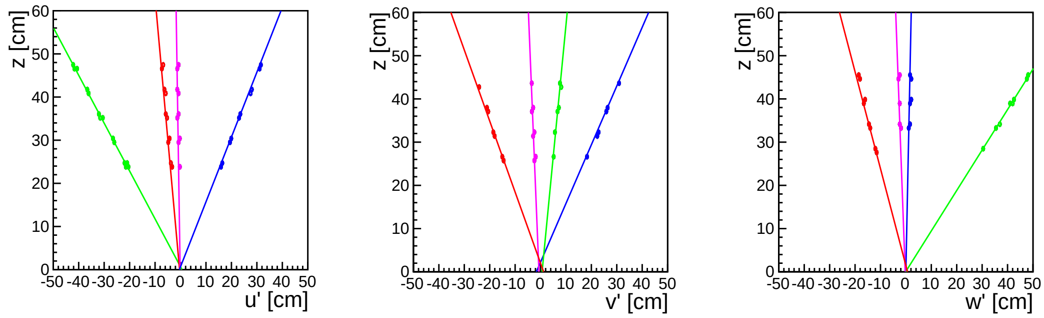

Figure 5.9 – Reconstructed track direction and the hits assigned to it for all projections. The colors denote different tracks.

subdetector plane between the center of the pixel and the determined track. The threshold value of 3 mm is used as a criteria of assignment.

5.2.3 Performance test

The Global Track Finder (GTF) and the Hough Track Finder (HTF) algorithms are tested for speed performance and for reconstruction efficiency with the different types of events. For the test a sample of 100,000 pp elastic scattering and $pK_s\Sigma^+$ MC events are used.

Track finder	pp elastic	$pK_s\Sigma^+$
Global track finder	4 ms	7 ms
Hough track finder	40 ms	70 ms

Table 5.1 – Comparison of the speed performance of different track finders (ms per event). The GTF is 10 times faster than the HTF for both kind of events. This test is performed with one 2.3 GHz core processor.

Tab. 5.1 shows the result of the speed comparison for one core of 2.3 GHz processor. In this test the GTF is 10 times faster than the HTF for both pp elastic scattering and $pK_s\Sigma^+$ events. The reconstruction efficiency test demonstrates high reconstruction efficiency for both algorithms in case of pp elastic scattering events and significantly different results for the $pK_s\Sigma^+$ events sample (Tab. 5.2).

The much smaller reconstruction efficiency of the GTF for $pK_s\Sigma^+$ events can be explained by the fact that this method does not use the isochrone radius information during the track finding. Instead it uses artificially created block pixels with an average dimension of about $1 \times 1\ cm^2$. Therefore, it is not able to separate tracks located close to each other. $pK_s\Sigma^+$ events have four tracks which are quite often located close to each other. pp elastic scattering events have two tracks which are well separated in space and as a result are well reconstructed by the GTF.

Track finder	pp elastic	$pK_s\Sigma^+$
Global track finder	97.9%	1.2%
Hough track finder	99.4%	21%

Table 5.2 – Comparison of the reconstruction efficiency of different track finders. The reconstruction efficiencies of the GTF and the HTF are comparable for pp elastic scattering events, while that of the HTF is much higher in case of $pK_s\Sigma^+$ events.

Based on the performed tests the Global Track Finder is the best choice for a fast track reconstruction of two track events. It can be used for online reconstruction of the elastic scattering events to monitor current experiment conditions like quality of hits, symmetries or beam polarization. The Hough Track Finder is slower but much more efficient for many-track events and it is used for further offline evaluation of the pp elastic scattering and the $pK_s\Sigma^+$ events.

5.3 Track Fitter

After a track has been found in three-dimensional space, the accuracy of the track parameters is improved by a track fitting procedure based on the drift time information, i.e. the isochrone radius of the STT hits, and the pixels position information from the SQT. Hits from other sub-detectors (Barrel, Quirl, Ring) are not used in the fitting procedure, since due to their large pixel dimensions they are not able to improve the precision of found tracks. The fit is done by minimization of the following function:

$$\chi^2 = \sum_{i=1}^{N^s_{hits}} \frac{(r_i - d^s_i)^2}{(\sigma^s_i)^2} + \sum_{i=1}^{N^p_{hits}} \frac{(d^p_i)^2}{(\sigma^p_i)^2} \tag{5.3}$$

where:

d_i^s is the distance of closest approach between the track and the wire of the hit straw:

$$d_i^s = \frac{[\vec{v} - \vec{w_i}]\vec{t} \times \vec{s_i}}{|\vec{t} \times \vec{s_i}|} \tag{5.4}$$

$\vec{v}$ and $\vec{w}_i$ are the directions of the track and of the straw axes, respectively;

$\vec{t}$ and $\vec{s}_i$ are the positions of the track and of the straw centers, respectively;

d_i^p is the distance of closest approach between the track and the center of the pixel hit:

$$d_i^p = \frac{|(\vec{h} - \vec{p_1}) \times (\vec{h} - \vec{p_2})|}{|\vec{p_2} - \vec{p_1}|} \tag{5.5}$$

r_i is the isochrone radius;

σ_i^s is the position resolution of the straw, different for each r_i;

σ_i^p is the dimension of the corresponding pixel hit;

N_{hits}^s and N_{hits}^p are the number of hits in the STT and the SQT, respectively;

$\vec{h}$ - x, y, z coordinates of pixel hit;

$\vec{p_1}$ and $\vec{p_2}$ are 3D points which define the track.

Fig. 5.10 shows two tracks zoomed in the STT region before and after the track fitting procedure.

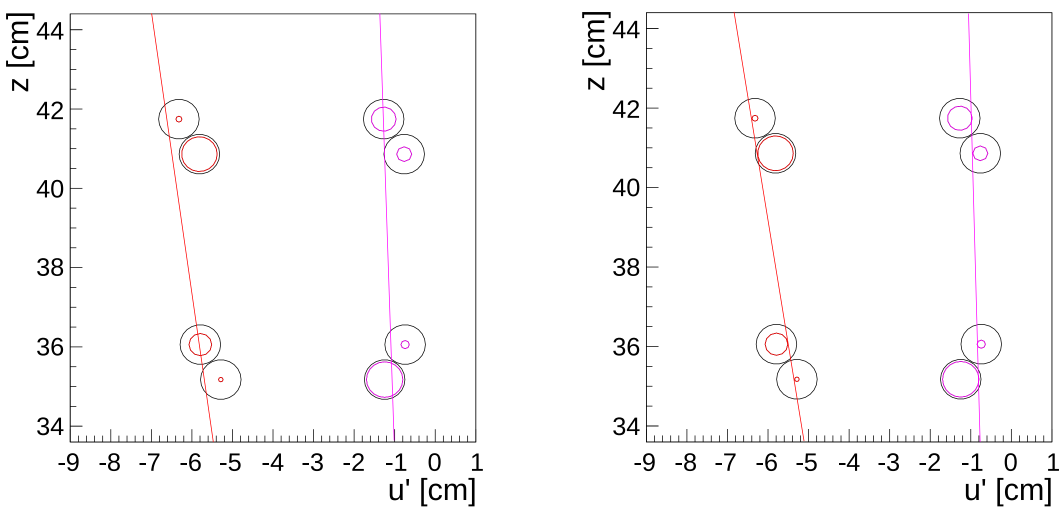

Figure 5.10 – Zoomed view of two tracks in the u' projection of the STT before (left) and after (right) track fitting.

5.4 Event Finder

The event finder uses fitted tracks to find the signature of a specified type of event. To distinguish different types of events and remove most of background the characteristic topology of searched events is used.

5.4.1 pp elastic scattering event finder

Elastic scattering events are reconstructed from the data taken with the elastic trigger (Sec. 2.3). The trigger significantly suppresses background events by recording only two-track events. For further selection, to each pair of tracks an upper limit on the distance of closest approach between the tracks is applied. The safety value of the limit of 0.5 cm is determined from further analysis (Sec. 6.1.3).

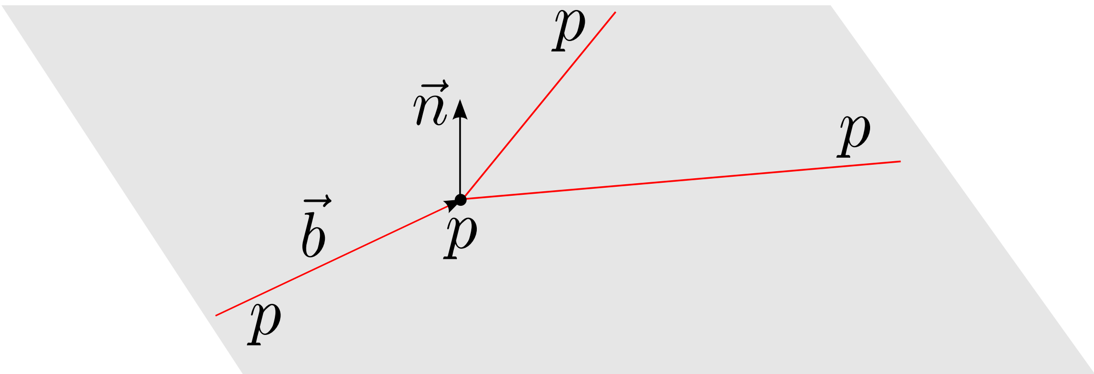

Figure 5.11 – The tracks of the two scattered protons lie in the same plane together with the beam axis.

Due to momentum conservation the scattered proton directions are coplanar to the beam direction (see Fig. 5.11). As a measure of coplanarity the following angle is taken:

$$\alpha_{copl} = \angle(\vec{n}, \vec{b}) - \pi/2 \tag{5.6}$$

where $\vec{n}$ is the normal to the plane of the two scattered protons; $\vec{b}$ is the direction of the beam. Events with α_{copl} more than 2° are discarded. Additionally, an upper limit of 4 cm on the z coordinate of the vertex position is used. Further selections are done after the event fitting procedure, see Sec. 5.5.1.

5.4.2 $pK^0\Sigma^+$ event finder

The general scheme of the $pK^0\Sigma^+$ event selection is demonstrated in Fig. 5.12. The reaction $pp \to pK^0\Sigma^+$ ($K^0 \to \pi^+\pi^-$, $\Sigma^+ \to p\pi^0$ or $\Sigma^+ \to n\pi^+$) has four charged particles in the final state. Fulfilment of this condition for a first-level event selection is done by taking events with hyperon trigger (Sec. 2.3). However, the number of tracks

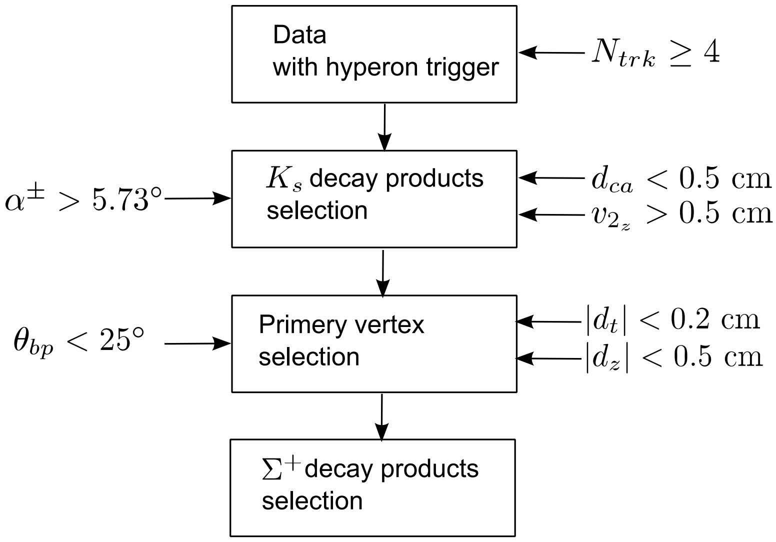

Figure 5.12 – General scheme of $pK_s\Sigma^+$ event selection. The selection criteria are explained in the text.

can be less then four due to false signals in the trigger or due to an insufficient number of hits to reconstruct some tracks. Such events are immediately discarded. As a next step the K_s decay vertex is searched. For this each pair of tracks with a distance of closest approach d_{ca} less then 0.5 cm is selected. Using the selected pairs, the point of closest approach between both tracks is calculated and used as the K_s decay vertex v_2 (Fig. 5.13). To exclude the possibility of mixing the obtained decay vertex with the primary vertex a lower limit on the distance of the decay vertex from the center of the target $v_{2_z} > 0.5$ cm is demanded.

A significant reduction of background and events with incorrect vertex selection is achieved by requiring a minimum-allowed value of 5.73° for the angles between the pions and the kaon directions $\alpha^{\pm}$. This also reduces the area of possible locations of the primary vertex v_1 as illustrated by shaded area in Fig. 5.13. As will be shown in Sec. 6.2.7 the selection of $\alpha^{\pm} < 5.73^o$ will result in a loss of less than 0.5% of signal events.

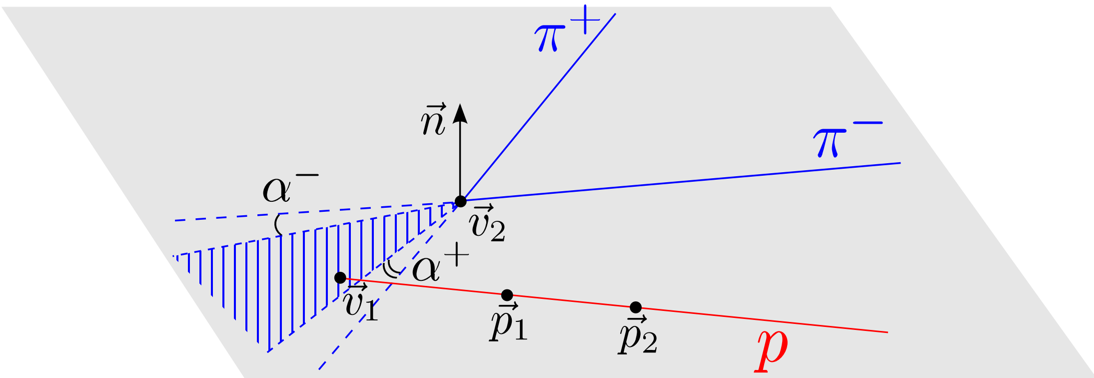

Figure 5.13 – Illustration to the $pK^0\Sigma^+$ finder algorithm. Two pions from K_s decay define a plane, the primary proton p intersects this plane in the point $\vec{v}_1$ which is the candidate for the primary vertex.

To find the primary vertex, the intersection of the kaon decay plane with the primary proton trajectory p is calculated:

$$\vec{v}_1 = \vec{p}_1 + \frac{\vec{n} \cdot (\vec{v}_2 - \vec{p}_1)}{\vec{n} \cdot (\vec{p}_2 - \vec{p}_1)}(\vec{p}_2 - \vec{p}_1) \tag{5.7}$$

where:

$\vec{p}_1$, $\vec{p}_2$ are the points which belong to the primary proton track;

$\vec{n}$ is the normal vector to the kaon decay plane.

As candidate for the primary proton the track with the smallest distance of closest approach to the target center is used. The condition on polar angle of the candidate of θ_{bp} less then 25°, which is the maximum kinematically allowed angle, is applied to suppress the background.

The location of the primary vertex is also limited by the geometrical dimension of the target. The latter is very well reproduced in the analysis of the pp elastic scattering events (Sec. 6.1.2). Using this, the following conditions on the distance between the calculated primary vertex v_1 and the geometrical center of the target are applied: $|d_t| < 0.2$ cm for the transverse component and $|d_z| < 0.5$ cm for the longitudinal component.

The direction of the K_s is determined from the positions of the primary and kaon decay vertex as follow:

$$\vec{d}_{K_s} = \vec{v}_2 - \vec{v}_1 \tag{5.8}$$

Finally, if more than one combination of tracks satisfies the above mentioned conditions, then the combination having the smallest distance of closest approach between the decay pions of the K_s is chosen.

5.5 Geometrical Event Fitter

5.5.1 pp elastic geometrical event fitter

In the pp elastic geometrical fitter the following constraints are used: the scattered particles share the same vertex and they are coplanar with the direction of the beam. These conditions are already approximately satisfied during the event finding procedure. The latter still allows a small deviation from the ideal condition due to the fact that the measured track direction deviates from the true direction within the detector resolution.

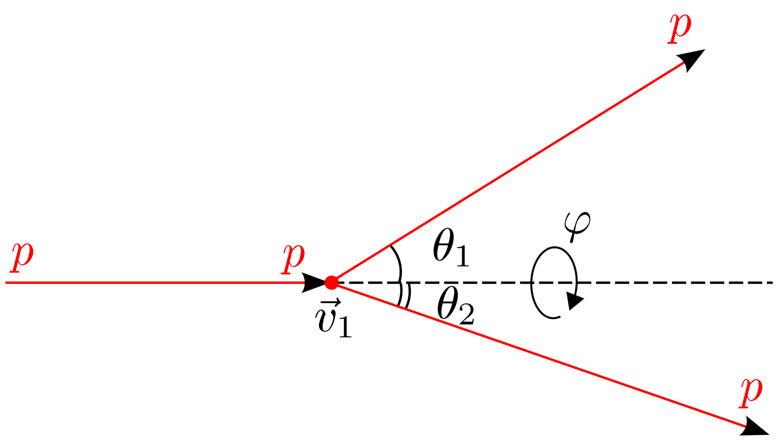

Figure 5.14 – Illustration of the pp-elastic geometrical fitter.

With the geometrical fitter the geometry of the pp elastic scattering event is forced to be correct and the fit itself defines how well the obtained geometry is fulfilled by the detector hits.

As fit parameters the vertex position $\vec{v}_1$, the angles between the scattered protons and the beam direction θ_1, θ_2, and the azimuthal angle φ of the plane defined by the scattered protons are chosen (Fig. 5.14). The fit is done by minimizing the following χ^2 function:

$$\chi^2 = \sum_{t=1}^{2} \left(\sum_{i=1}^{N_t^{shits}} \frac{(r_{ti} - d_{ti}^s)^2}{(\sigma_{ti}^s)^2} + \sum_{i=1}^{N_t^{phits}} \frac{(d_{ti}^p)^2}{(\sigma_{ti}^p)^2} \right) \tag{5.9}$$

where:

$$d_{ti}^s = \frac{[\vec{v}_1 - \vec{w}_i]\vec{t}_t(\theta_t, \varphi_t) \times \vec{s}_i}{|\vec{t}_t(\theta_t, \varphi_t) \times \vec{s}_i|}; \qquad d_{ti}^p = \frac{|(\vec{h}_i - \vec{v}_1) \times (\vec{h}_i - \vec{p}_t)|}{|\vec{p}_t - \vec{v}_1|} \tag{5.10}$$

where:

$\vec{v}_1$ is the vertex position; $\vec{p}_t$ is a point which belongs to the tth track; the other variables are identical to the ones from Eq. (5.3).

The resulting χ^2 distribution is discussed in Sec. 6.1.

5.5.2 $pK^0\Sigma^+$ geometrical event fitter

The geometry of the $pK^0\Sigma^+$ event is defined as follow:

- the two pions share the same vertex;
- the kaon lies in the plane defined by the pions;
- kaon and primary proton share the same vertex.

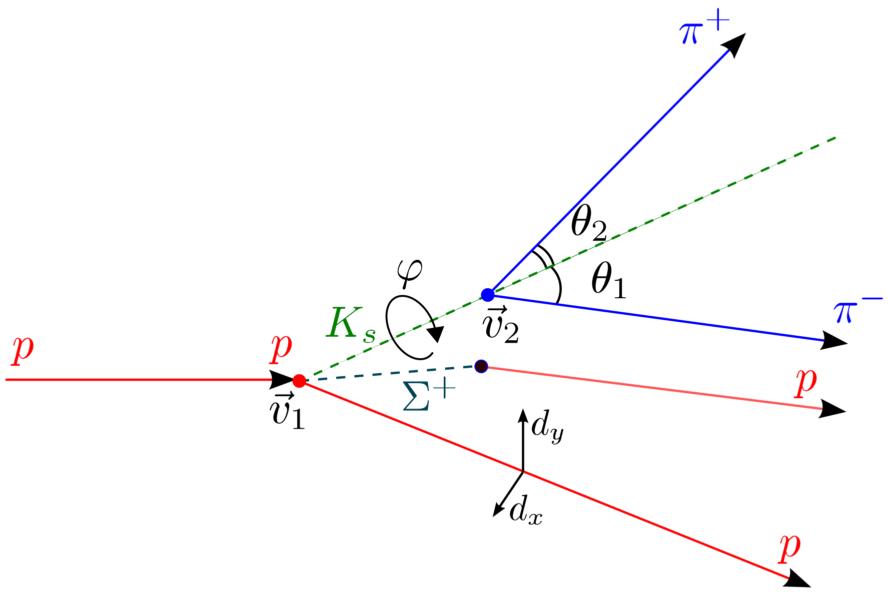

Figure 5.15 – Illustration to the $pK_s\Sigma^+$ geometrical fitter.

The fit procedure determines how well events with this geometry can be reproduced by the detector hits. As fit parameters the positions of the primary vertex $\vec{v}_1$ and kaon decay vertex $\vec{v}_2$, the angles of the pions with respect to the K_s direction θ_1, θ_2, and the azimuthal angle φ around the K_s direction of the plane defined by the pions are chosen (Fig. 5.15).

$$\chi^2 = \chi^2_{\pi^+\pi^-} + \sum_{i=1}^{N^s_{hits}} \frac{(r_i - d^s_i)^2}{(\sigma^s_i)^2} + \sum_{i=1}^{N^p_{hits}} \frac{(d^p_i)^2}{(\sigma^p_i)^2} \tag{5.11}$$

where: $\chi^2_{\pi^+\pi^-}$ is the χ^2 for the two pions calculated according to Eq. (5.9);

N^s_{hits} and N^p_{hits} are the numbers of straw and pixel hits created by the primary proton;

d^s_i and d^p_i is calculated based on Eq. (5.10) with $\vec{v}_1$ calculated by Eq. (5.7) where $\vec{p}_1$ and $\vec{p}_2$ are the functions of the primary proton direction.

The obtained χ^2/N_{dof} distribution for experimental data and for MC simulation is shown in Fig. 5.16. The distributions shows an excellent agrement with each

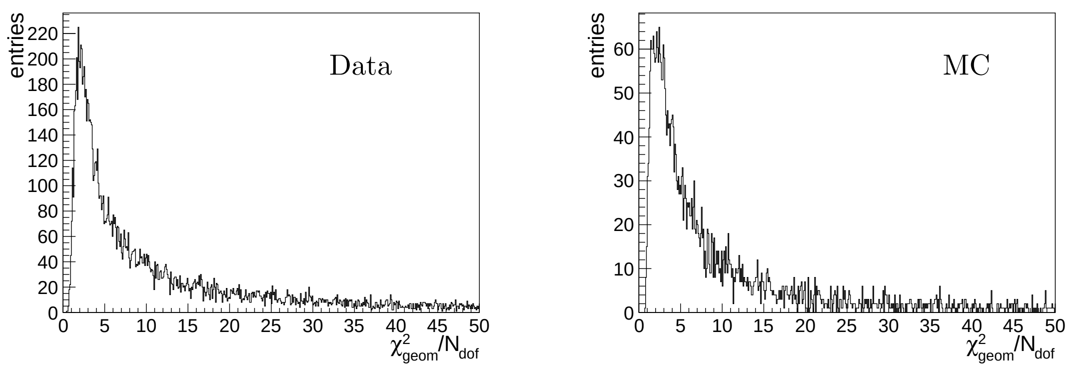

Figure 5.16 – The χ^2/N_{dof} distribution of the $pK^0\Sigma^+$ geometrical fit for the experimental data (left) and for the MC simulation (right). The peak of both distributions is at about 1.7.

other. The maximum of the χ^2/N_{dof} distribution is about 1.7 for both data and MC simulation.

5.6 $pK^0\Sigma^+$ Kinematical Event Fitter

In addition to the geometrical constraints, $pK^0\Sigma^+$ events have kinematical constraints which follow from momentum and energy conservation. These constraints are used to fit the measured values, in ideal case within their errors, to fulfill the required kinematic conditions. The χ^2 of the fit reflects the agreement between the fitted event and the detector response.

For the reason of simplicity, the kinematical variables of the $pK^0\Sigma^+$ events are evaluated in the center of mass system (CMS) of the initial state. With the knowledge of the initial state energy $\sqrt{s}$, the CMS momentum p^* of the $K^0 - \{p\Sigma^+\}$ system (Fig. 5.17) is calculated as:

$$p^* = \frac{1}{2\sqrt{s}} \left((s - (m_{K^0} + m_{p\Sigma^+})^2)(s - (m_{K^0} - m_{p\Sigma^+})^2)\right)^{\frac{1}{2}} \tag{5.12}$$

where m_{K^0} is the mass of K^0, and $m_{p\Sigma^+}$ is the invariant mass of the $p\Sigma^+$ system and is one of the fit parameters.

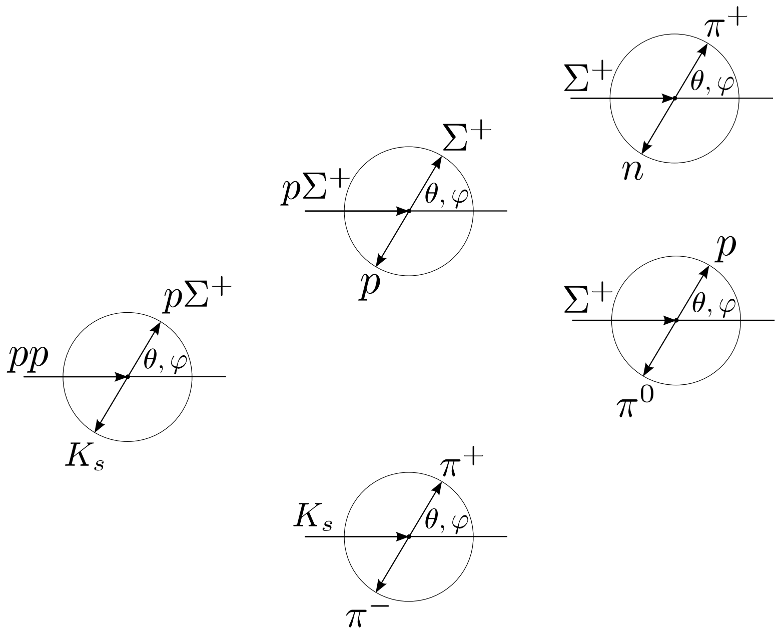

Figure 5.17 – Illustration to the $pK\Sigma^+$ kinematical fitter. The kinematic of the $pK\Sigma^+$ event is calculated as for the chain of two-body systems in CMS.

The direction of the momentum is set as a function of $\cos\theta$ and φ. The energies of the corresponding particles are calculated from:

$$E^*_{K^0} = \sqrt{m_{K^0} + p^{*2}} \qquad E^*_{p\Sigma^+} = \sqrt{m_{p\Sigma^+} + p^{*2}} \tag{5.13}$$

Knowing momentum and energy, the four-vectors of particles in the CMS are constructed and boosted by Lorentz transformation into the laboratory frame. The same procedure is done for the processes $K_s \to \pi^+\pi^-$ and $\{p\Sigma^+\} \to p\Sigma^+$. The Σ^+ decays with almost 100% into the two main daughter states $n\pi^+$ and $p\pi^0$. Both of them are tested during the fit and the one which yields the best agreement with the detector response is chosen. The obtained directions of the final state particles in the laboratory frame are fitted to the detector hits, which are given as isochrone radii for the STT and as pixel hits for the SQT.

As fit parameters the position of primary vertex, the mass of the $p\Sigma^+$ system, the decay length of K_s and Σ^+ as well as $\cos\theta$ and φ of all considered CMS subsystems are taken. All together this results in 14 fit parameters independent of the Σ^+ decay branch.

The start values of the kinematical fit are calculated from the track direction in the laboratory frame, boosted back into the CMS system. For this purpose the tracks obtained after the geometrical fit are used.

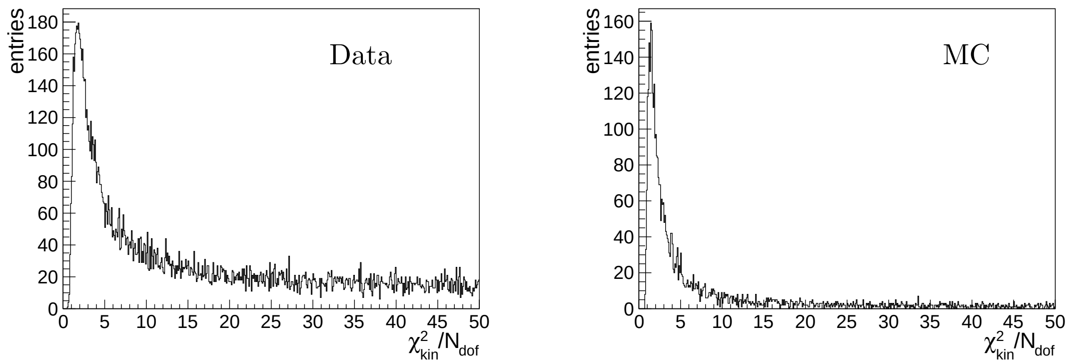

Figure 5.18 – The χ^2/N_{dof} distribution of the $pK^0\Sigma^+$ kinematic fit for the experimental data (left) and for the MC simulation (right). Both distributions peak at about 1.5.

The χ^2/N_{dof} distribution of the kinematical fit for the experimental data and for MC simulation is shown in Fig. 5.18. The maximum of the χ^2/N_{dof} distribution is at 1.5.

The values of the kinematical and the geometrical fit can not be compared directly in this case. The geometrical fit uses only three tracks during the fit while the kinematical fit uses all four tracks. As a result the χ^2/N_{dof} of the kinematic fit can be smaller than that of the geometrical fit.

5.7 Resolution

The precision of the reconstruction is determined by simulating and reconstructing 200,000 $pp \to pK^0\Sigma^+$ events. For this study an upper limit on the χ^2/N_{dof} of geomet-

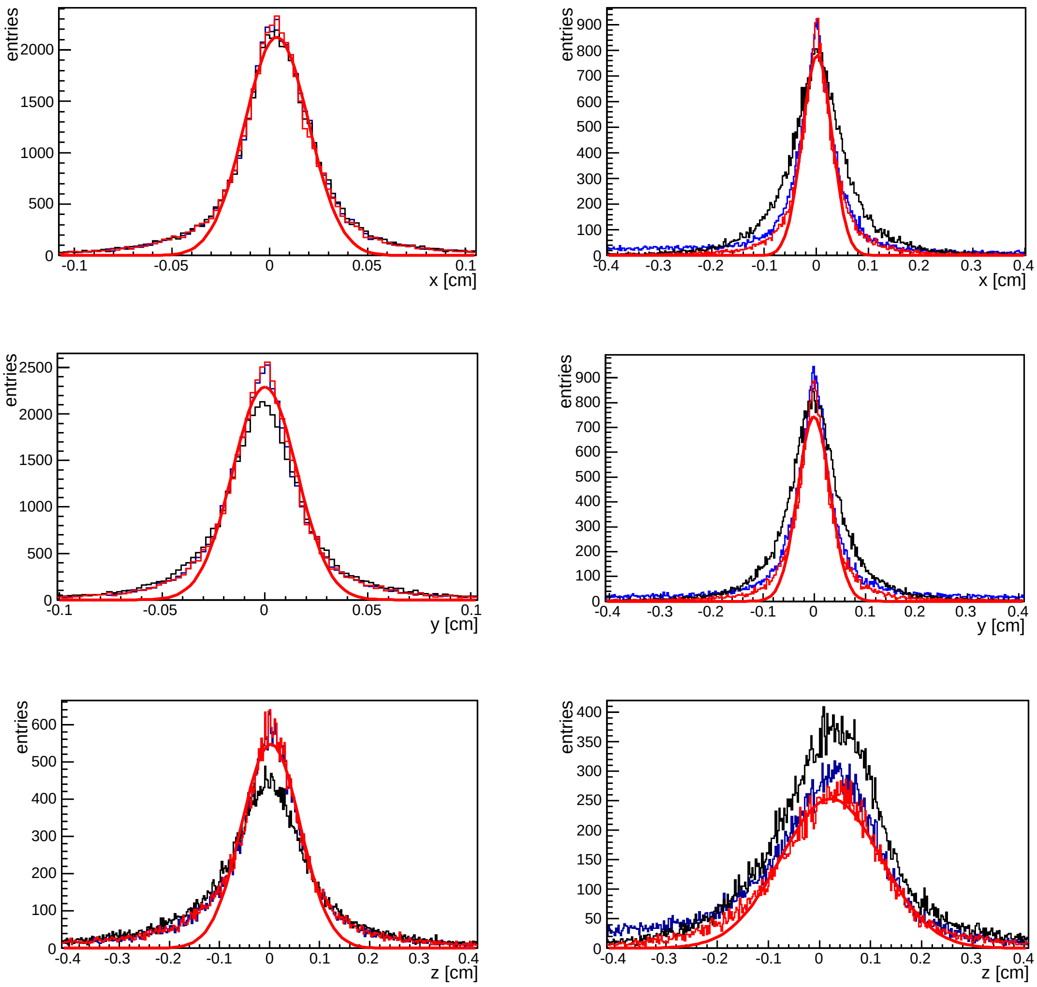

Figure 5.19 – The resolution ($v(x, y, z) = v_{mcreco} - v_{mc}$) of the primary vertex (left column) and the K_s decay vertex (right column). The black line depicts the distribution of unfitted events. The blue and the red lines depict the geometrically and kinematically fitted events, respectively. Note that the transverse component of primary vertex have different scale comparing to others.

rical and kinematic fit of 10 is applied. Fig. 5.19 demonstrates the resolution of the primary vertex (left column) and the K_s decay vertex (right column) by the difference of reconstructed and simulated vertex positions $v_{mcreco} - v_{mc}$. The black line depicts the unfitted distribution of $pK^0\Sigma^+$ event candidates, while the blue and the red lines denote the geometrically and kinematically fitted event candidates, respectively. The transverse components of the primary vertex position are not significantly improved by the fit procedure, in contrast to the z position. The fit also improves the position of the K_s decay vertex.

The number of events in the peak of the K_s decay vertex is different for unfitted and for fitted events. This can be explained by the fact that some of the event candidates are not able to describe the topology of $pK_s\Sigma^+$ with $\chi^2 < 10$.

The distributions of kinematically fitted events are fitted with a gaussian function (red lines). It yield a proper description of the peak region, while the tails of the distributions, which can be caused by the multiple scattering, have a non-gaussian shape. The standard deviations obtained from the fits are collected in Tab. 5.3.

Type of vertex	x [μm]	y [μm]	z [μm]
Primary vertex	167 $\pm$ 1	158 $\pm$ 1	581 $\pm$ 4
Kaon decay vertex	294 $\pm$ 3	305 $\pm$ 3	831 $\pm$ 5

Table 5.3 – The resolution $v_{mcreco} - v_{mc}$ of the primary vertex and the K_s decay vertex based on MC studies.

The momentum resolution is studied under the same conditions as the vertex resolution. The relative resolutions $(p_{mcreco} - p_{mc})/p_{mc}$ for the final state particles of the reaction $pp \to pK_s\Sigma^+$ are shown in Fig. 5.20. Again, the black, the blue and the red

Parameter	p	$\pi^\pm$	K_s	$p \mid\mid \pi^+$	Σ^+
σ %	0.69	1.27	0.55	0.93	0.59

Table 5.4 – Momentum resolution $(p_{mcreco} - p_{mc})/p_{mc}$ of the final state particles of the reaction $pp \to pK^0\Sigma^+$ based on MC simulation studies.

lines depict the distributions of unfitted, geometrically and kinematically fitted events, respectively. The geometrical fit does significantly improve the momentum resolution of pions and slightly of K_s but it does not make evident influence on the primary proton and on the hyperon. This difference follows from the fact that the K_s and pions momenta are calculated using only the geometry of the K_s decay, while the momenta of the other particles are calculated based on the topology of the whole event (see Sec. 6.2). The primary proton and the Σ^+ resolutions are considerably improved after the kinematical fit. The corresponding deviations σ of the distributions are collected in

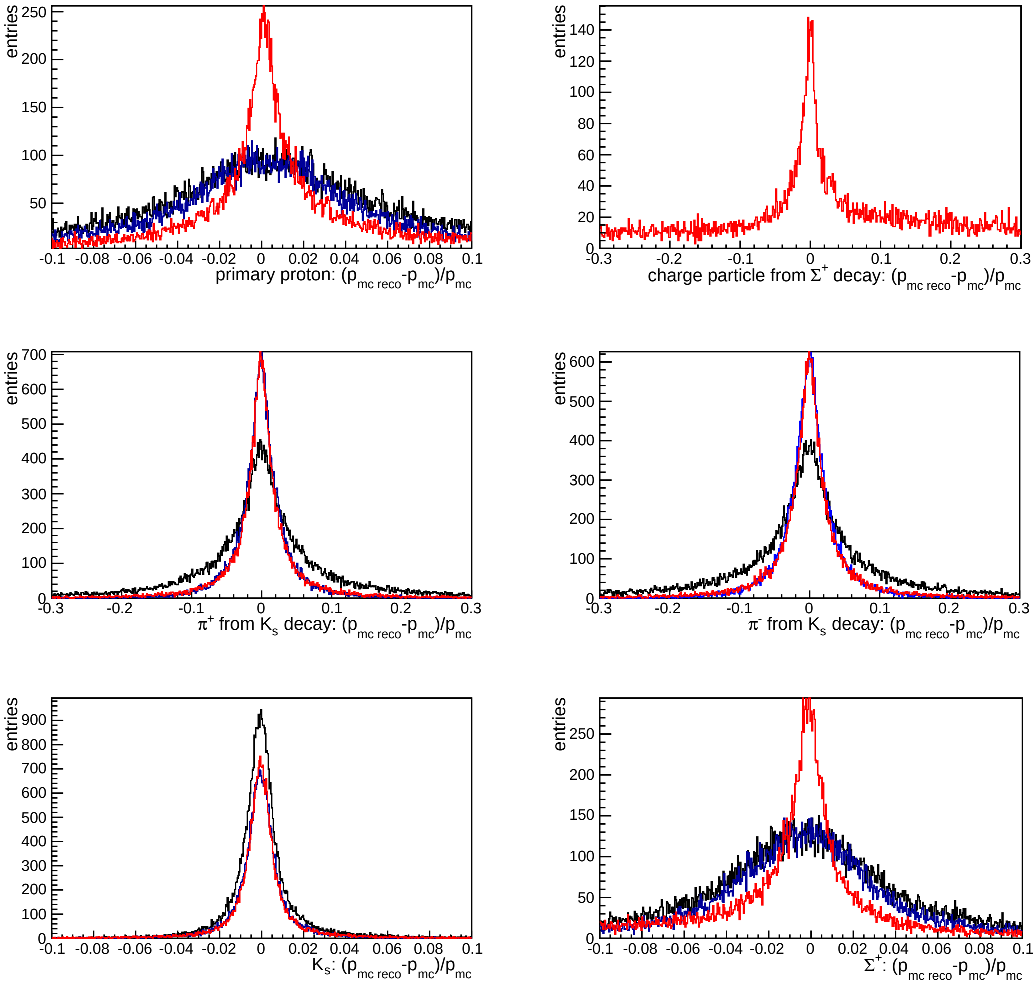

Figure 5.20 – Momentum resolution of the final state particles of the reaction $pp \to pK^0\Sigma^+$. The resolution of the primary proton (top left), the charged products of the Σ^+ decay (p and π^+) (top right), the π^+ (left) and π^- (right) of the K_s decay (middle row), K_s (bottom left) and Σ^+ is shown. The black line depicts the distribution of unfitted events. The blue and the red lines depict the geometrically and kinematically fitted events, respectively. Note that the distributions have different scales.

Tab. 5.4.

The achieved momentum resolutions are significantly better than the resolutions provided by time-of-flight measurements (see Fig. 2.4 in Sec. 2.2.1).

5.8 Implementation

5.8.1 From ASCII to ROOT data format

The data recorded during the experiment are stored to the hard disk in ASCII data format. For each hit the detector id, the element id, TDC and ADC values are stored. Such a format has several disadvantages: firstly the data are not compressed [1] and secondly, what is more important, if one needs only a few events from the end of the file, then one has to read all events before in the file [2].

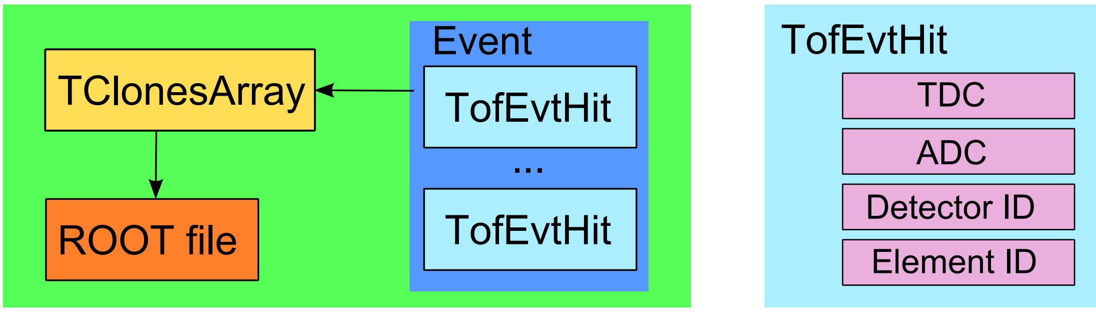

Figure 5.21 – Block scheme of the new data format.

To overcome these problems the ROOT data format is used. This format supports compression and allows to access data directly. Fig. 5.21 shows the structure of the proposed and used data format.

5.8.2 COSY-TOF reconstruction and analysis framework

The existing analysis software tof++ [71] worked well for previous measurements of COSY-TOF despite its complexity. However, the installation of the SQT and the STT and the necessity for the development of new reconstruction and analysis algorithms require a better organized solution. This solution should incorporate several underlying principles:

[1]in 40 min the COSY-TOF experiment produces about 4 GB of data

[2]line-by-line reading along of 4 GB text file requires about several minutes

- be easily extendable by new algorithms;
- have as simple as possible structure;
- have a functional data manager for reading and writing data;
- be easy to test and debug.

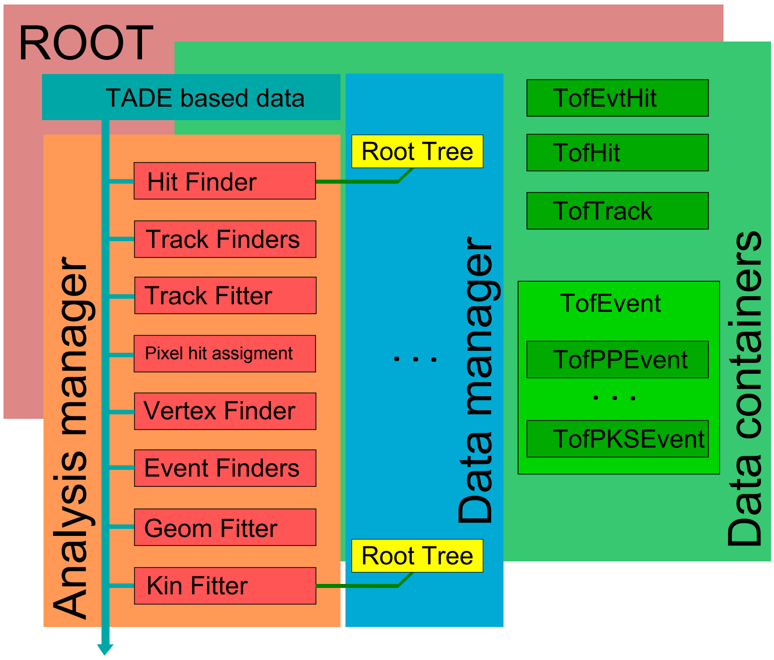

Figure 5.22 – Block scheme of the COSY-TOF analysis framework.

All these requirements are implemented in the COSY-TOF analysis framework which is developed as a part of the current work. As a basis for this framework parts of the ROOT [65] and FairRoot [72] frameworks are used. The block scheme of the COSY-TOF analysis framework is demonstrated in Fig. 5.22.

There are three main logical units: the analysis manager, the data containers and the data manager.

5.8.2.1 Analysis manager

All reconstruction and analysis algorithms are organized into tasks. Each task can be an independent unit as well as a combination of other tasks. The basic task class **TofTask** is inherited from ROOT's **TTask**. All algorithm tasks are derived from **TofTask**. The following tasks are implemented in the scope of this work:

- **TofHitFinderTask** reconstructs hits coordinates from hit detector elements based on the detector geometry. The task uses parts of the tof++ [71] software. Besides of hit finding the task is also responsible for pixel hit assignment to the tracks reconstructed with the STT.
- **TofTrackFinderLTask** is an implementation of the Global track finder (Sec. 5.2.1)
- **TofTrackFinderHTask** is an implementation of the Hough track finder (Sec. 5.2.2). The implementation of Hough space is taken from the tofstraw library [73].
- **TofTrackFitterTask** is an implementation of the track fitter (Sec. 5.3).
- **TofEventFinderTask** is an implementation of the event finder for pp elastic scattering and $pK^0\Sigma^+$ events (Sec. 5.4).
- **TofGeomEventFitterTask** is an implementation of the geometrical event fitter for pp elastic scattering and $pK^0\Sigma^+$ events (Sec. 5.5).
- **TofKinKEventFitterTask** is an implementation of the kinematical event fitter for $pK^0\Sigma^+$ events (Sec. 5.6).

Each of the tasks has implemented three important methods: initialization, execution and finalization.

The analysis manager in the first step initializes all tasks, that is allocates space and registers data in the data manager. Then it loops over all events one by one executing tasks in the order they are added to the manager. At the end it finalizes all tasks, that is releases space and records additional data.

5.8.2.2 Data containers

Data containers are classes of objects within the analysis framework. They are inherited from **TObject** to make them serializable. The classes have different level of complexity depending on the type of data they manage. For example **TofEvtHit** is a simple class which manages lowest level detector information while **TofEvent** is a complex class which manages all information about event including pointers to other containers. A list of data containers can be seen in Fig. 5.22.

5.8.2.3 Data manager

The data manager is designed to provide an interface for writing and reading of registered data containers into memory or a ROOT file during the analysis. Registration of the data containers is done at the initialization of each task. During the execution registered data are recorded on event by event basis. If data are recorded in the ROOT file, then the ROOT class **TTree** is used to organize the output data into a tree-like data structure. This allows to navigate within the recorded data container with the ROOT browser.

5.8.2.4 Analysis macros

The analysis itself is managed by analysis macros. These macros specify the data which should be analyzed, the calibration files, the algorithms, etc. An example of the analysis macro in the COSY-TOF analysis framework is shown in Add. 2.

Chapter 6

Analysis

6.1 pp Elastic Scattering Events

The analysis of the pp elastic scattering events is used for the following purposes:

- Determination of the target dimensions. Precise knowledge of target size and position is needed to determine the selection criteria for $pK^0\Sigma^+$ reconstruction.
- Precise determination of the beam direction. This is important for the calculation of the $pK^0\Sigma^+$ event kinematics.
- Comparison of the accuracy of reconstruction based on the STT alone and on the combination of STT and SQT.
- Determination of the beam polarization which is needed to determine polarization observables in the reaction $pp \to pK^0\Sigma^+$.

As a basis for the selection of pp elastic scattering events, part of the experimental data taken with the elastic trigger (Sec. 2.3) were used. These data are reconstructed (Sec. 5.4.1) and fit with a geometrical fit (Sec. 5.5). From the event topology the kinematic variables are calculated. The absolute values of the scattered proton momenta are calculated as:

$$|p_{1,2}| = \sqrt{p_t^2 + p_{l_{1,2}}^2} \tag{6.1}$$

where p_t and $p_{l_{1,2}}$ are the transverse and longitudinal momenta of the scattered protons which are defined by momentum conservation as follows:

$$p_t = p_{beam}\frac{\tan\theta_1 \tan\theta_2}{\tan\theta_1 + \tan\theta_2}\ , \qquad p_{l_{1,2}} = \frac{p_t}{\tan\theta_{1,2}} \tag{6.2}$$

The momentum directions of the protons are determined as $\vec{p}_{1,2} = p_{1,2}\vec{d}_{1,2}$, where $\vec{d}_{1,2}$ are the measured directions of the first and the second track.

The event sample after the geometrical fit is not free from background processes. Background is due to the inelastic scattering of the beam in the target as well as any other physical reaction the final state of which either has two charged particle tracks or is reconstructed with two tracks as a result of the detector inefficiency or incomplete acceptance. The first step in selecting the pp-elastic candidates is a cut on the χ^2/N_{dof} of the geometrical fit. Fig. 6.1 shows the χ^2/N_{dof} distribution. The maximum is around 1.6 which is larger than for the single track fits (Sec. 5.3) due to constraints introduced by the pp-elastic geometry.

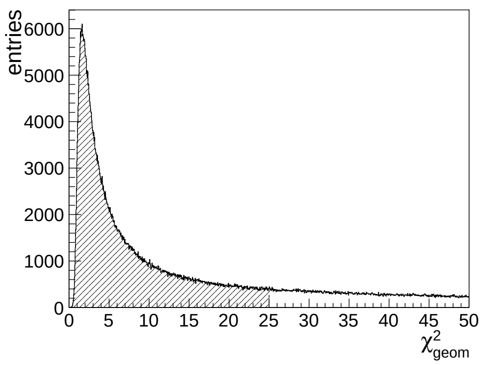

Figure 6.1 – χ^2/N_{dof} of kinematical fit of elastic events. The maximum of the distribution is around 1.6.

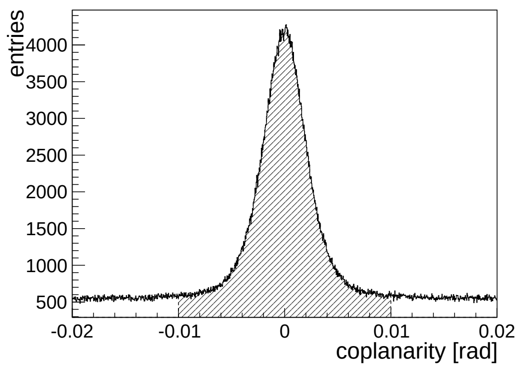

Figure 6.2 – Coplanarity of scattered tracks to the beam direction. The shaded area indicates selected events.

The shaded area up to $\chi^2/N_{dof} = 25$ indicates events which are accepted for further evaluation. The threshold is chosen quite loose to ensure that events affected by multiple scattering and by possible inaccuracy in the reconstruction procedure are not discarded.

The coplanarity requirement of the scattered protons to the beam direction as an important signature of the elastic events is used for their reconstruction and for their geometrical fit. The latter constrains the value of coplanarity α_{copl} defined by Eq. (5.6) to be exactly zero. Thus, the coplanarity distribution is plotted in Fig. 6.2 for events before the geometrical fit. The distribution is well described by a gaussian curve with $\sigma = (2.26 \pm 0.01)$ mrad. A loose threshold of $|\alpha_{copl}| < 10$ mrad is applied to remove of events which are not coplanar.

The result of this χ^2 and coplanarity selection illustrated in Figs. 6.1, 6.2 can be seen in Fig. 6.3 where the transverse versus longitudinal momentum of protons is plotted. A sharp elliptic band from 0.25 to 2.70 GeV/c in p_l indicates pp elastic scattering events. The two less intense bands show the $d\pi^+$ final state.

The pp-elastic ellipse is limited at small and large longitudinal momenta p_l by the acceptance of the STT which allows to fully reconstruct tracks with polar angle θ up to 52°.

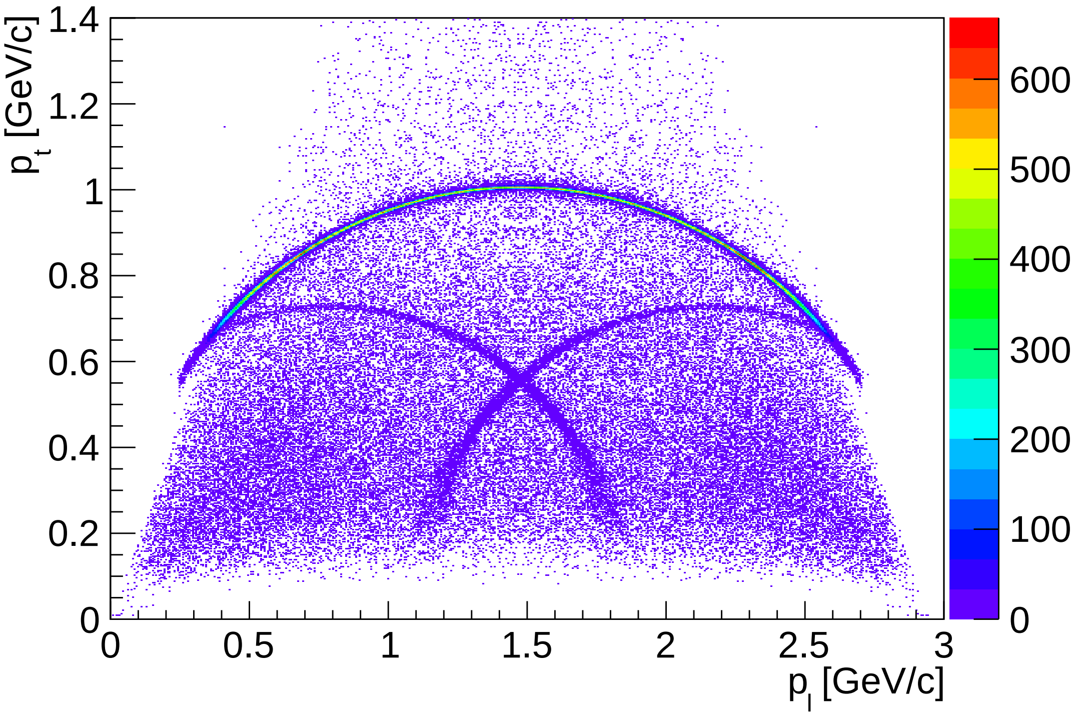

Figure 6.3 – Transverse versus longitudinal momentum of the pp elastic scattering candidates after χ^2_{geom} and coplanarity selection. The intense elliptic band indicates pp elastic scattering events. The two less intense ellipses correspond to the $d\pi^+$ final state.

For further extraction of the pp elastic scattering events a constraint on kinematical variables is applied. Due to the kinematics of a pp elastic scattering event δ defined as given in Eq. (6.3) should be equal to zero.

$$\delta = \tan\theta_1 \tan\theta_2 - \frac{1}{\gamma_{CM}^2} \tag{6.3}$$

The distribution of the quantity δ for all events is shown in Fig. 6.4 (left). The pp elastic scattering events are sharply distributed around zero while background events have a different distribution with a maximum at -0.415. The condition $|\delta| < 0.008$ to accept events satisfying the kinematics of pp elastic scattering is shown in Fig. 6.4 (right) with the shaded area.

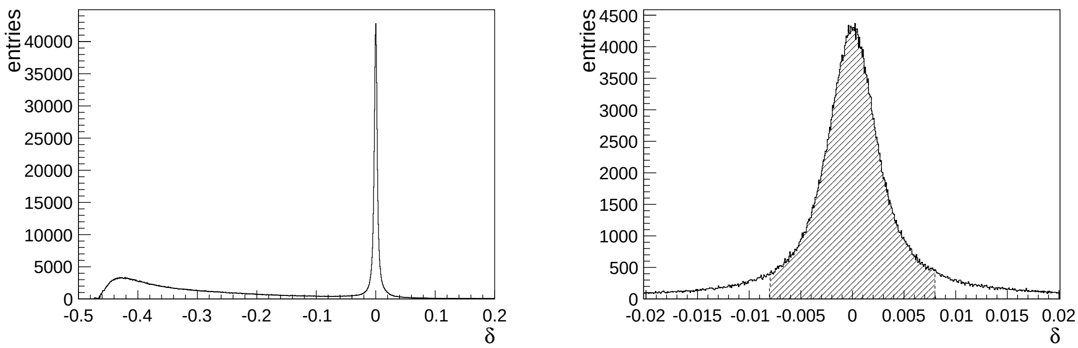

Figure 6.4 – Distribution of δ defined by Eq. (6.3); left - δ plotted for all pp elastic scattering candidates; right - zoomed view of the signal events from the left plot, the shaded area indicates selected events.

The distribution of the events in the p_t-p_l plane after applying conditions on χ^2, coplanarity and δ is shown in Fig. 6.5. A clean sample of 404,998 pp elastic scattering events remains. For further references this sample will be denoted as the "selected pp elastic scattering events".

Knowing the momenta and the masses of the scattered protons, a four-vector is constructed as $P_{miss} = (P_{beam} + P_{target}) - (P_1 + P_2)$. The energy component of the obtained four-vector determine the missing energy of the event.

Fig. 6.6 shows the missing energy distribution of the selected pp elastic scattering events. The distribution is well described by a gaussian fit with a standard deviation $\sigma = (2.474 \pm 0.005)$ MeV. With 8.5 keV, its mean value almost does not deviate from zero. Thus the precise correction of the distances d_l between the STT double-layers (see Sec. 4.1.2) is confirmed.

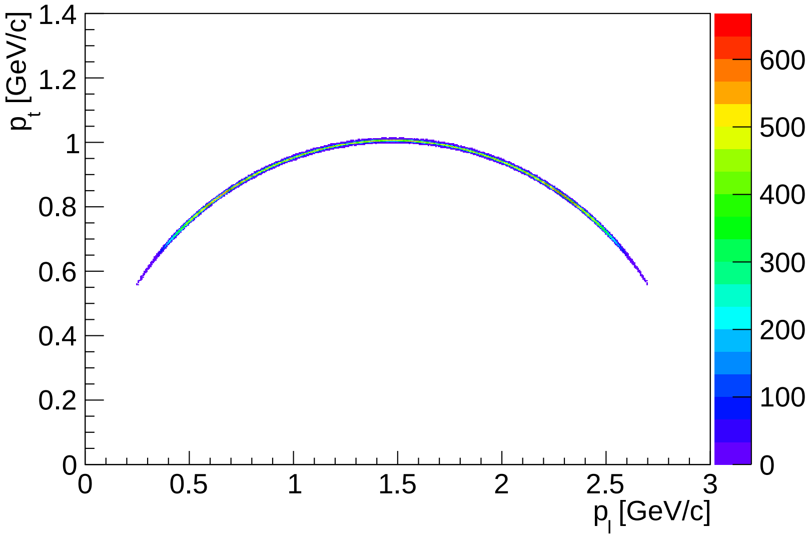

Figure 6.5 – Transverse versus longitudinal momentum of the pp elastic scattering candidates after applying the selection criteria on χ^2_{geom}, coplanarity and δ.

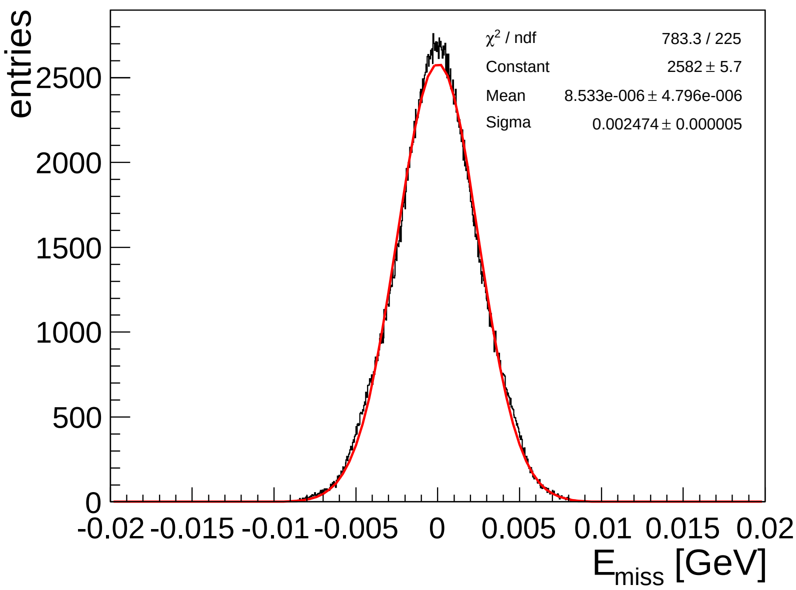

Figure 6.6 – Missing energy distribution of the selected pp elastic scattering events fitted with gaussian function.

The plotted missing energy is obtained after the correction of the beam direction, as discussed in the following section.

6.1.1 Beam direction

The precise knowledge of the beam direction is needed for the correct determination of the geometrical variables, e.g. coplanarity, as well as for the calculation of the kinematic variables of the pp elastic scattering and $pK^0\Sigma^+$ events. A deviation of the beam direction from the nominal value will induce systematic errors to the measurement. As the main contribution to the determined track direction based on information provided by the STT it is important to know the direction of the beam relative to the z-axis of the STT subdetector. Since the position and orientation of the SQT is calibrated relative to the STT it can not add additional systematic error to the measurement of the track direction.

Due to the coplanarity of the pp elastic scattering events the normal to the plane

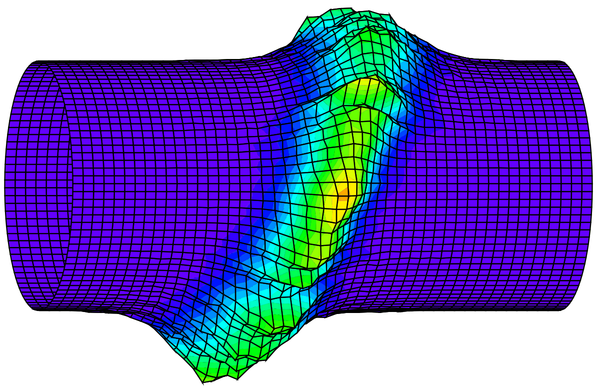

Figure 6.7 – Distribution of the normal directions to the pp scattering plane in a cylindrical coordinate system. The cylinder axis coincides with the nominal beam direction.

of the scattered protons should be perpendicular to the beam direction. A deviation of the normal from the perpendicular direction would demonstrate that beam axis is not parallel to the z-axis of the STT. Fig. 6.7 shows this deviations for pp elastic scattering events in a cylindrical coordinate system. The color indicates the density of the deduced normal directions. It is seen that the plane defined by the maxima of the density of normal directions is not perpendicular to the nominal beam axis, which coincides with the cental axis of the cylinder.

Fig. 6.8 (left) shows the deviation angle of the normal vector to the scattering plane defined by the two different protons from being perpendicular to the nominal beam direction as a function of the azimuthal angle φ. The distribution is fit with a sine function $\triangle\theta_{fit}\sin(n(\triangle\theta,\varphi)-\varphi_{fit})$ as indicated by the red line. The amplitude $\triangle\theta_{fit}=3.74\pm0.18$ mrad determines the most probable value for the tilt angle between the plane defined by the normals to the pp scattering plane and the plane perpendicular to the nominal beam direction, and thus the tilt angle between true z-axis of the STT and beam direction. The direction of the inclination is defined by the azimuthal angle $\varphi_{fit}=3.00\pm0.04$ rad. The obtained inclination is in good agreement with 3.69 mrad obtained in Ref. [26] where track reconstruction was based on the STT along.

The correction of the inclination effect can be either applied to the beam direction or to the orientation of the z-axis of the STT.

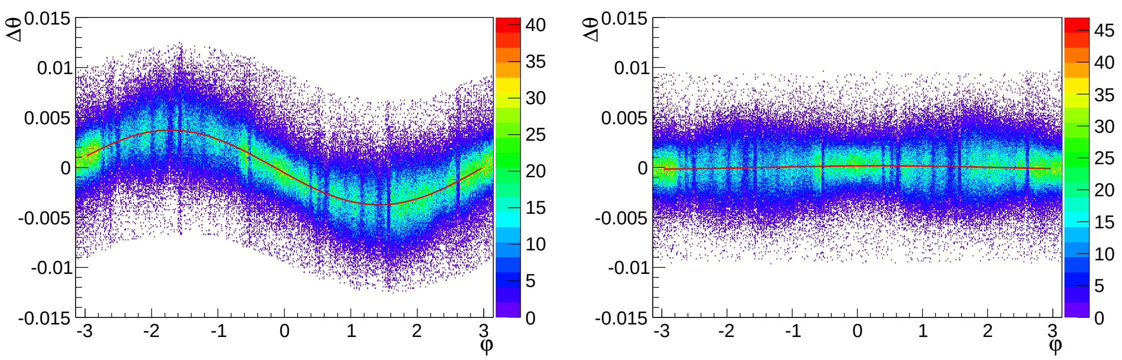

Figure 6.8 – Deviation angle between the normal vector on the pp scattering plane and the plane perpendicular to the nominal beam direction as function of the azimuthal angle φ; left - before correction; right - after.

To simplify the further evaluation of $pK^0\Sigma^+$ kinematics the true beam direction is assumed to be parallel to the z-direction of the COSY-TOF detector and the z-direction of the STT is corrected. Fig. 6.8 (right) shows the deviation angle of the normal vector after the correction.

6.1.2 Target dimension

Another important aspect in the analysis is the knowledge of the exact target dimension. This information is needed for the efficient reconstruction of the $pK^0\Sigma^+$ events as well as for background suppression. The vertex distribution of the selected pp elastic scattering events can be a good indicator of the target dimension. Fig. 6.9 (left) shows the vertex

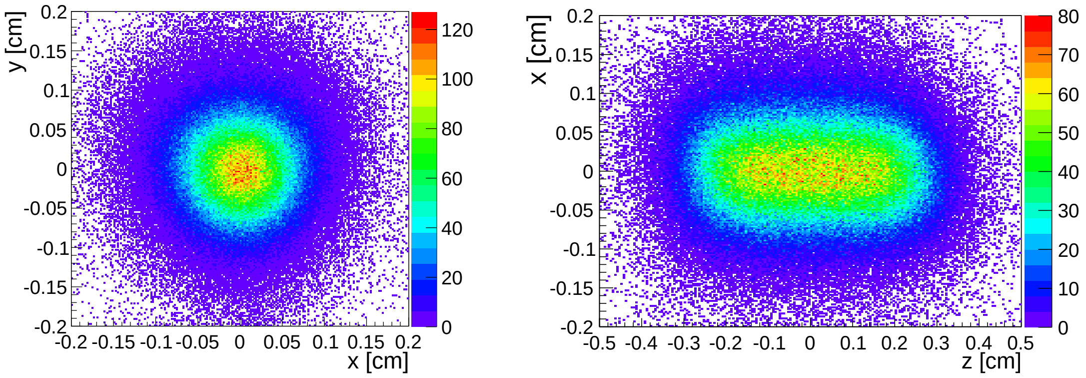

Figure 6.9 – The distribution of the vertices of pp elastic scattering events projected on $x-y$ plane (left) and on $z-x$ plane (right).

position distribution in a plane perpendicular to the beam. Colors indicate the density distribution of the vertices.

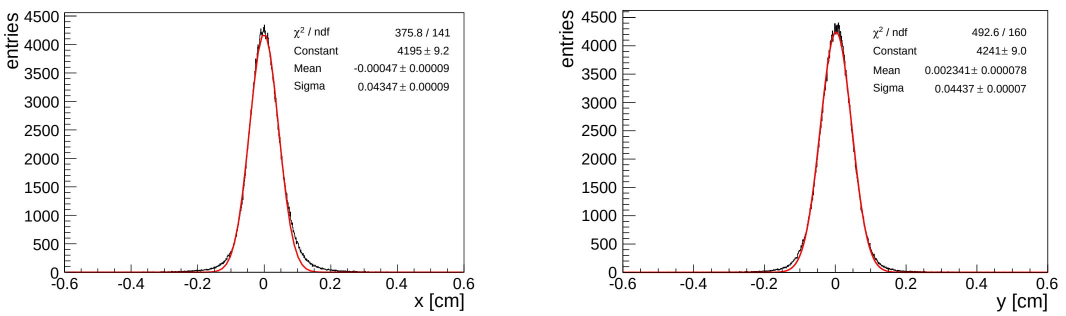

Figure 6.10 – The projection of the vertex distribution of pp elastic scattering events on the x axis (left) and on the y axis (right).

With the maximum at (0,0) the density distribution has an approximate radius of 0.5 mm. As the target radius is 3 mm we can conclude that the observed vertex distribution is a result of the interaction of the beam with only a part of the target. The transverse radius of this interaction region is a convolution of the beam size in the x-y plane with the resolution of the pp-elastic vertex determination in this plane.

Fig. 6.9 (right) shows the vertex distribution in the $z-x$ plane. In this projection the target borders are clearly seen at $z = \pm 2.5$ mm.

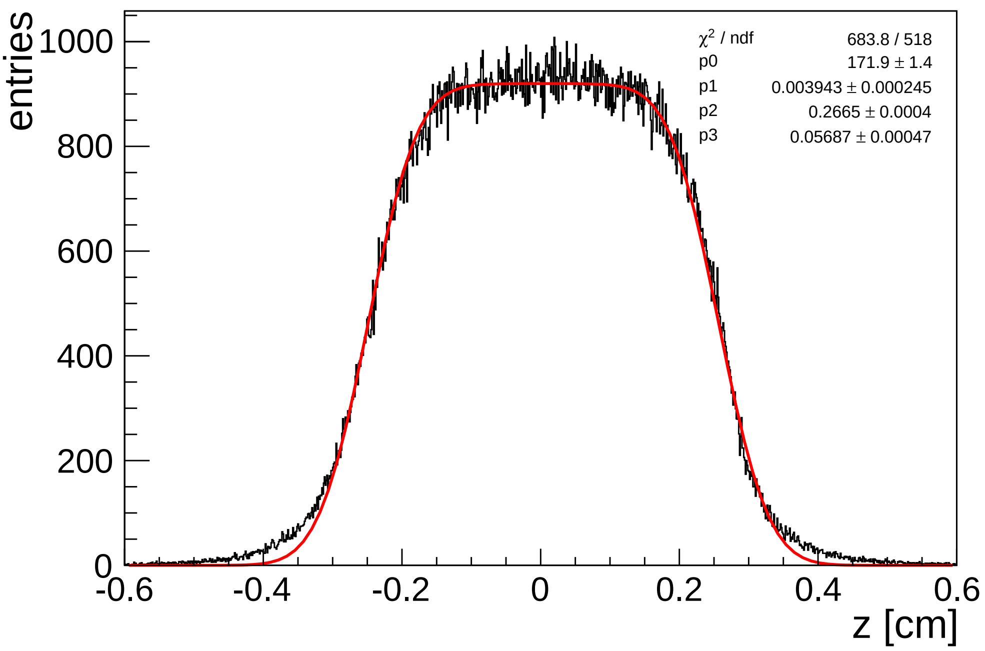

Figure 6.11 – The projection of the pp-elastic vertex distribution on the z axis. The red line shows the fit of the distribution with a convolution of box and gaussian function in the region $|z| < 0.3$ cm.

The projections of the vertex distribution on the x and y axes are shown in Fig. 6.10 left and right, respectively. Both of them are well described by a gaussian fit as indicated by the red line. For the x-projection a standard deviation $\sigma = (434.9 \pm 0.7)$ μm and for the y-projection $\sigma = (443.7 \pm 0.9)$ μm is found.

The σ width of the y-projection is 2.3% larger than that for the for x-projection. This can be explained by the stochastic beam extraction by which a higher emittance in the y direction is expected.

The projection of the vertex positions on the z axis is shown in Fig. 6.11. A fit with the convolution of a box and a gaussian function is shown as red line. The box function represents the target dimension and the gaussian the resolution of the vertex reconstruction. As we can see from the obtained χ^2/N_{dof} the convolution function perfectly describes the vertex distribution in the region [-0.3,0.3] cm. The tails which are not described by the fit are the result of multiple scattering. From the fit it is determined that the length of the target is (5.33 ± 0.01) mm and the resolution of the vertex reconstruction is $\sigma_z = (569 \pm 5)$ μm.

The exact position of the maximum density of the vertex distribution at the origin, that is point (0,0,0), is a result of the position correction of the STT.

6.1.3 Reconstruction accuracy with and without the SQT

As an additional task the improvement of the reconstruction accuracy by including the SQT is studied. For this purpose pp elastic scattering events are reconstructed with and without this subdetector, and the result are compared.

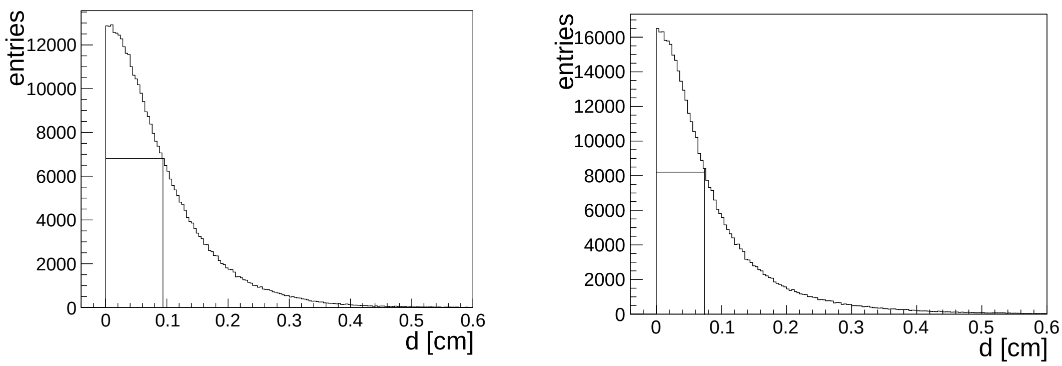

Figure 6.12 – Distance of closest approach d between the two tracks of selected pp elastic scattering events; left - reconstruction based on STT alone; right - based on both STT and SQT. The corresponding FWHM values are 1860 μm and 1480 μm.

An appropriate parameter in this comparison is the distance of closest approach between the tracks d which define a pp elastic scattering event. The parameter d is calculated before the geometrical fit, which implies $d = 0$. Fig. 6.12 shows the distribution of d for the selected pp elastic scattering events. On the left side the result of the reconstruction without SQT, on the right side that with the SQT is shown. The corresponding values of the FWHM are 1860 μm and 1480 μm, respectively. This equivalent to 22.8% improvement of the FWHM value. As a result of the improved reconstruction accuracy one obtains an improvement of the vertex resolution by 20.5%, 12.9% and 5.3% for σ_x, σ_y and σ_z, respectively.

As a consequence, the improvement of the geometrical accuracy results in an improvement of the obtained kinematic variables. For example, the resolution of the missing energy of pp elastic scattering events is 8.2% better when including the SQT.

Subdetectors	σ of Z (X,Y) vertex distribution [μm]	σ of E_{miss} [MeV]	Number of reconstructed events
STT	699 (495,468)	2.68	389,825
STT + SQT	569 (435,444)	2.47	404,998

Table 6.1 – Comparison of reconstruction accuracy with and without the SQT.

Tab. 6.1 summarizes the vertex and missing energy resolutions for events reconstructed with and without the SQT.

As an additional result of the improved reconstruction accuracy by including the SQT a higher number of events passes the selection procedure.

6.1.4 Beam polarization

The determination of the beam polarization is needed to determine polarization observables in the $pK^0\Sigma^+$ final state. The beam polarization can be deduced from the left-right azimuthal asymmetry $a(\theta^*, \varphi)$ of the scattered protons in the reaction $\vec{p}p \to pp$.

The polarization itself is defined as follows:

$$P_b = \frac{1}{A(\theta^*)} \frac{a(\theta^*, \varphi)}{\cos(\varphi)} \tag{6.4}$$

where

$A(\theta^*)$ is the analyzing power. It is well known from other experiments [74].

$a(\theta^*, \varphi)$ is the asymmetry defined as:

$$a(\theta^*, \varphi) = \frac{L - R}{L + R} \tag{6.5}$$

where

$$L = \sqrt{N^+(\theta^*, \varphi) N^-(\theta^*, \varphi + \pi)} \qquad R = \sqrt{N^-(\theta^*, \varphi) N^+(\theta^*, \varphi + \pi)} \tag{6.6}$$

where $N^{+}(\theta^{*}, \varphi+\pi)$, $N^{-}(\theta^{*}, \varphi+\pi)$ is the number of tracks produced with spin up (+) and down (-) in the specified region of θ^{*} and φ correspondingly.

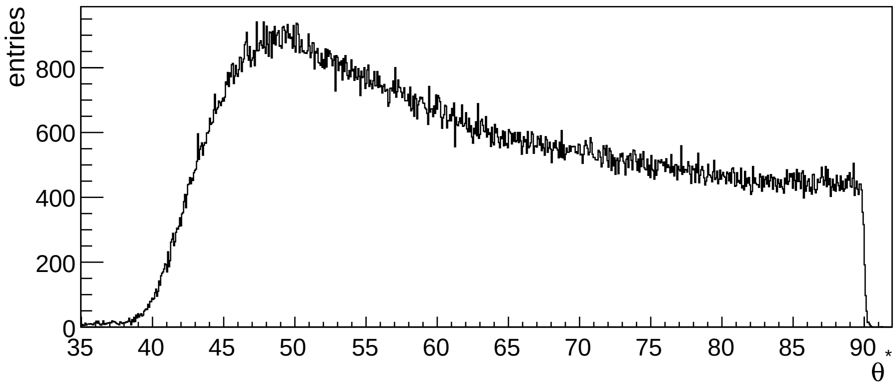

Figure 6.13 – The distribution of polar angle θ^{*} in the CMS. The angle θ^{*} is defined by the more forward scattered proton.

To find the dependence of the asymmetry on θ^{*} the distribution in Fig. 6.13 is divided into 12 bins between 42° and 90°. The azimuthal angle of the tracks in each θ^{*} bin is divided into 16 bins as shown in Fig. 6.14.

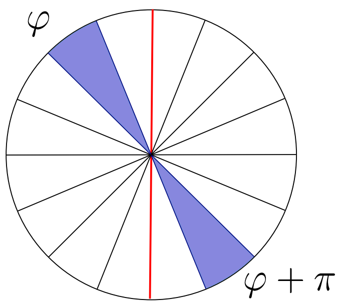

Figure 6.14 – Bins in azimuthal angle φ.

The resulting asymmetry $a(\theta^{*}, \varphi)$ according to Eq. (6.5) for each φ and θ^{*} bin is shown in Fig. 6.15. From Eq. (6.4) follows that for a fixed θ^{*} bin the $a_{\theta^{*}}(\varphi)/\cos(\varphi) = PA_{\theta^{*}} = const \equiv \overline{a}_{\theta^{*}}$. Therefore, the distribution of asymmetries for each θ^{*} bin is fitted with the function $\overline{a}_{\theta^{*}}\cos(\varphi)$, where $\overline{a}_{\theta^{*}}$ is the average asymmetry for the specified θ^{*} bin. The fit, shown by the red line in Fig. 6.15, agrees well with the data within the statistical uncertainty.

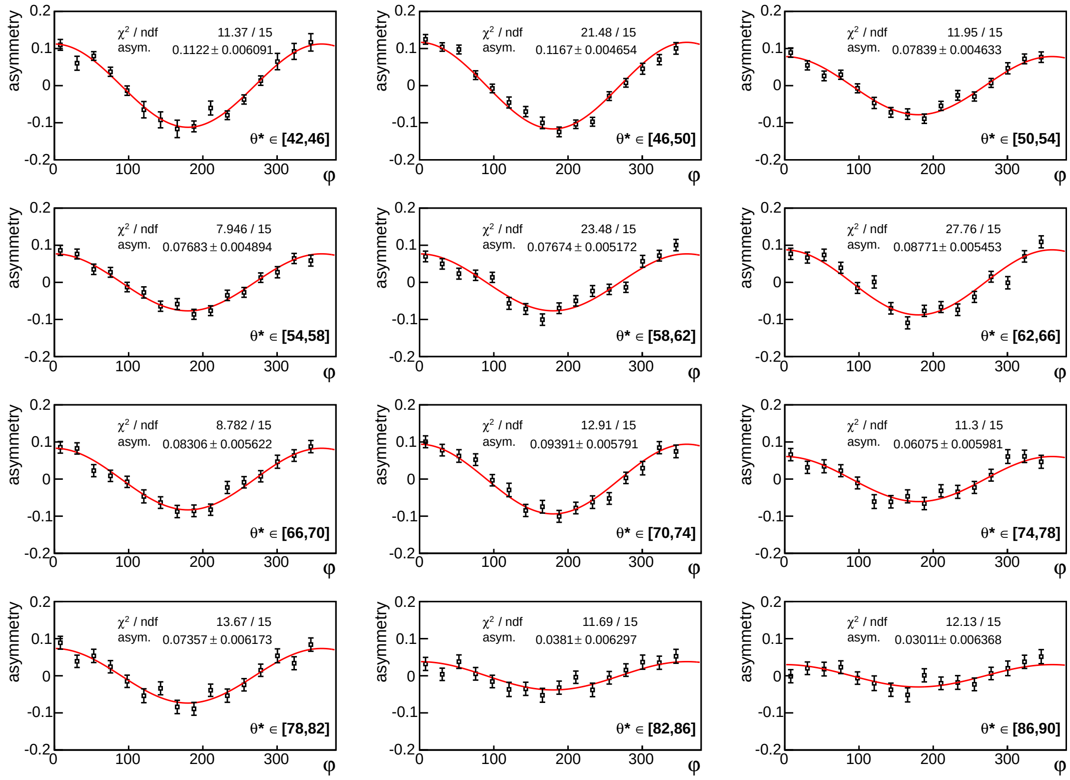

Figure 6.15 – Asymmetry calculated for 12 θ^* bins in the range 42° to 90°.

The asymmetry $\overline{a}_{\theta^*}$ resulting form the fit for each θ^* bin is shown in Fig. 6.16. The red line in the figure shows the analyzing power A_{θ^*} taken from the partial wave analysis [74] fitted in the absolute height to the experimental data obtained in this work by the function $PA_{\theta^*} = \overline{a}_{\theta^*}$, where the polarization P is a fit parameter.

The fit describe the experimental data points with $\chi^2/N_{dof} = 5.8$ and yield the value of the beam polarization of $(61.5 \pm 1.2)\%$. This result confirms the polarization obtained in Ref. [26] where the beam polarization was calculated to be $(61.0 \pm 1.7)\%$. The good agreement of results shows that the gain in track reconstruction accuracy by adding the SQT is not as critical for the polarization measurement as it is for the reconstruction of $pK^0\Sigma^+$ events.

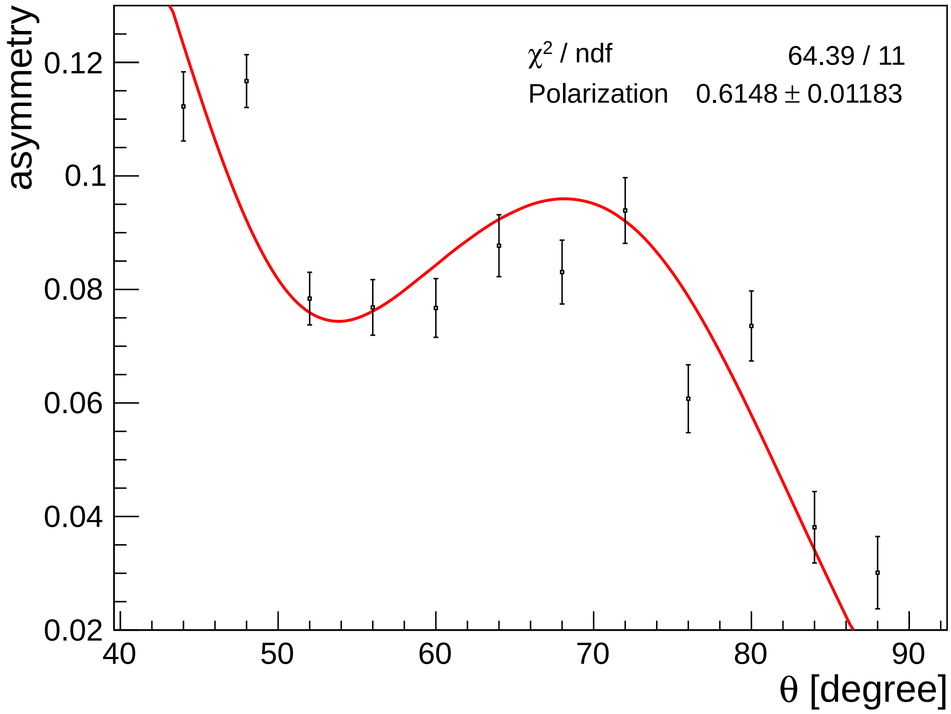

Figure 6.16 – The average asymmetries $\overline{a}_{\theta^*}$ for different θ^* bins, fitted in absolute height by the analyzing power A_{θ^*} taken from the partial wave analysis REF. The obtained fit parameter P is equivalent to the beam polarization.

6.2 $pK^0\Sigma^+$ Events

After the geometrical reconstruction of the $pK^0\Sigma^+$ events (see Sec. 5.4.2, 5.5.2) the kinematical variables need to be calculated. However, the fact, that the direction of the Σ^+ hyperon is only defined within the plane created by charged decay particle of the Σ^+ and by the primary vertex, complicate this task considerably. Therefore, two methods are proposed and used to determine the Σ^+ direction and all kinematic variables.

6.2.1 Parametrization of the Σ^+ direction

In this method the Σ^+ direction is parameterized by its decay length l (Fig. 6.17).

Using the parameterized Σ^+ direction and momentum conservation a system of three nonlinear equations with three unknown parameters is constructed (Eq. (6.7)).

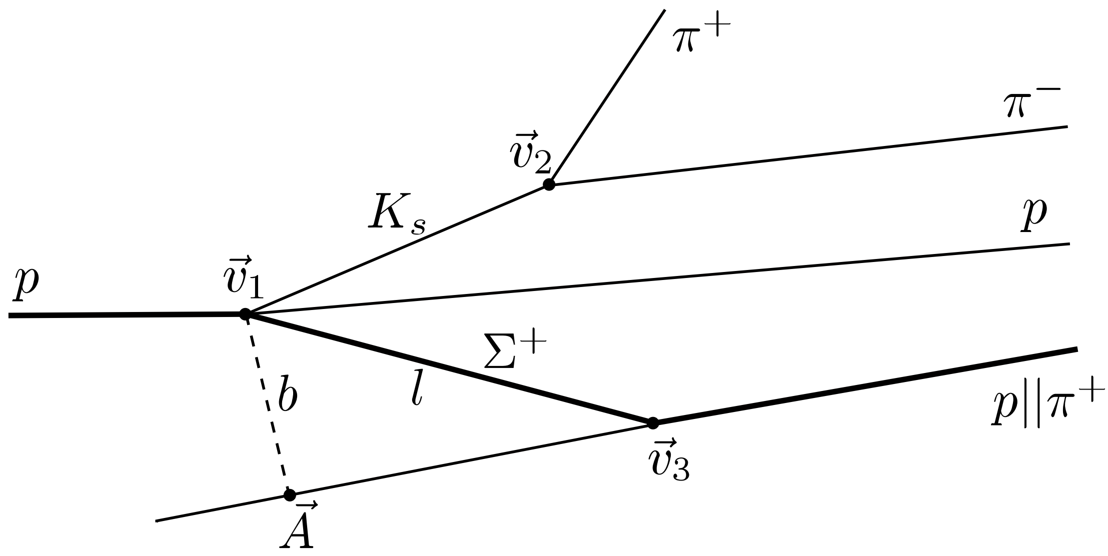

Figure 6.17 – Topology of the $pK^0\Sigma^+$ event

$$\begin{pmatrix} x_p \\ y_p \\ z_p \end{pmatrix} p_p + \begin{pmatrix} p_{K_x} \\ p_{K_y} \\ p_{K_z} \end{pmatrix} + \begin{pmatrix} \dfrac{A_x + x_{ch}\sqrt{l^2 - b^2} - v_{1_x}}{l} \\ \dfrac{A_y + y_{ch}\sqrt{l^2 - b^2} - v_{1_y}}{l} \\ \dfrac{A_z + z_{ch}\sqrt{l^2 - b^2} - v_{1_z}}{l} \end{pmatrix} p_{\Sigma^+} = \begin{pmatrix} 0 \\ 0 \\ p_b \end{pmatrix} \tag{6.7}$$

where x_p, y_p, z_p are the three components of the primary proton direction.

x_{ch}, y_{ch}, z_{ch} - the three components of the Σ^+ charge decay product direction.

$\vec{v}_1$ - position of the primary vertex.

$\vec{A}$, b - point and distance of closest approach between the Σ^+ charged decay particle and the primary vertex.

l - length of the Σ^+ path from production to decay.

$\vec{p}_K$ - K_s momentum vector which is determined by K_s decay pions using energy and momentum conservation (Add. 1).

p_p, p_{Σ^+} - absolute momenta of primary proton and Σ^+.

p_b - beam momentum.

The Eq. (6.7) give only one physically possible solution (Add. 3) for the p_p, p_{Σ^+} and l.

6.2.2 Using the SQT

In the case when the Σ^+ decays behind the SQT one can use the hit produced by the Σ^+ in the SQT to determine its momentum direction. To reduce the possibility of wrong hit assignment to Σ^+ track a following method is used.

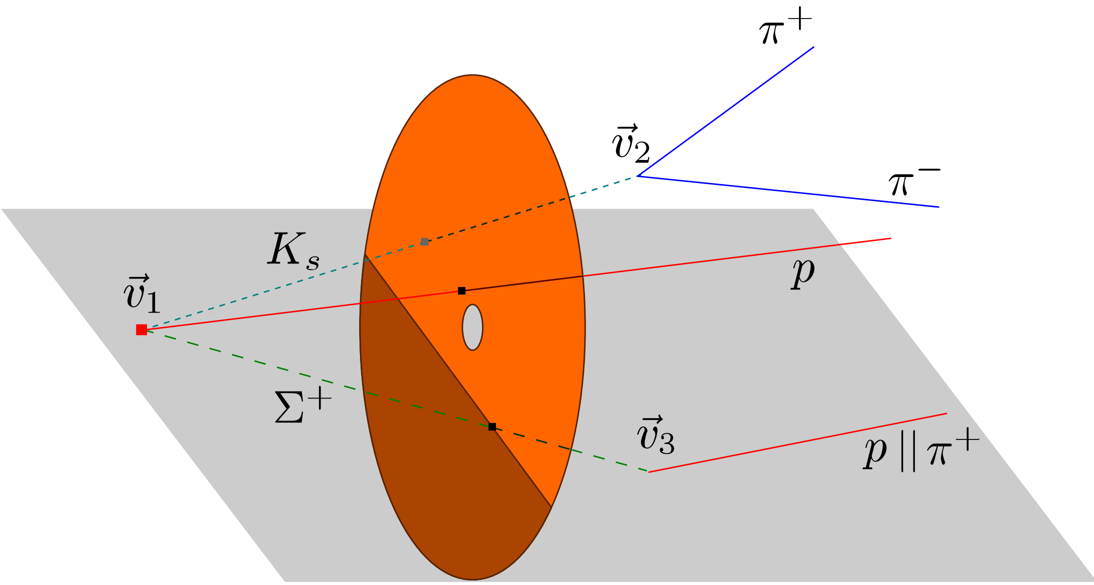

Figure 6.18 – Determination of the Σ^+ track direction for Σ^+ decay behind the SQT. The Σ^+ charged decay particle and the primary vertex define a plane which intersects the SQT in a line containing the Σ^+ hit.

The plane containing both the Σ^+ charge decay particle trajectory and the primary vertex (Fig. 6.18) also contains the Σ^+ track. This plane intersects the SQT in a line of possible location of the Σ^+ hit. If there is a hit which is less than 1 mm distance from this line and which does not belong to other tracks, then this hit is considered as the one lying on the Σ^+ track. The vector defined by the primary vertex and by the found SQT hit defines the momentum direction of the Σ^+ hyperon.

Using the reconstructed directions and momentum conservation a system of linear equation is constructed as given in Eq. (6.8). The solution of this equation yields the momenta of all involved particles.

$$\begin{pmatrix} x_p \\ y_p \\ z_p \end{pmatrix} p_p + \begin{pmatrix} x_{K_s} \\ y_{K_s} \\ z_{K_s} \end{pmatrix} p_{K_s} + \begin{pmatrix} x_{\Sigma^+} \\ y_{\Sigma^+} \\ z_{\Sigma^+} \end{pmatrix} p_{\Sigma^+} = \begin{pmatrix} 0 \\ 0 \\ p_b \end{pmatrix} \tag{6.8}$$

where x_{K_s}, y_{K_s}, z_{K_s} and x_{Σ^+}, y_{Σ^+}, z_{Σ^+} are the three components of the K_s and Σ^+ flight direction.

Fig. 6.19 illustrate the number of events reconstructed with the parametrization of the Σ^+ direction (red) and by using the SQT hit (blue) represented as circles with different area. The number of events reconstructed by "the SQT hit" method is smaller than that obtained by the parametrization method for the following reasons:

- it considers only Σ^+ hyperons which decay behind (after passing) the SQT which causes about 40% loss in number of events;
- any inefficiency in the SQT will causes the event reconstruction to fail.

The last reason is particular relevant in the present experiment since one out of 16 readout blocks of the SQT was disconnected by vibration during the mounting procedure.

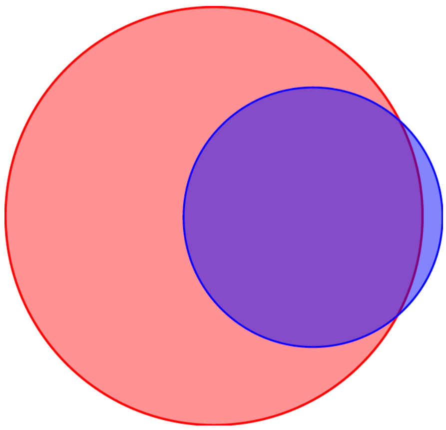

Figure 6.19 – Area of circles indicating number of events reconstructed with the parametrization of the Σ^+ direction (red) and by using the SQT hit (blue).

The overlap of both circles in Fig. 6.19 represents events which are reconstructed by both methods. The fact that there is almost 100% overlap gives confidence that the obtained result is stable.

Tab. 6.2 summarizes the numbers of reconstructed events by both methods.

Due to the asymmetric inefficiency in the SQT events uniquely reconstructed by the SQT hit method (18 events) are not used for the determination of polarization observables.

Σ^+ parametrization method	The SQT hit method	Sum	Overlap
887	316	905	298

Table 6.2 – Numbers of reconstructed events by the two different methods and the relation between them. The numbers are obtained after applying final selection criteria which will be discussed in the following sections.

6.2.3 Vertex distributions

The material downstream of the target causes multiple scattering as well as production of secondary particles.

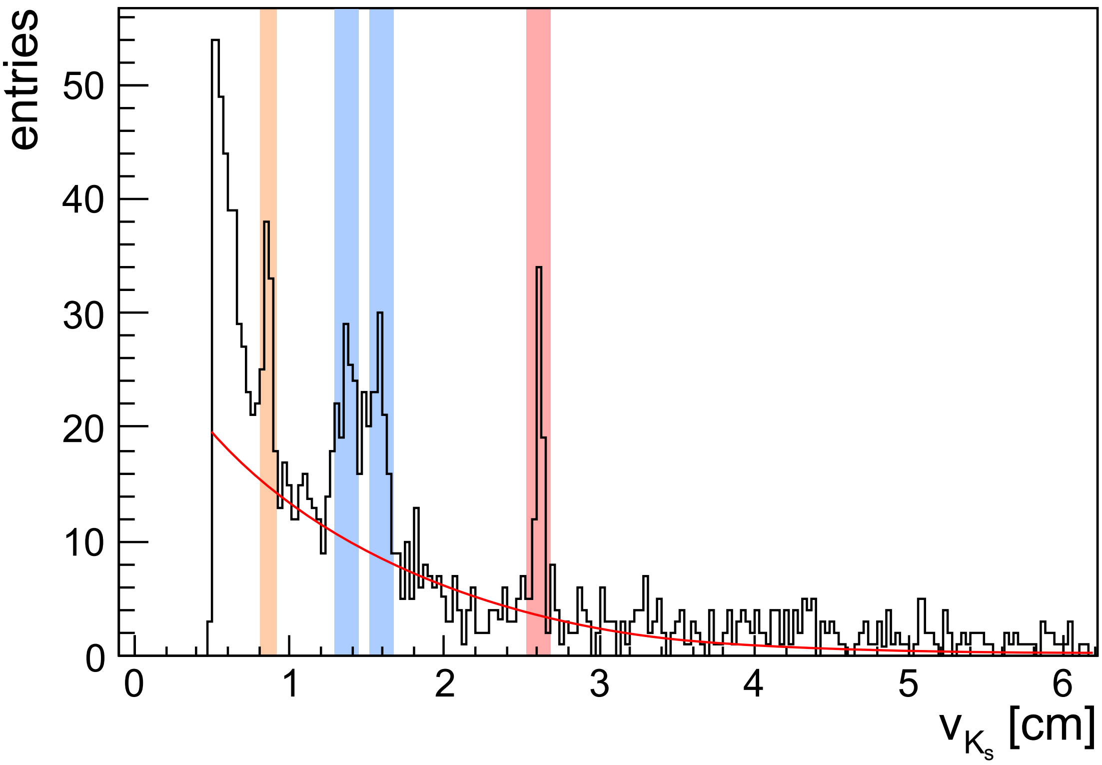

Figure 6.20 – Distribution of the z component of the K_s decay vertex. The orange, the blue and the red shaded areas indicate the location of the vacuum separation foil, the start counter and the SQT, respectively.

By chance it may happens that a background event in combination with a produced secondary particle can forms an event which satisfies geometry and kinematic conditions of the $pK^0\Sigma^+$ event. Such events can be identified by analyzing the distribution of the z component of the K_s decay vertex (Fig. 6.20). The distribution shown in Fig. 6.20

includes the condition on χ^2 of the kinematic fit accepting $\chi^2_{kin} < 5$, and after selecting events having a z component of the K_s decay vertex longer than 5 mm. The same conditions on the K_s decay vertex is also applied during event finding, Sec. 5.4.2. Due to the excellent tracking precision regions having a large contribution of false K_s vertices are directly visible in Fig. 6.20.

The first peak shaded with orange color is a result of the beam interaction with the vacuum separation foil. The vacuum separation foil contributes only material inside COSY-TOF which has to be passed by the direct beam. To confirm this interpretation, projection of the K_s decay vertex distribution on the xy plane are plotted in Fig. 6.21 for 1 mm thick slices in z in front and behind the peak at $z \simeq 8.5$ mm. The concentration of vertices around $x = 0$, $y = 0$ in peak region and the much wider vertex distribution in front of and behind the peak demonstrate that the peak is due to a point-like interaction, only explainable as interaction of the beam with the vacuum separation foil.

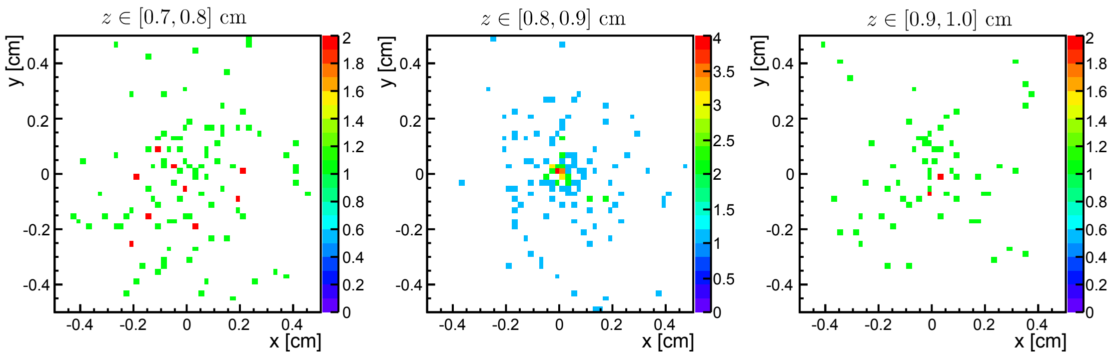

Figure 6.21 – Kaon vertex distribution in the foil region.

The blue shaded peaks are due to the two scintillator layers of the start counter. The red shaded peak at $z \simeq 2.6$ cm coincides with the z coordinate of the SQT position.

To suppress background events which are created due to produced secondary particles a stronger selection on the χ^2 of kinematic fit of $\chi^2_{kin} < 2$ is applied in the peak regions. In the vacuum-separation foil region with $z \in [0.8, 0.9]$ cm events with $\sqrt{x^2 + y^2} < 0.1$ cm are rejected to suppress interactions of the direct beam with the foil.

In addition the selection $z_K > 0.8$ cm is used to exclude K_s decay vertices too close to the target. Vertices in this region due to multiple scattering and due to finite reconstruction resolution have a large contribution of prompt events within the target volume, which are produced at a rate which is by order of magnitude larger than of the $pK^0\Sigma^+$ final state.

The correct reconstruction of $pK^0\Sigma^+$ events can be controlled analyzing the decay vertex $|v| = \sqrt{v_x^2 + v_y^2 + v_z^2}$ distribution of K_s and Σ^+ particles corrected on event by event basis by $\beta\gamma$. The obtained spectrum represents the eigentime distribution of K_s and Σ^+, respectively. Fig. 6.22 and Fig. 6.23 show these distributions for K_s and Σ^+, respectively.

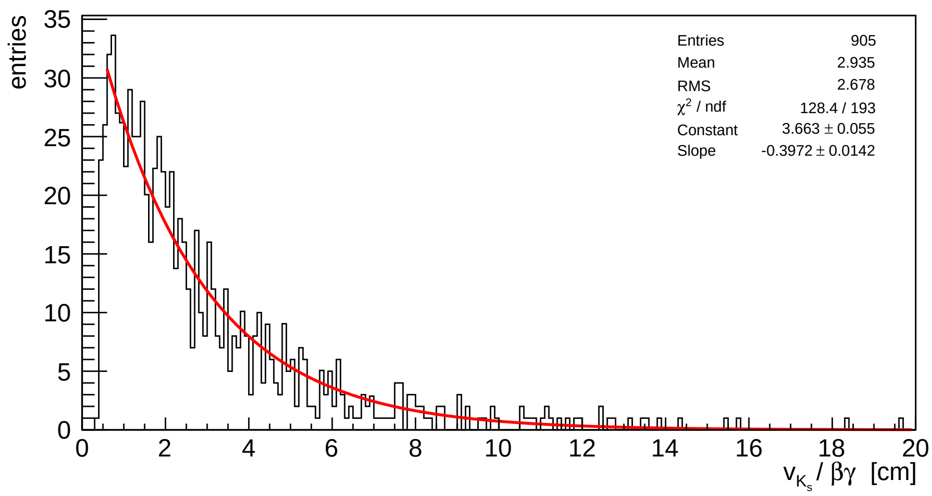

Figure 6.22 – Eigentime distribution of K_s. The value of the abscissa is obtained by dividing the distance of the K_s decay vertex from the origin $|v| = \sqrt{v_x^2 + v_y^2 + v_z^2}$ by the value of $\beta\gamma$ of the K_s in the corresponding $pK^0\Sigma^+$ event.

The exponential fit gives a value of 2.52 ± 0.09 cm for the K_s decay length and 2.46 ± 0.11 cm for the Σ^+ decay length. The value obtained for the Σ^+ is within the error in good agreement with the table value $c\tau_{\Sigma^+} = 2.40$ cm the value obtained for the K_s has a deviation of 1.8σ from the table value $c\tau_{\Sigma^+} = 2.68$ cm.

6.2.4 pK^0 missing mass

The pK^0 missing mass is calculated as $m_{miss} = \sqrt{E_{miss}^2 - \vec{p}_{miss}^{\,2}}$, where E_{miss} and $\vec{p}_{miss}$ are defined by the missing four-vector $P_{miss} = (P_{beam} + P_{target}) - (P_p + P_{K_s})$. The pK^0 missing mass is evaluated for events before the kinematical fit which constrains it to

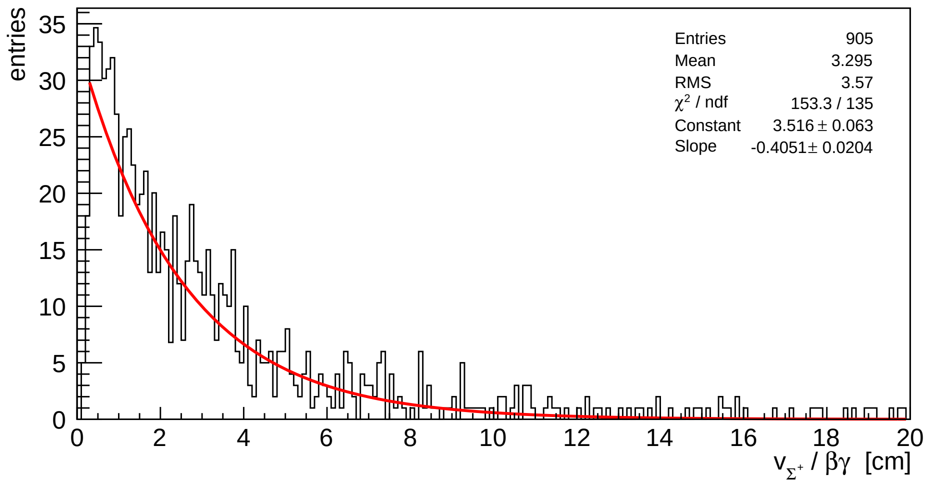

Figure 6.23 – Eigentime distribution of Σ^+. The value of the abscissa is obtained by dividing the distance of the Σ^+ decay vertex from the origin $|v| = \sqrt{v_x^2 + v_y^2 + v_z^2}$ by the value of $\beta\gamma$ of the Σ^+ in the corresponding $pK^0\Sigma^+$ event.

the Σ^+ mass. Fig. 6.24 shows the pK^0 missing mass distribution after the geometrical fit for different selection criteria.

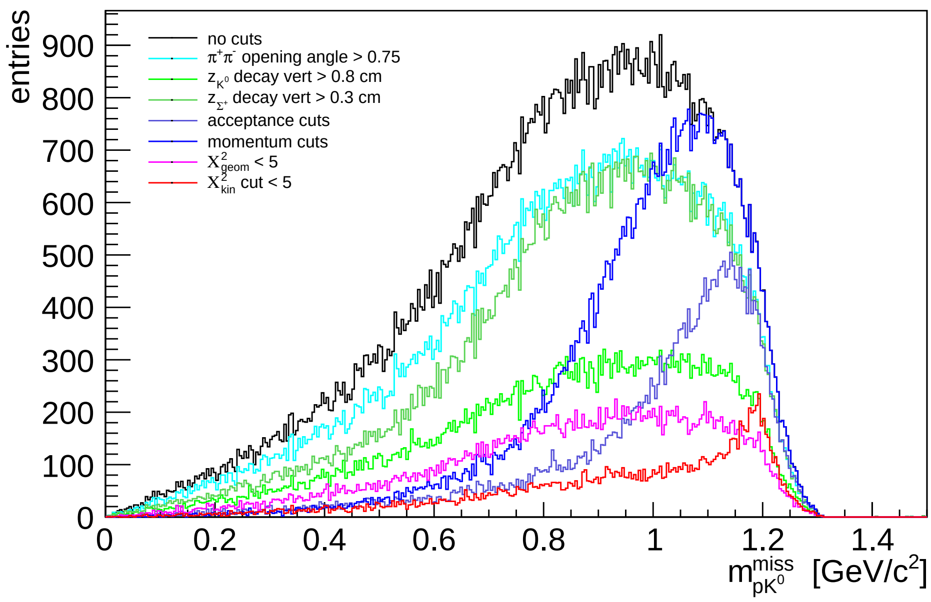

Figure 6.24 – pK^0 missing mass distribution obtained after the geometrical fit for different selection criteria. All selection criteria are explained in the text.

In the Fig. 6.24 the black histogram shows to the distribution without any conditions. The reduction of the yield seed in the aqua distribution is due to limit on the opening angle between the two pions from the K_s decay. The dark and light green histograms correspond to events with a lower limit on the z component of kaon and Σ^+ decay vertex position, respectively. The value of $z_{\Sigma^+} > 0.3$ cm is chosen in order to suppress fake Σ^+ candidates that are too close to the target vertex location.

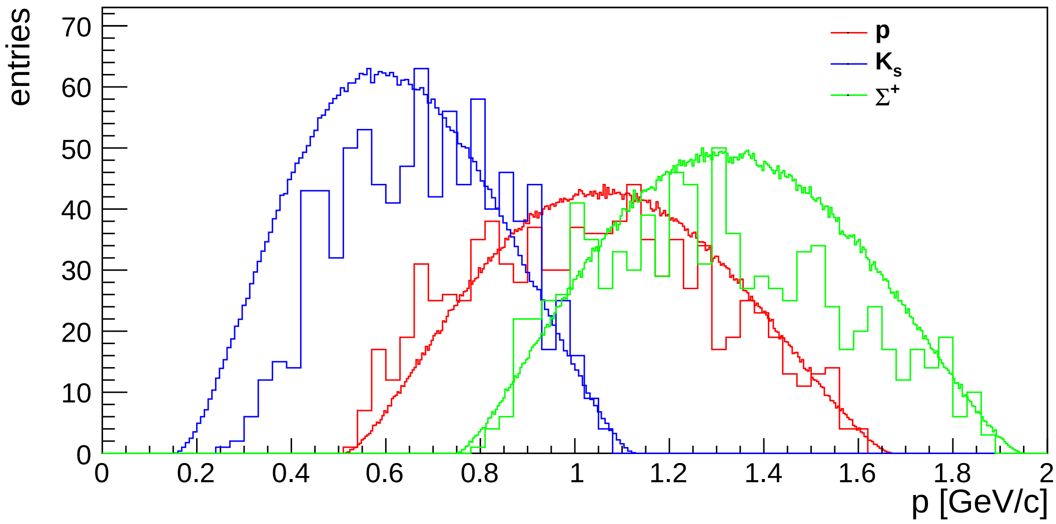

Figure 6.25 – Momentum distributions of protons (red), K_s (blue) and Σ^+ (green) in the $pK^0\Sigma^+$ final state. The histogram with the fine binning correspond to the generated MC distributions, the histograms with the coarse binning to the $pK^0\Sigma^+$ events selected from the experimental data.

The dark and medium blue distributions denote selections based on the kinematically allowed range in polar angle and momentum, respectively, for each of the tree particle in the $pK^0\Sigma^+$ final state. The distribution with the fine binning in Fig. 6.25 shows the true MC momentum distributions for all particles of the $pK^0\Sigma^+$ final state. Based on these distributions the upper and lower limit of the accepted momentum of each particle is set. To illustrate the influence of a selection based on the χ^2 of the geometrical fit, thepK_s missing mass distribution is also plotted in Fig. 6.24 for $\chi^2_{geom} < 5$ (magenta). For the final selection of $pK^0\Sigma^+$ events the last condition is not used instead a condition on the χ^2 of the kinematical fit is required , the effect of which is seen in the red histogram. In addition a lower limit of 0.15 rad is used for angle

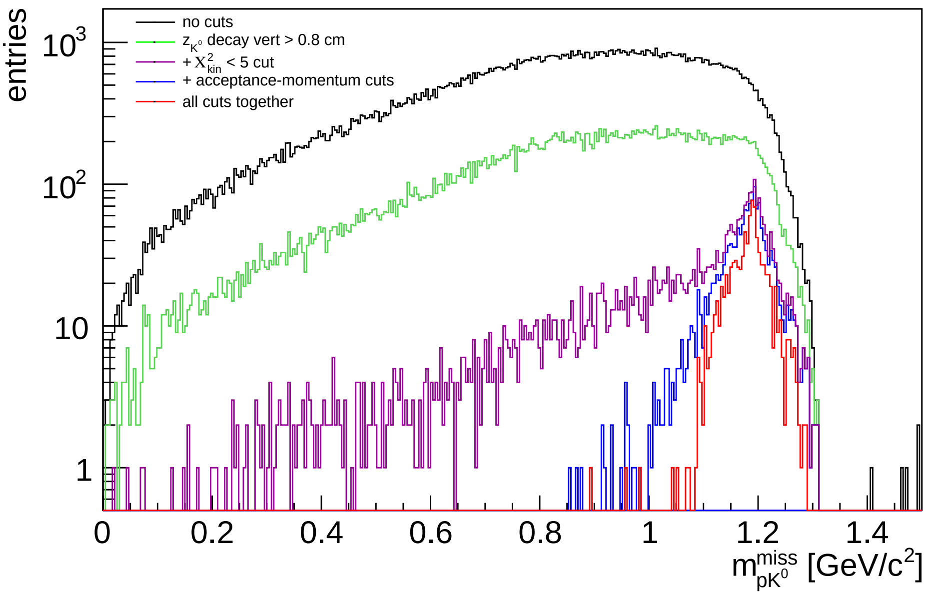

Figure 6.26 – pK^0 missing mass distribution obtained after the geometrical fit. The influence of the different selections is shown additively.

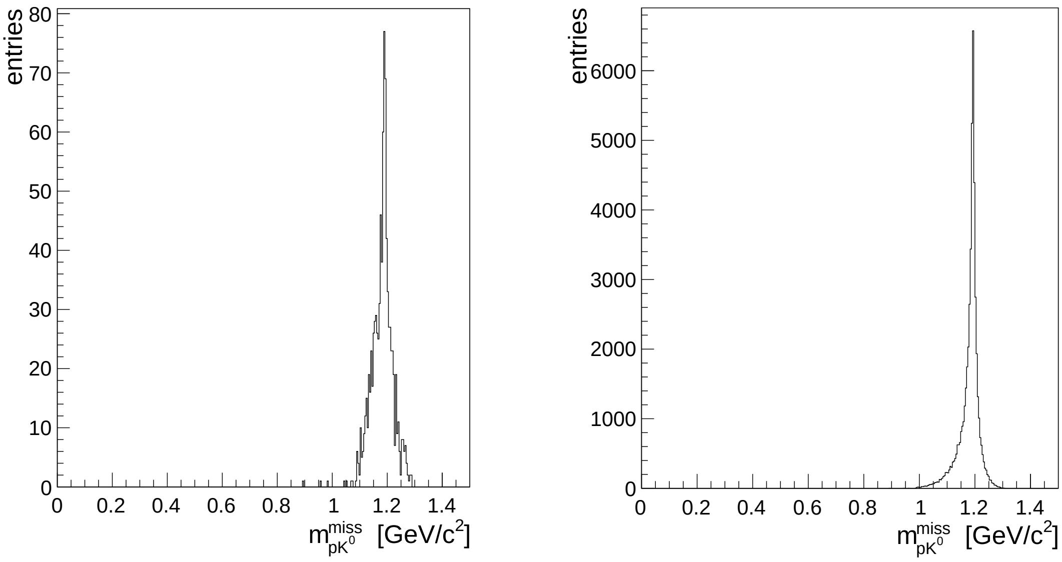

Figure 6.27 – Left: pK_s missing mass of the selected $pK^0\Sigma^+$ events. The FWHM value of the distribution is 26 MeV. Right: pK_s missing mass as a result of reconstruction of 10^6 MC events.

between the K_s and each of the two pions from K_s decay. This limit will be discussed in Sec. 6.2.7 in more detail. Fig. 6.26 shows the influence of the selections mentioned above in a sequential way.

The pK_s missing mass distribution resulting from the selection based on the conditions mentioned above and on the conditions on the decay vertices discussed in Sec. 6.2.3 is shown in Fig. 6.27 (left). The distribution has a FWHM value of 26 MeV, which corresponds to a standard deviation σ of 11 MeV. Fig. 6.27 (right) shows the distribution for 10^6 simulated and reconstructed MC events. Both distributions are in fair agreement.

6.2.5 Angular distributions, acceptance and reconstruction efficiency

The angular distributions of p, K^0 and Σ^+ illustrated by thick red, blue and green histograms in Fig. 6.28 are within the STT acceptance. Pions from K_s and Σ^+ decay, shown by the thin histograms, however, are also emitted at the angles outside the STT acceptance. This results in an efficiency loss for the reconstruction of $pK^0\Sigma^+$ events.

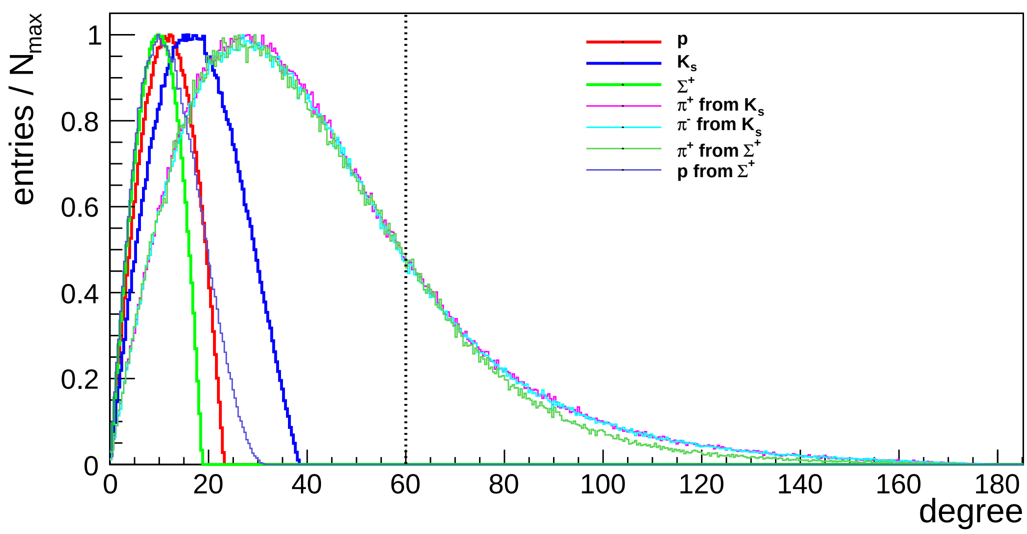

Figure 6.28 – Angular distributions in laboratory system of all final state particles. The vertical-dotted line indicates the approximate acceptance of the STT.

The angular distributions of the primary particles p. K^0 and Σ^+ in the CMS are shown in Fig. 6.29. This distributions are already corrected for acceptance and

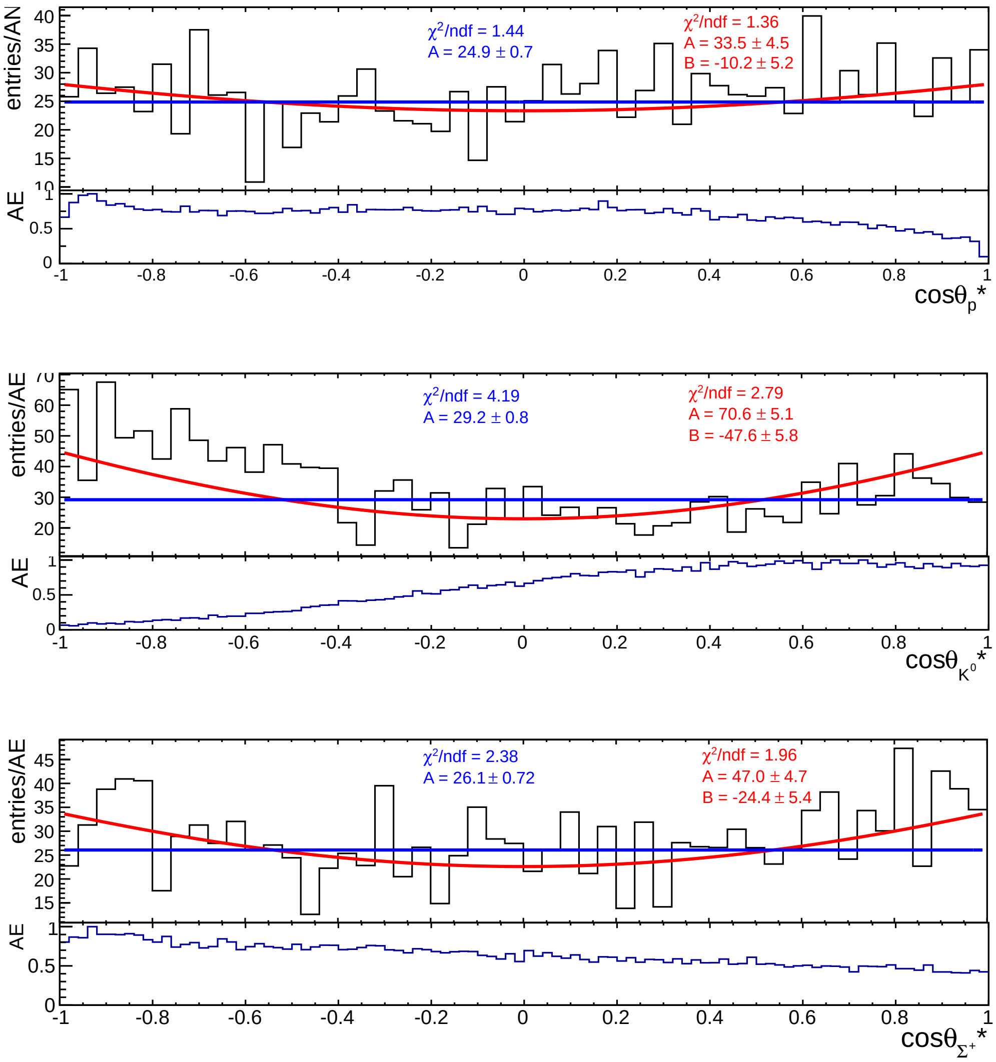

Figure 6.29 – Angular distributions of p, K_s and Σ^+ in the CMS corrected by acceptance and reconstruction efficiency (AE) both of which were deduced by reconstructing 10^6 $pK_s\Sigma^+$ Monte Carlo events. Each distribution is fitted by the functions $f = A$ (blue) and $f = A + B\cos(\cos\theta^\star)$ (red), where A and B are constants. The corresponding χ^2/N_{dof} and parameters are shown in the figures. See also Tab. III, IV and V in Add. 4.

efficiency. The influence of the acceptance and reconstruction efficiency (AE) on each particle, obtained as a result of reconstruction of 10^6 $pp \to pK_s\Sigma^+$ MC events, can be seen on the lower part of the figure panels. As the pions from K_s decay are most strongly affected by the STT acceptance limit, also the K_s which is reconstructed based on decay pions is most sensitive to the limited acceptance. The smaller the K_s momentum the larger is probability for the decay pions to be emitted into the backward region outside the STT acceptance. Exactly this behavior is seen in the K_s angular distribution: the reconstruction efficiency significantly decreases towards the backward region. The inefficiency in K_s reconstruction at backward angles is reflected in an inefficiency of the proton and Σ^+ reconstruction in the forward region as expected from momentum conservation.

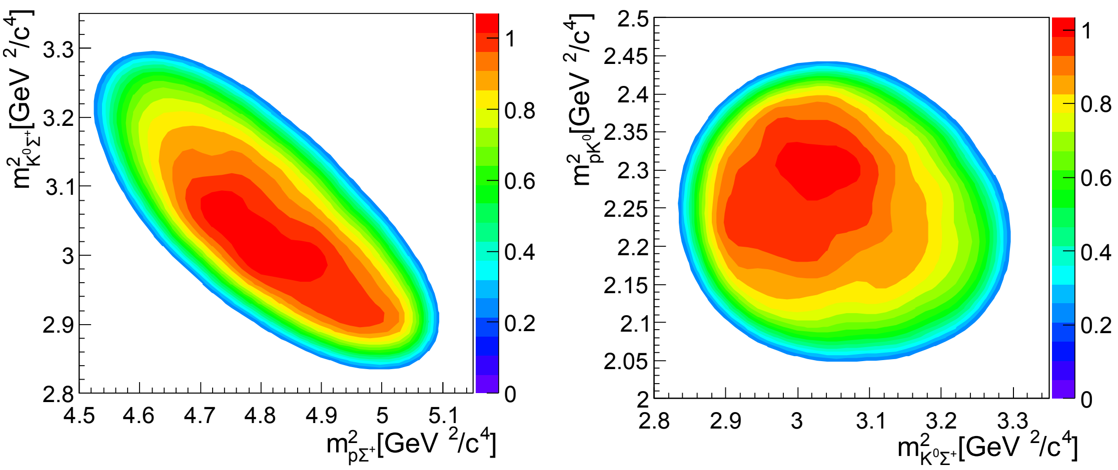

Figure 6.30 – Combined acceptance and reconstruction efficiency deduced from the analysis of 10^6 $pp \to pK_s\Sigma^+$ events of a Monte Carlo simulation.

Fig. 6.30 shows the acceptance and reconstruction efficiency (AE) map in a Dalitz plot representation. An inefficiency at high $K^0\Sigma^+$ masses and at low pK^0 masses region is observed. The constant drop of of the value of AE at the edges of the Dalitz plot is a visualization effect of the finite binning and is not relevant.

6.2.6 Σ^+ decay channel separation and kinematics.

The asymmetry parameter of the $\Sigma^+ \to p\pi^0$ decay channel is about 14 times bigger than that for the $\Sigma^+ \to n\pi^+$ decay channel. Therefore, at limited event statistics, the first decay channel is more significant for the determination of the Σ^+ polarization.

Due to the fact that only charged particle tracks are measured, the direct determination of the decay channel based on kinematic observables is not possible. However, the decay channel can be identified by comparing the angular distributions of the Σ^+ charged decay particle relative to the Σ^+ direction, visible as kink angle between both tracks. The red and blue distributions in Fig. 6.31 show the generated MC angular distributions for the $\Sigma^+ \to p\pi^0$ and $\Sigma^+ \to n\pi^+$ decay channels, respectively.

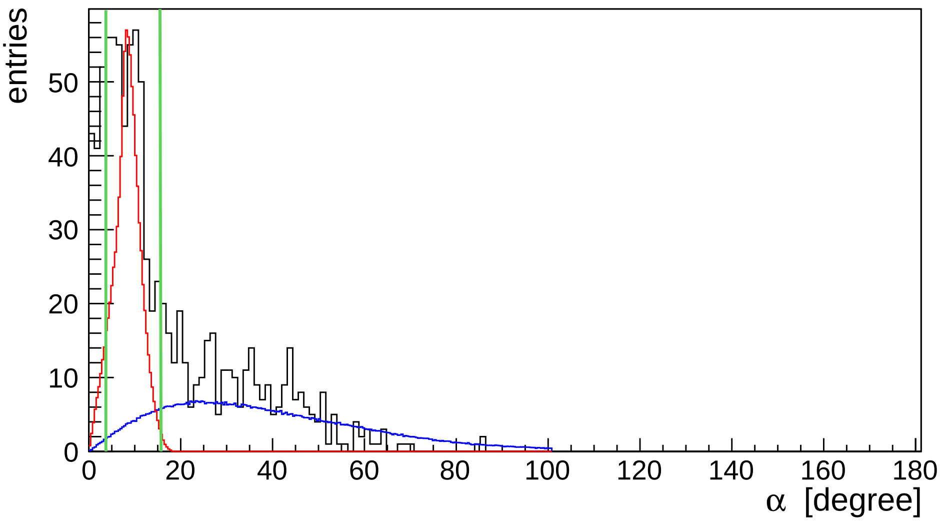

Figure 6.31 – Distribution of angles between the direction of the Σ^+ and its charged decay particle. The vertical green lines show limits applied for the selection of the $\Sigma^+ \to p\pi^0$ decay channel.

The black histogram in Fig. 6.31 which corresponds to the selected data sample show a good agreement with generated MC data sample except for small angles, where the yield of found $pK^0\Sigma^+$ events is higher than expected. This enhancement may be due to poorly determined Σ^+ direction in cases where the charged decay particle of the Σ^+ is emitted at small angles relative to the beam direction. In such cases the plane containing the Σ^+ track is not well defined. The same behavior is observed for reconstructed MC.

Events having a kink angle between 4.5° and 16.5° are accepted as $\Sigma^+ \to p\pi^0$ decay. This identified event sample still contains about 10% of $\Sigma^+ \to n\pi^+$ decays which, however, due to the small asymmetry parameter do not significantly influence the polarization observables.

For the calculation of the Σ^+ polarization the knowledge of the proton momentum of the hyperon decay in the Σ^+ rest frame is needed. Due to the kinematics of the decay the restricted knowledge of only Σ^+ momentum and kink angle θ, it is not possible to obtain a unique solution for the proton momentum. There are generally two solutions, labeled as p_θ^+ and p_θ^- in Fig. 6.32, which are kinematically not distinguishable without knowledge of the pion direction.

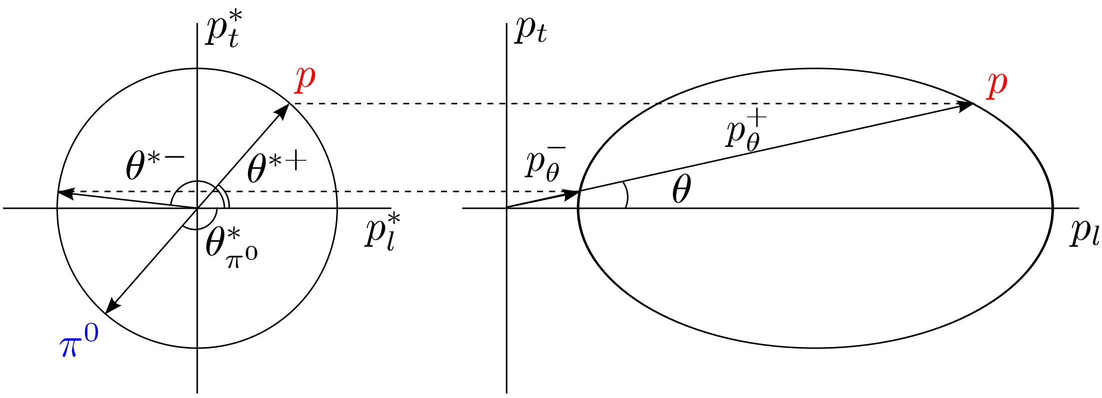

Figure 6.32 – The kinematics of the $\Sigma^+ \to p\pi^0$ decay in the Σ^+ rest frame (left) and proton ellipse in the laboratory frame (right). The proton direction, defined by the kink angle θ in laboratory system, allows two solutions p^{*+} and p^{*-} in the Σ^+ rest frame.

Eq. (6.9) shows the analytical solution for the momenta of the Σ^+ charged decay particle.

$$\begin{aligned} p_{ch} = \frac{1}{2}\, \frac{1}{\left(m_{\Sigma^+}{}^2 + p_{\Sigma^+}{}^2 - p_{\Sigma^+}{}^2 \cos^2(\theta_{ch})\right) p_{\Sigma^+} \cos(\theta_{ch})} \cdot \Big(p_{\Sigma^+}{}^2 \cos^2(\theta_{ch}) \cdot \\ \left(m_{ch}^2 - m_0{}^2 + m_{\Sigma^+}{}^2\right) \pm \left(m_\Sigma{}^2 + p_{\Sigma^+}{}^2\right)^{\frac{1}{2}} \Big(\Big(4\, m_{ch}{}^2 p_{\Sigma^+}{}^2 \cos^2(\theta_{ch}) + \\ m_{ch}{}^4 + \left(-4\, p_{\Sigma^+}{}^2 - 2\, m_0{}^2 - 2\, m_{\Sigma^+}{}^2\right) m_{ch}{}^2 + \\ (m_{\Sigma^+} - m_0)^2 (m_{\Sigma^+} + m_0)^2\Big) p_{\Sigma^+}{}^2 \cos^2(\theta_{ch})\Big)^{\frac{1}{2}}\Big) \end{aligned} \tag{6.9}$$

where p_{Σ^+} is the Σ^+ momentum, which is known from the analysis of the $pp \to pK^0\Sigma^+$ event kinematics.

θ_{ch} and m_{ch} are kink angle and mass of the charged particle from Σ^+ decay (p or π^+), respectively.

m_0 is the mass of the neutral particle from Σ^+ decay (π^0 or n).

To select the correct solution the time of flight information is used. Since in most of the cases the two solutions of Eq. (6.9) are well separated, the resolution of the time-of-flight measurement is sufficient to select the correct solution. From MC studies it is concluded that for about 96% of the $pK^0\Sigma^+$, $\Sigma^+ \to p\pi^0$ events the momentum of the proton is obtained correctly.

6.2.7 Background studies

There are two categories of background events which may create a signature of $pp \to pK_s\Sigma^+$ reaction. These are events with and without delayed decay vertices. The first column of Tab. 6.3 shows possible background channels.

Channel	Cross section σ [μb]	Reconstructed as $pK_s\Sigma^+$ from 200,000 events	Estimated contribution to the signal
$pp\pi^+\pi^-$	2510	0	0
$pn\pi^+\pi^+\pi^-$	450	-	0
$pp\pi^+\pi^-\pi^0$	220	-	0
$pp\eta$	150	-	0
$pp\pi^+\pi^-\pi^0\pi^0$	50	-	0
$pp\rho$	20	-	0
$pp\omega$	20	-	0
$pK^+\Lambda$	20	21	21
$nK^+\Sigma^+$	20	-	0
$pK^+\Sigma^0$	5	-	5
$pK^0\Lambda\pi^+$	2	-	2
$pK^+\Lambda\pi^0$	10	-	11
$nK^+\Lambda\pi^+$	2	-	2

Table 6.3 – Possible background channels without (upper part) and with (lower part) delayed decay vertex. Cross section are taken mainly from Ref. [75], at 2.95 GeV/c beam momenta (roughly interpolated or extrapolated to 2.95 GeV/c).

Due to the excellent vertex resolution of the COSY-TOF detector (Sec. 6.1.3) the background events without delayed vertices are efficiently suppressed by the lower limit on the z-coordinate of the K_s decay vertex. This is confirmed by simulation and reconstruction of 200,000 $pp \to pp\pi^+\pi^-$ events. None of them survives the $pK^0\Sigma^+$

selection criteria. Based on this result the contribution of all other channels with only prompt charge particles from the target is estimated to be negligibly small.

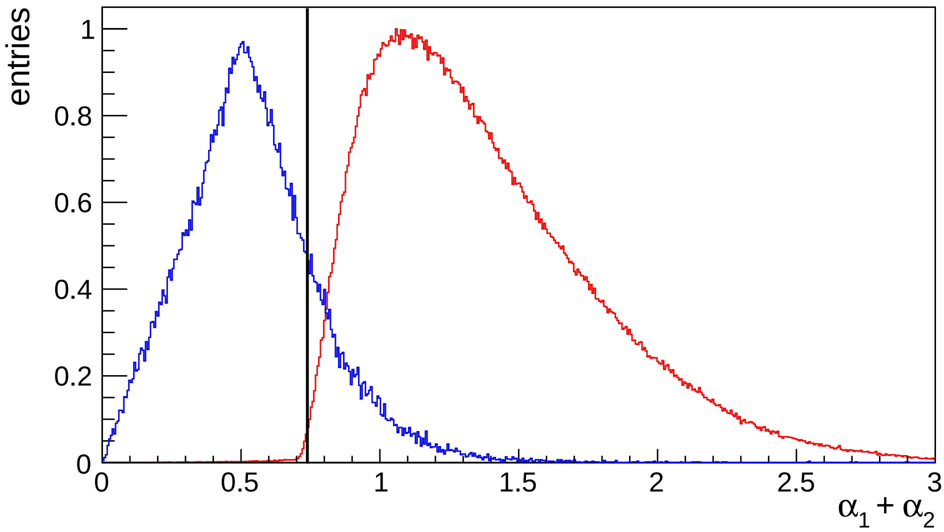

Figure 6.33 – Distribution of the opening angle between the decay particles of Λ (blue) and K_s (red). The vertical line at 0.75 rad shows the lower limit applied to select $pK^0\Sigma^+$ events.

To estimate the background contribution due to channels of the second category the 200,000 $pp \to pK^+\Lambda$ events are simulated and reconstructed. To distinguish $K_s \to \pi^+\pi^-$ and $\Lambda \to p\pi^-$ during the reconstruction a lower limit on the opening angle between the two decay particles is used (see Fig. 6.33). Another sensitive parameter is the angle between the momentum direction of the mother particle and of its decay particles. In the case of K_s, these angles are equivalent while in the case of Λ the angles are very different from each other (Fig. 6.34). The lower limit of 0.15 rad efficiently suppresses the $\Lambda \to p\pi^-$ channel. Only 21 events successfully pass all selection criteria, amounting 0.01% reconstruction efficiency. From the dedicated analysis of this channel with the same experimental data sample [26] about 40,000 $pK^+\Lambda$ events have been reconstructed with a reconstruction efficiency of 20%. Using this information the background contribution of the reaction $pp \to pK^+\Lambda$ is estimated to be 21 events.

The contribution $nK^+\Sigma^+$ events can be discarded already at event-finding stage since they have less then 4 charged tracks in the final state. The contribution of

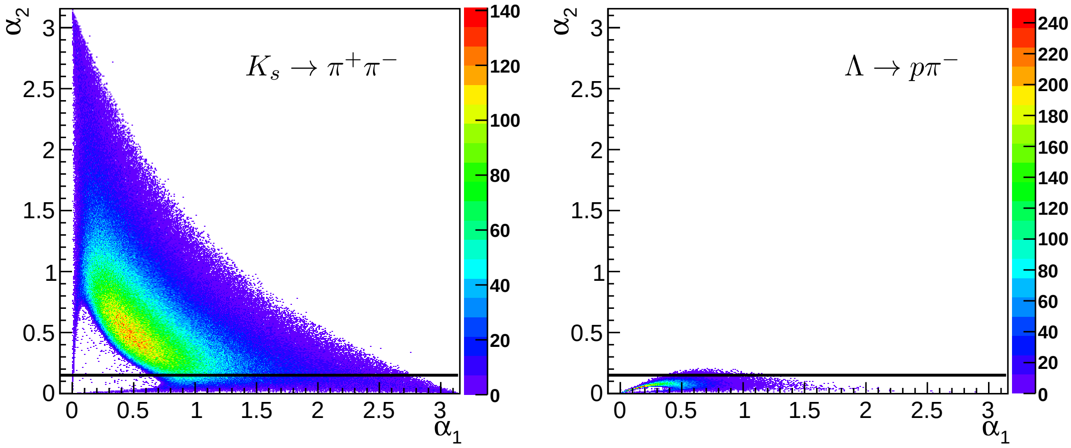

Figure 6.34 – Correlation of the angles between the momentum direction of the mother particle and its decay particles. The black line indicates the lower limit used to distinguish $K_s \to \pi^+\pi^-$ from $\Lambda \to p\pi^-$.

$pK^+\Lambda\pi^0$ is estimated based on the analysis $pK^+\Lambda$ channel, taking into account the ratio of cross-sections.

The total contribution of physical background N_{bg} is estimated to be at most 50 events. With this, the signal to background ratio is $S/N = (N_{reco} - N_{bg})/N_{bg} = (905 - 50)/50 = 17.1$, corresponding to 5.85% background contribution.

Chapter 7

Results

In this chapter the results of this work are presented and described. The discussion of the results will follow in Ch. 8.

7.1 Unpolarized Observables

To determine the unpolarized observables the $pK^0\Sigma^+$ event sample is reconstructed both by using the "Σ^+ direction parametrization" (Sec. 6.2.1) method, and by the "SQT hit" method (Sec. 6.2.2).

7.1.1 Cross section of the reaction $pp \to pK^0\Sigma^+$

The cross section is defined as follows:

$$\sigma = 2 \cdot \frac{N_{signal}}{\varepsilon_{reco} \cdot \varepsilon_{sc}^{hyp} \cdot L} \tag{7.1}$$

where N_{signal} is the number of $pK_s\Sigma^+$ events in the reconstructed event sample fulfilling the selection criteria. This number determined by subtracting the estimated physical background from the total number of reconstructed and selected events: $N_{signal} = N_{reco} - N_{bg} = 905 - 50 = 855 \pm 31_{stat} \pm 20_{syst}$;

the factor of two accounts for the fact that K^0 is 50% K_s and 50% K_L;

ε_{reco} - reconstruction efficiency for the reaction $pp \to pK_s\Sigma^+$, determined by using MC simulation ($\varepsilon_{reco} = 0.0537 \pm 0.0014$);

ε_{sc}^{hyp} - efficiency of the start counter for the $pp \to pK_s\Sigma^+$ reaction;

L - luminosity during the experiment.

The time integrated luminosity is determined from the analysis of pp elastic scattering events [76]: $L = 14.6 \pm 0.7\ nb^{-1}$. To find the efficiency of the start counter ε_{sc} for single tracks the number of tracks obtained with the hyperon trigger as a function of the azimuthal angle θ is plotted in Fig. 7.1. A limit of $\theta < 30°$ is applied to account the acceptance of the $pK_s\Sigma^+$ final state (see. Fig. 6.28). The red line marks the maximum efficiency around 100° and 150°. Assuming 100% efficiency in these regions the, start counter efficiency is obtained from the ratio of the total number of reconstructed tracks to the integral of the number of tracks over the full φ range with constant maximum detection efficiency defined by the red line: $\varepsilon_{sc} = 0.86 \pm 0.02$.

For the reaction $pp \to pK_s\Sigma^+$, except for cases with K_s decay vertex in front of the start counter, two tracks in the start counted are expected, $\varepsilon_{sc}^{hyp} = \varepsilon_{sc}^2 = 0.74 \pm 0.028$.

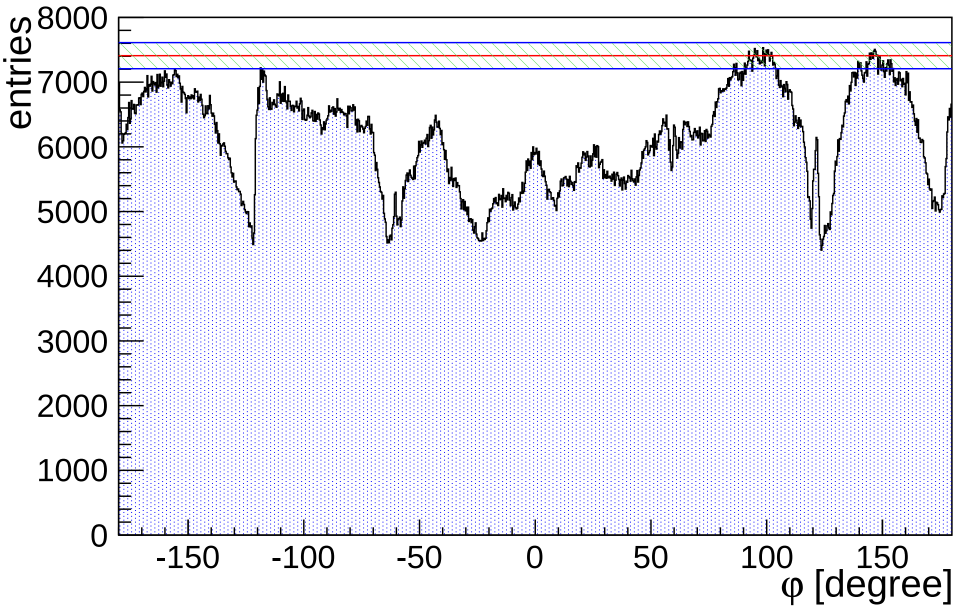

Figure 7.1 – Distribution of the number of tracks collected with the hyperon trigger as a function of azimuthal angle. A condition on polar angle $\theta < 30°$ was applied. The red line indicates the maximum detection efficiency.

Evaluation of Eq. (7.1) with the parameters specified above gives the following cross section of the reaction $pp \to pK^0\Sigma^+$:

$$\sigma = (2.95 \pm 0.11_{stat} \pm 0.22_{syst})\ \mu b \tag{7.2}$$

The systematic error is composed of the error of the luminosity determination, the uncertainty of the efficiencies of the start counter and $pK^0\Sigma^+$ reconstruction, and finally from the systematic error introduced by estimating the background contribution in the selected $pK^0\Sigma^+$ event sample:

$$\Delta\sigma_{syst} = \sqrt{\left(\frac{\partial\sigma}{\partial L}\Delta L\right)^2 + \left(\frac{\partial\sigma}{\partial\varepsilon_{sc}}\Delta\varepsilon_{sc}\right)^2 + \left(\frac{\partial\sigma}{\partial\varepsilon_{reco}}\Delta\varepsilon_{reco}\right)^2 + \left(\frac{\partial\sigma}{\partial N}\Delta N_{syst}\right)^2} \quad (7.3)$$

7.1.2 Dalitz plot

For the construction of the Dalitz plot the selected $pK^0\Sigma^+$ event sample after the kinematical fit is used. The obtained distribution is corrected for acceptance and reconstruction efficiency using the AE map from Fig. 6.30. The result is shown in Fig. 7.2. The black line shows the kinematic limit of the distributions. A clear enhancement

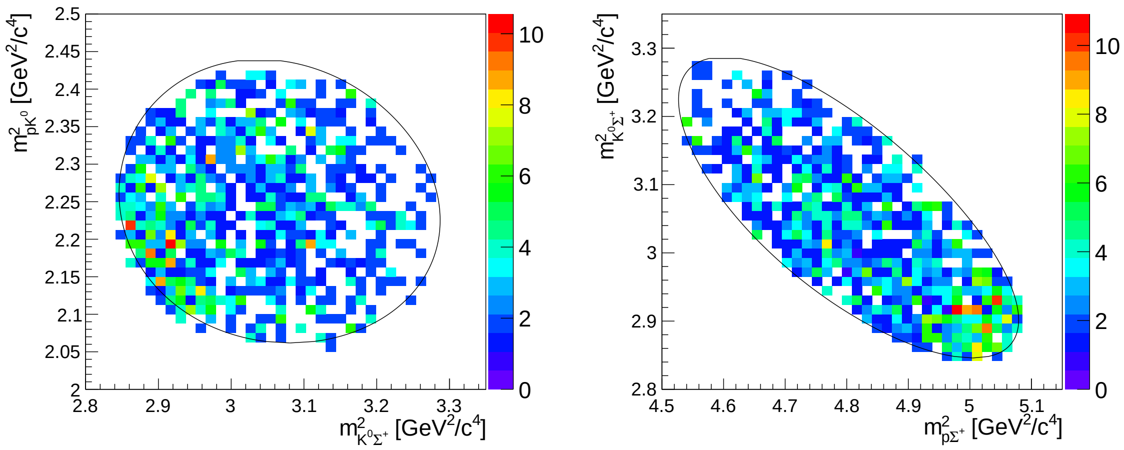

Figure 7.2 – Dalitz plots of K^0p - $K^0\Sigma^+$ (left) and $K^0\Sigma^+$ - $p\Sigma^+$ (right) subsystems. The data is acceptance and efficiency corrected. The black line indicates the kinematic limits of the distributions.

at low $K^0\Sigma^+$ and high $p\Sigma^+$ masses is observed. Monte Carlo simulations shows that the contribution due to the background channels discussed in Sec. 6.2.7 is uniformly distributed in the $pK^0\Sigma^+$ three-body final state. Considering also the low background contribution estimated to be on the level of 5.85%, namely 50 events out of 905 reconstructed, it can be concluded that the observed non-uniformity is due to the signal channel.

7.2 Polarization Observables

To determine polarization observables, the events which are uniquely reconstructed by the "SQT hit" method are excluded, in order to avoid asymmetry affects which are caused by inactive regions in the SQT (Sec. 6.2.2).

7.2.1 Σ^+ production polarization

Angular momentum conservation in the $\Sigma^+ \to (N\pi)^+$ decay requires the orbital momentum l in the $N\pi$ system to be either 0 or 1, where $l = 1$ is related to the spin-flip of the nucleon with respect to the decaying hyperon. Parity conservation would require $l = 1$, however parity non-conservation in the weak decay of the Σ^+ also allows $l = 0$ in the $N\pi$ system. The wave function of the nucleon-pion system thus has both S ($l = 0$) and P ($l = 1$) wave components:

$$\psi_{B\pi} = A_s\psi_s + A_p\psi_p \tag{7.4}$$

where A_s and A_p are the amplitudes of S and P wave respectively.
Using Clebsch-Gordon coefficients we can write:

$$\psi_{B\pi} = A_s Y_{00}\chi_{+\frac{1}{2}} + A_p\left(\sqrt{\frac{2}{3}}Y_{11}\chi_{-\frac{1}{2}} - \sqrt{\frac{1}{3}}Y_{10}\chi_{+\frac{1}{2}}\right) \tag{7.5}$$

The resulting angular distribution of the nucleon from Σ^+ decay is given as [77]:

$$I(\theta,\varphi) = \frac{1}{N_0}\frac{dN}{d\Omega} = |\psi_{B\pi}|^2 = \frac{1}{4\pi}\left(1 + \alpha\vec{P}\frac{\vec{p_B}}{|p_B|}\right) = \frac{1}{4\pi}\left(1 + \alpha P_N \cos\theta_n^*\right) \tag{7.6}$$

where:

P_N is the hyperon polarization, depending on the production process;

θ_n^* is the angle between the normal vector to the production plane and the daughter nucleon direction in the Σ^+ rest frame (Fig. 7.3). The production plane is defined by the beam and Σ^+ momentum vectors. Parity conservation requires the polarization to be perpendicular to the production plane.

α is the asymmetry parameter which is defined as:

$$\alpha \equiv \frac{-2\Re e A_s A_p^*}{|A_s|^2 + |A_p|^2} \tag{7.7}$$

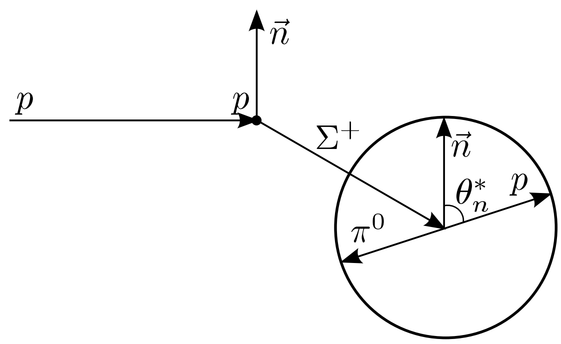

Figure 7.3 – Schematic illustration of the vectors and angels relevant in the production and decay of the Σ^+ hyperon.

For the $\Sigma^+ \to p\pi^0$ decay channel the asymmetry parameters $\alpha = -0.98^{+0.017}_{-0.015}$, while for the $\Sigma^+ \to n\pi^+$ decay channel $\alpha = 0.068 \pm 0.013$ [78].

Integrating Eq. (7.6) over negative and positive $\cos\theta_n^*$ gives:

$$\frac{N^-}{N_0} = \int_{-1}^{0}(1 + \alpha P_N \cos\theta_n^*)d(\cos\theta_n^*) = 1 - \frac{1}{2}\alpha P_N \tag{7.8}$$

$$\frac{N^+}{N_0} = \int_{0}^{1}(1 + \alpha P_N \cos\theta_n^*)d(\cos\theta_n^*) = 1 + \frac{1}{2}\alpha P_N \tag{7.9}$$

Solving Eq. (7.8) and Eq. (7.9) together defines the formula used to determine the Σ^+ polarization:

$$P_N = \frac{2}{\alpha}\frac{N^+ - N^-}{N^+ + N^-} \tag{7.10}$$

For the polarization measurement the $\Sigma^+ \to p\pi^0$ decay channel is selected (Sec. 6.2.6) due to the much larger asymmetry parameter as comparing to that of the $\Sigma^+ \to n\pi^+$ decay channel.

The polarization is obtained with Eq. (7.10) as a function of the Σ^+ polar angle in the CMS and of the Feynman variable, which is defined as the ratio of the longitudinal momentum to the maximum possible longitudinal momentum of the Σ^+: $x_f = p_{l_{\Sigma^+}}/p_{lmax_{\Sigma^+}}$), is shown in Fig. 7.4 and in Fig. 7.5, respectively.

The value of polarization can be alternatively obtained by fitting the $\cos\theta_n^*$ distribution with the polynomial function $f(x) = p_0 + p_1 x$ (Fig. 7.6). In this case the polarization is given as follows:

$$P_N = \frac{1}{\alpha}\frac{p_1}{p_0} \tag{7.11}$$

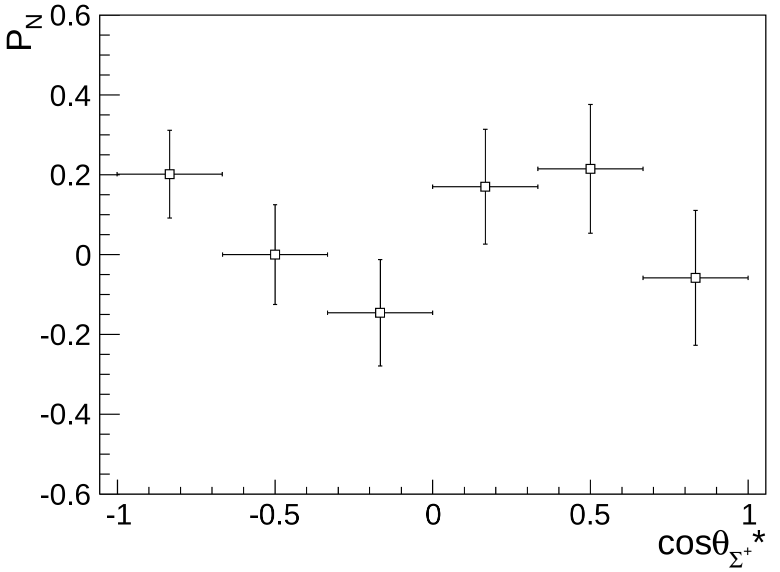

Figure 7.4 – Polarization of Σ^+ as a function of its polar angle in the CMS. See also Tab. VI in Add. 4.

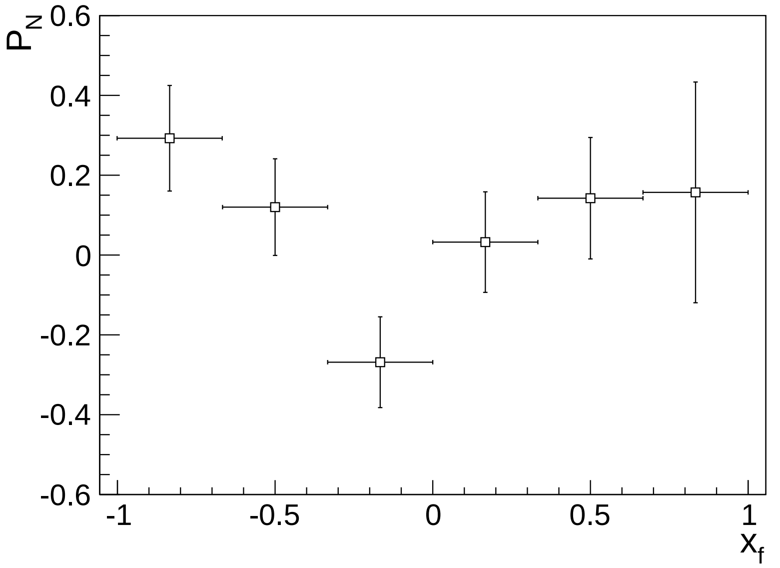

Figure 7.5 – Polarization of Σ^+ as a function of the Feynman variable x_f. See also Tab. VII in Add. 4.

The calculation with this method gives $P_N = +6.8 \pm 9.1\%$. The small number of entries in each bin makes the determination of parameter p_1 very uncertain. As result the method provide too big errors for a polarization value.

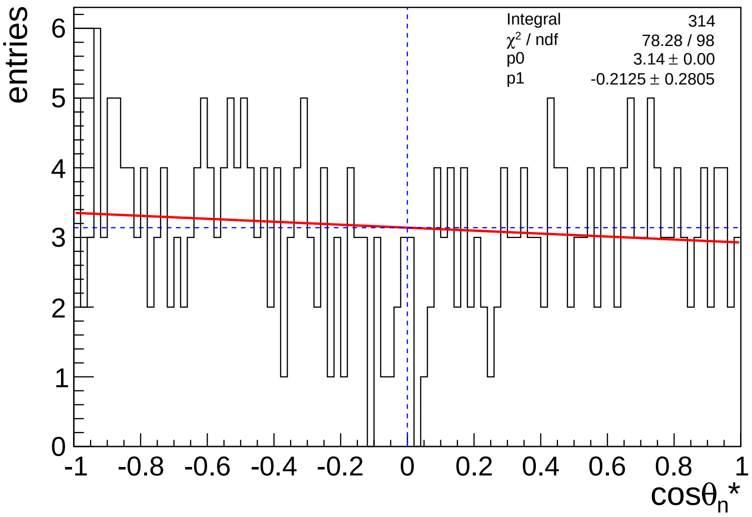

Figure 7.6 – The $\cos\theta_n^*$ distribution of the selected $pK^0\Sigma^+$ event sample. The parameter p_0 (horizontal blue-dashed line) is fixed to the number of entries divided by the number of bins in the histogram.

Fig. 7.7 shows the $\cos\theta_n^*$ distribution of reconstructed MC events with a generated polarization (Sec. 3.3.2) of +30%. The value deduced from Eq. (7.11) is $+29.5 \pm 1\%$ which is consistent with the value generated in the MC data sample.

The gap in the distribution around $\cos\theta_n^* = 0$ in Fig. 7.7 is a result of the lower limit on the kink angle between the Σ^+ and the decay proton momentum direction (vertical line at $\alpha = 4.5°$ in Fig. 6.31). Due to symmetry of this cut around $\cos\theta_n^* = 0$ it does not influence the polarization measurement.

To plot the Σ^+ polarization as a function of the Σ^+ transverse momentum, the

Σ^+ transverse momentum, $p_{t_{\Sigma^+}}$ [GeV/c]	Σ^+ polarization, P_N
0.16 ± 0.06	0.011 ± 0.074
0.28 ± 0.06	0.117 ± 0.084

Table 7.1 – Σ^+ polarization as a function of the Σ^+ transverse momentum.

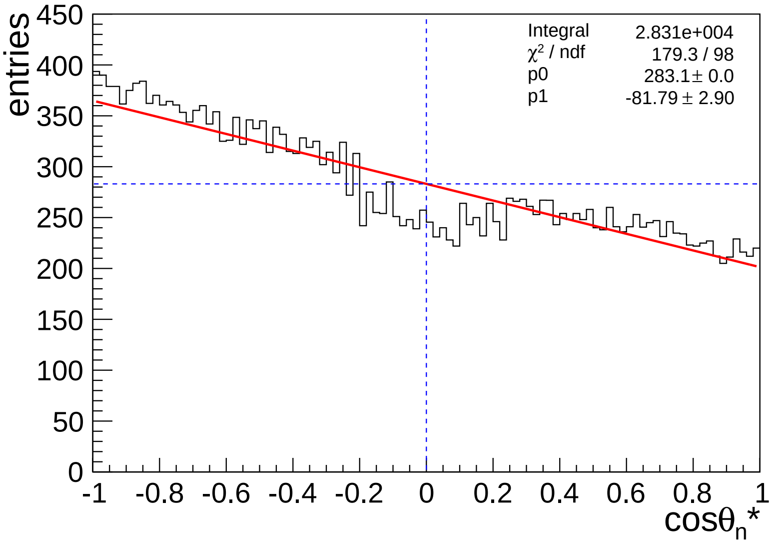

Figure 7.7 – The $\cos\theta_n^*$ distribution of reconstructed MC events. A dip at at $\cos\theta_n^* = 0$ is a result of the limit on the kink angle between Σ^+ and proton directions.

data is divided into two samples as shown in Fig. 7.8. For each sample the polarization based on Eq. (7.10) is calculated. The obtained result is shown in Tab. 7.1.

7.2.2 Σ^+ analyzing power

The Σ^+ analyzing power is a measure of the influence of the spin direction of the projective proton on the differential Σ^+ cross section. The analyzing power is determined with the same method as the asymmetry of $\vec{p}p \to pp$ elastic scattering (Sec. 6.1.4). It is defined based on Eq. (6.4) as follows:

$$A_N = \frac{1}{P_b \cos(\varphi)} \frac{\sqrt{N^+(\theta^*, \varphi) N^-(\theta^*, \varphi + \pi)} - \sqrt{N^-(\theta^*, \varphi) N^+(\theta^*, \varphi + \pi)}}{\sqrt{N^+(\theta^*, \varphi) N^-(\theta^*, \varphi + \pi)} + \sqrt{N^-(\theta^*, \varphi) N^+(\theta^*, \varphi + \pi)}} \tag{7.12}$$

where all variables are the same as in Eq. (6.4) and Eq. (6.6). The beam polarization P_b is deduced from the analysis of $\vec{p}p \to pp$ elastic scattering (Sec 6.1.4). The azimuthal angle of Σ^+ tracks from each θ^* bin is divided into two bins according to Fig. 7.9.

Due to the low statistics the number of bins to study the dependence of the analyzing power on polar angle θ^* of the Σ^+ momentum direction in the $\vec{p}p$ CMS frame, the full

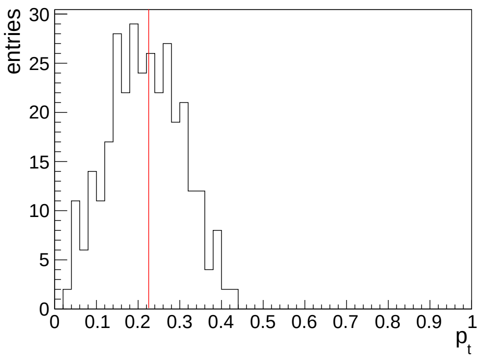

Figure 7.8 – Distribution of Σ^+ transverse momentum of the selected events. The vertical red line separate data into two bins.

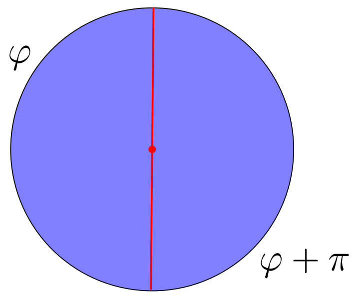

Figure 7.9 – Bins in φ. The red line indicates the spin direction of the beam (up or down).

$\cos\theta^*_{\Sigma^+}$ range is divided into only six bins. Fig. 7.10 and Fig. 7.11 show the resulting analyzing power as a function of $\cos\theta^*_{\Sigma^+}$ and as a function of the Feynman variable, respectively.

7.2.3 Spin transfer coefficient

The spin transfer coefficient D_{NN} quantifies the influence of a polarized initial state on the Σ^+ polarization. D_{NN} is also called the depolarization parameter. The angular distribution of the nucleon from Σ^+ decay is defined as [26]:

$$I = \frac{1}{N_0}\frac{dN}{d\Omega} = \frac{1}{4\pi}(1 + P_b A_N \cos\phi)(1 + \alpha\cos\theta^*_n P_N + \alpha\cos\theta^*_n P_b D_{NN}\cos\phi) \qquad (7.13)$$

where ϕ is the angle between the beam and the Σ^+ polarization directions.

Integration of Eq. (7.13) over $\cos\phi$ in the range [0,1] gives the angular distributions of events with the beam and the Σ^+ polarization direction pointing into the same hemisphere:

$$\begin{aligned} I^{\uparrow\uparrow} = \int_0^1 I d(\cos\phi) = 1 + \frac{1}{2}\,P_b A_N + \alpha\cos\theta^*_n \times \\ \left(\frac{1}{2}\,P_b D_{NN} + \frac{1}{2}\,P_b A_N P_N + \frac{1}{3}\,{P_b}^2 A_N D_{NN} + P_N\right) \end{aligned} \qquad (7.14)$$

Applying Eq. (7.10) to the considered sample gives the polarization $P^{\uparrow\uparrow}$:

$$P^{\uparrow\uparrow} = \frac{2}{\alpha}\,\frac{N^{\uparrow\uparrow +} - N^{\uparrow\uparrow -}}{N^{\uparrow\uparrow +} + N^{\uparrow\uparrow -}} = \frac{2\,{P_b}^2 A_N D_{NN} + (3\,D_{NN} + 3\,A_N P_N)\,P_b + 6\,P_N}{6 + 3\,P_b A_N} \qquad (7.15)$$

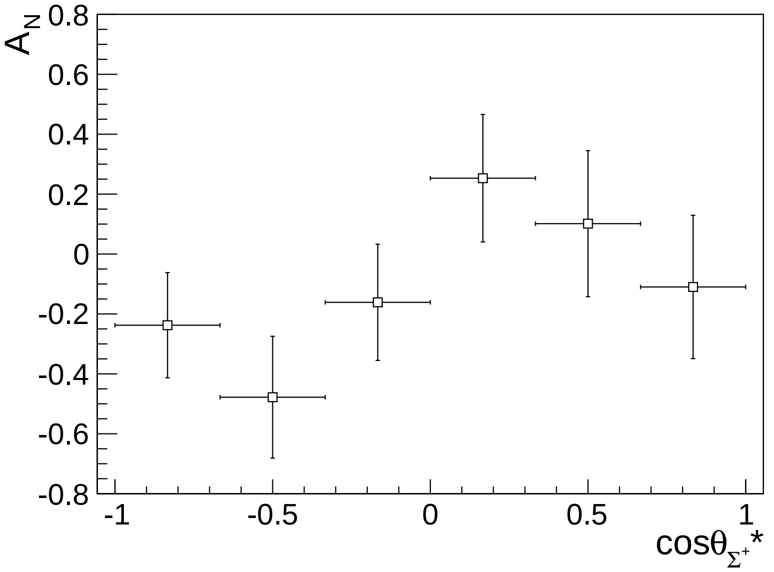

Figure 7.10 – The analyzing power of Σ^+ as a function of its CMS polar angle. See also Tab. VIII in Add. 4.

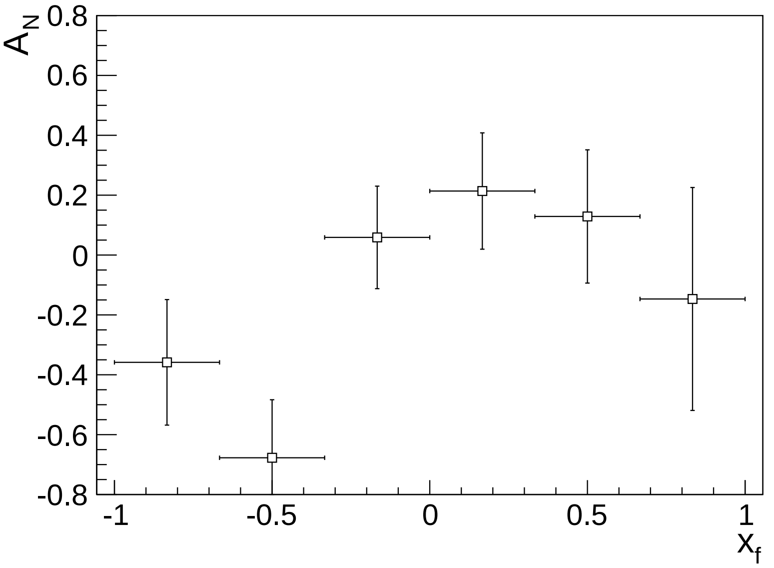

Figure 7.11 – The analyzing power of Σ^+ as a function of the Feynman variable x_f. See also Tab. IX in Add. 4.

where $N^{\uparrow\uparrow^{+}}$ and $N^{\uparrow\uparrow^{-}}$ are defined as follows:

$$N^{\uparrow\uparrow^{+}} = N_0 \int_0^1 I^{\uparrow\uparrow} d(\cos\theta_n^*)\,, \qquad N^{\uparrow\uparrow^{-}} = N_0 \int_{-1}^0 I^{\uparrow\uparrow} d(\cos\theta_n^*) \tag{7.16}$$

In the same way the polarization is determined for the sample with the beam and the Σ^+ polarization direction pointing into the opposite hemispheres (Eq. (7.17)). In this case the Eq. (7.13) is integrated over $\cos\phi$ in the range [-1,0].

$$P^{\uparrow\downarrow} = \frac{-2\,{P_b}^2 A_N D_{NN} + (3\,D_{NN} + 3\,A_N P_N)\,P_b - 6\,P_N}{-6 + 3\,P_b A_N} \tag{7.17}$$

By solving Eq. (7.15) and Eq. (7.17) together one obtains the formula to determine

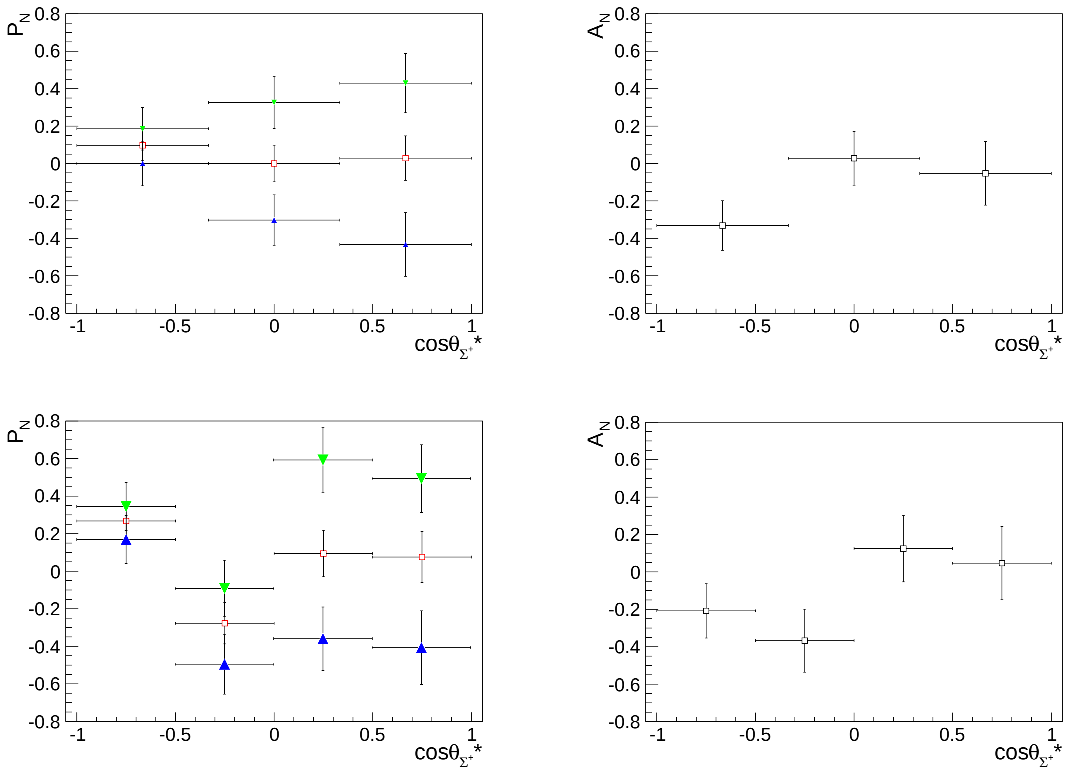

Figure 7.12 – Left: the polarization of the Σ^+ hyperon as a function of its polar angle in the CMS for events with beam and Σ^+ polarization direction in the same hemisphere $P^{\uparrow\uparrow}$ (green) and in opposite hemispheres $P^{\uparrow\downarrow}$ (blue). The red data points show the beam-spin-averaged Σ^+ polarization. Right: the analyzing power used in Eq. (7.18) to calculate the depolarization.

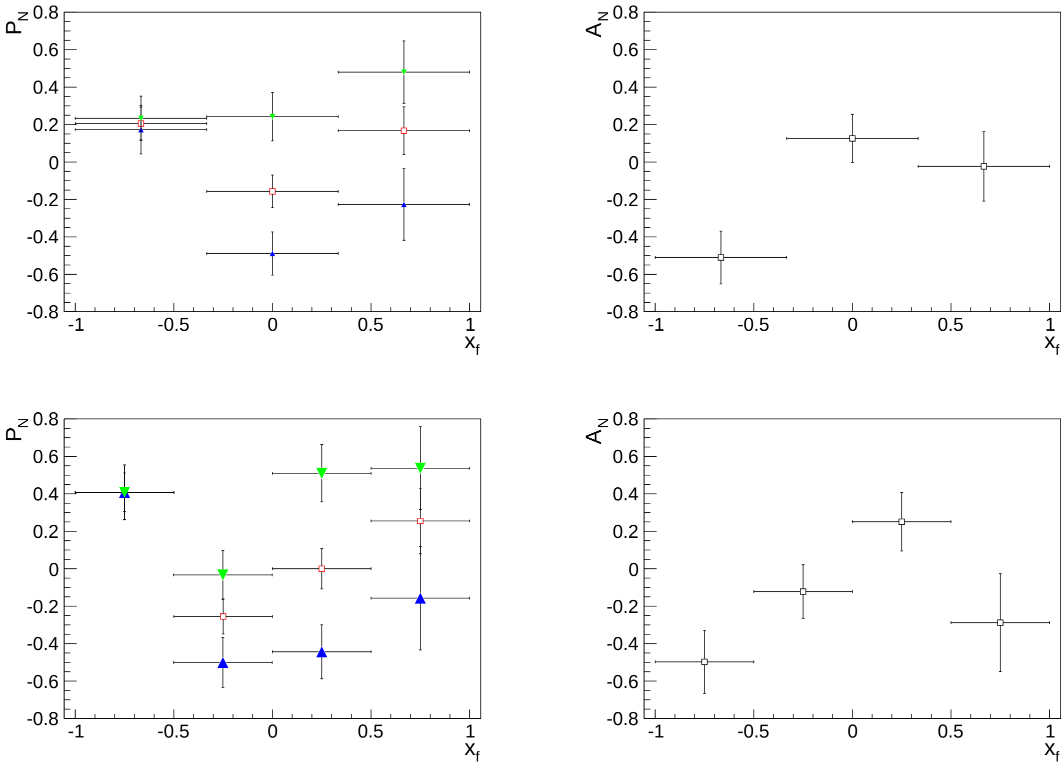

Figure 7.13 – Left: the polarization of the Σ^+ hyperon as a function of the Feynman variable x_f for events with beam and Σ^+ polarization direction in the same hemisphere $P^{\uparrow\uparrow}$ (green) and in opposite hemispheres $P^{\uparrow\downarrow}$ (blue). The red data points show the beam-spin-averaged Σ^+ polarization. Right: the analyzing power used in Eq. (7.18) to calculate the depolarization.

the spin transfer coefficient:

$$D_{NN} = \frac{3}{4} \frac{\left(4 - {P_b}^2 {A_N}^2\right)\left(P^{\uparrow\uparrow} - P^{\uparrow\downarrow}\right)}{P_b\left(3 - {P_b}^2 {A_N}^2\right)} \tag{7.18}$$

The presence of a finite depolarization effect can be immediately seen from a difference between $P^{\uparrow\uparrow}$ and $P^{\uparrow\downarrow}$. Fig. 7.12 (left) shows $P^{\uparrow\uparrow}$ (green) and $P^{\uparrow\downarrow}$ (blue) as a function of the Σ^+ polar angle in the CMS calculated for 3 (top) and 4 (bottom) bins in $\cos\theta^*_\Sigma$, respectively. In the backward region ($\cos\theta^*_\Sigma \in [-1, -0.5]$) the difference between $P^{\uparrow\uparrow}$ and $P^{\uparrow\downarrow}$ is negligible within the given statistical errors. However, moving to the forward region, a difference appears and in the region $\cos\theta^*_\Sigma \in [0, 1]$ it approaches a constant maximal value. The same behavior is observed as a function of

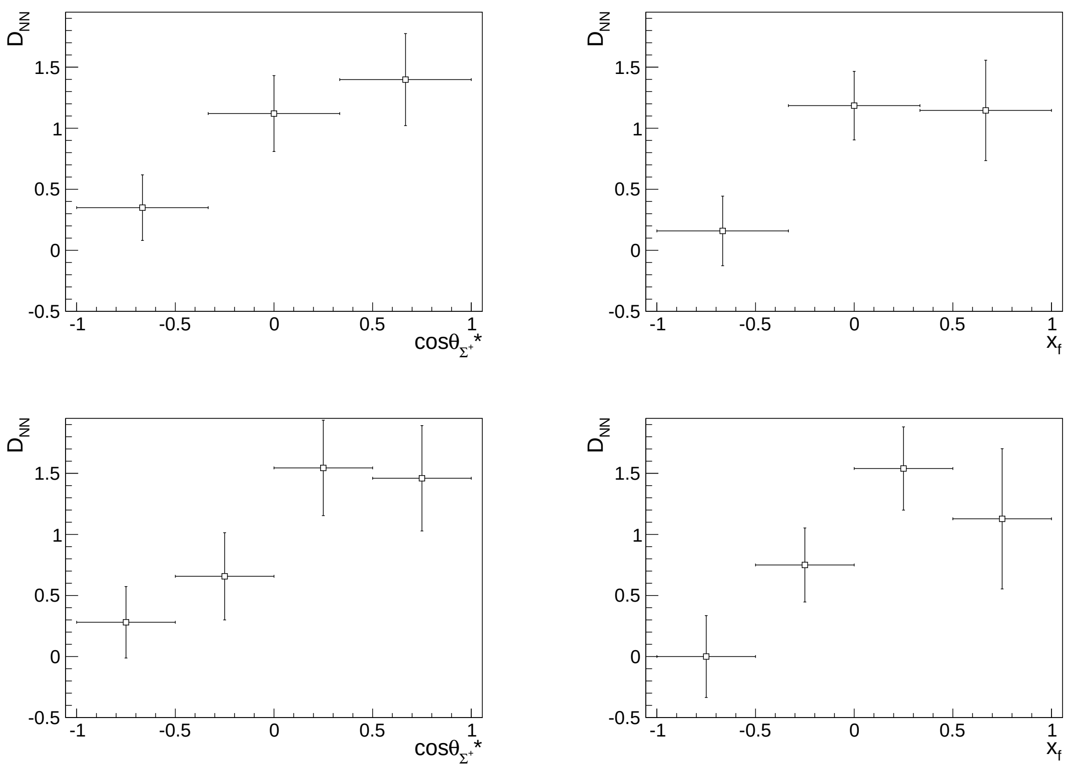

Figure 7.14 – Spin transfer coefficient as a function of the Σ^+ polar angle in the CMS (left) and of the Feynman variable x_f (right). See also Tab. X and XI in Add. 4.

the Feynman variable x_f(Fig. 7.13). The resulting value of the spin transfer coefficient D_{NN} obtained with Eq. (7.18) as a function of the Σ^+ polar angle in the CMS and of the Feynman variable x_f is shown in Fig. 7.14 right and left, respectively.

Chapter 8

Discussion

8.1 Cross Section

For the reaction $pp \to pK^0\Sigma^+$ a total cross section $\sigma = (2.95 \pm 0.11_{stat} \pm 0.22_{syst})\ \mu b$ is obtained (Sec. 7.1.1). This result is compared to total cross section values obtained in

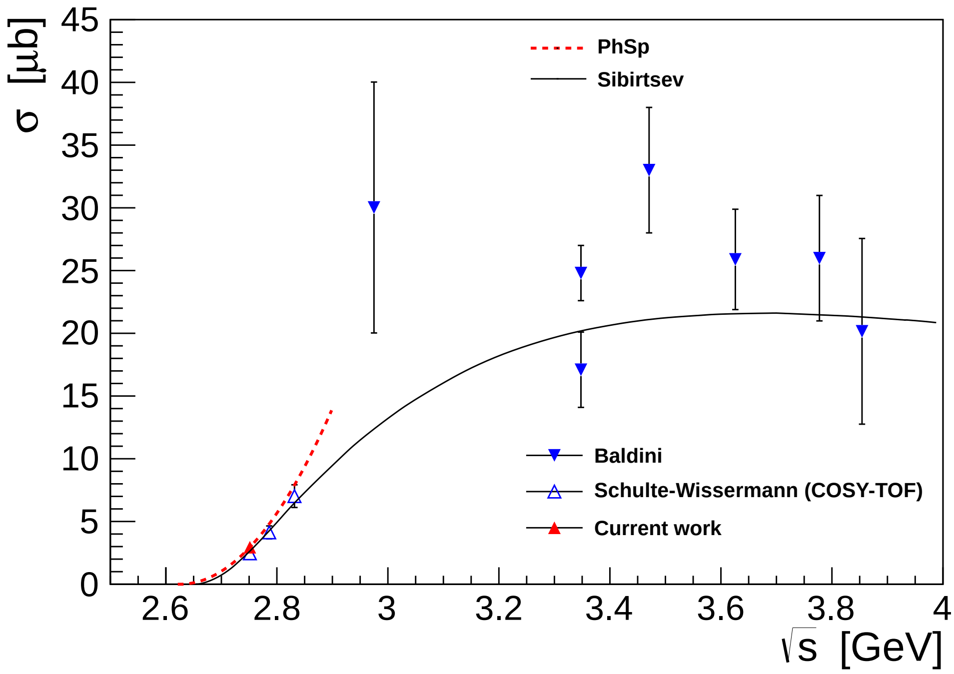

Figure 8.1 – Cross section of the reaction $pp \to pK^0\Sigma^+$. The red point shows the result obtained in the current work. The error bar is smaller than the symbol size. The red dashed curve represents the phase space dependence, the black solid curve shows the resonance model of Ref. [13].

previous measurements for a wider energy region in Fig. 8.1, and for the near-threshold region in Fig. 8.2.

The bubble chamber data [27] (full blue triangles in Fig. 8.1 at $\sqrt{s}$ between 3 GeV and 4 GeV) show no distinct energy dependence within the errors. In contrast, the cross sections previously measured by COSY-TOF [28] close to threshold (open blue triangles) clearly rise with the energy.

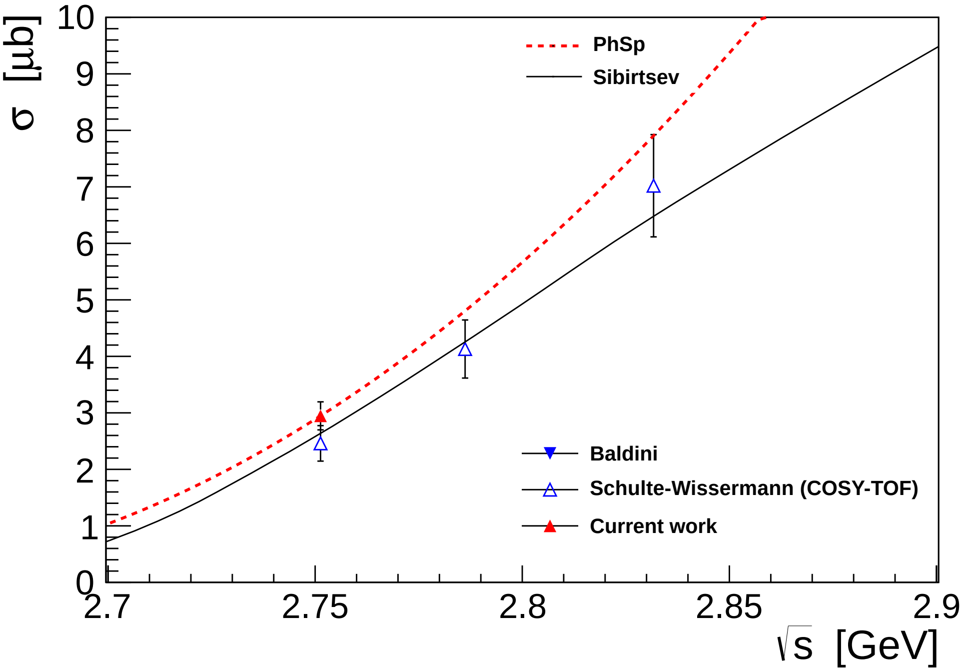

Figure 8.2 – Cross section of the reaction $pp \rightarrow pK^0\Sigma^+$ near threshold. The red dashed curve represents the phase space dependence, the black solid curve shows the resonance model of Ref. [13].

The result of the current work is in very good agreement with the previous measurement of COSY-TOF which used a different detector setup and a different reconstruction method. In the previous work [28] scintillating fiber hodoscopes were used for track measurement instead of SQT and STT. Due to the much poorer track resolution compared to the present setup, in the previous work the $pK^0\Sigma^+$ final state was reconstructed by using the time-of-flight information, while in the present work it is fully defined by the tracking information.

The red dashed line in Figs. 8.1 and 8.2 denotes the excitation function which results from a pure phase space distribution of non-interacting final state particles in relative s-wave with respect to each other. The 3-body phase space is defined as [79], [80]:

$$\Phi_3 = \frac{\pi^2}{4s} \int_{(m_\Sigma + m_p)^2}^{(\sqrt{s} - m_K)^2} \lambda^{1/2}(s, s_Q, m_K^2) \lambda^{1/2}(s_Q, m_\Sigma^2, m_p^2) \frac{ds_Q}{s_Q} \tag{8.1}$$

where the λ-function is defined by $\lambda(x, y, z) = (x - y - z)^2 - 4yz$ and $s_Q = m_{\Sigma p}^2 = (P_\Sigma + P_p)^2$. In the nonrelativistic limit Eq. (8.1) reduces to:

$$\Phi_3 = \frac{1}{2^7 \pi^2} \frac{(m_p m_K m_\Sigma)^{1/2}}{(m_p + m_K + m_\Sigma)^{3/2}} \, \varepsilon^2 \tag{8.2}$$

where ε is the excess energy above threshold which is defined by $\varepsilon = \sqrt{s} - \sqrt{s_0}$ with $\sqrt{s_0} = m_p + m_{K^0} + m_{\Sigma^+}$. As a result, the energy dependence of the cross section in the nonrelativistic limit is given by $\sigma \simeq c_0 \cdot (\sqrt{s} - \sqrt{s_0})^2$. Normalization to the cross section obtained in this work gives $c_0 = (185.5 \pm 15.6)\ \mu b\ \ \mathrm{GeV}^{-2}$. The cross section data close to threshold are quite well described by the phase space dependence, however the data at higher energies are drastically overestimated.

The solid black line corresponds to the resonance model calculation by Sibirtsev and Cassing [13]. This model seems to successfully describe the data in the whole energy range. The calculation of Ref. [13] differs from that of Ref. [30] (dashed line in Fig. 1.10) by a different set of coupling constants and cut-off values.

Model predictions for the total cross section of the reaction $pp \to pK^0\Sigma^+$ are collected in Tab. 8.1.

Model	σ [μb]
Ferrari [1]	17.2
Sibirtsev [13]	2.64
Li [5]	2.87

Table 8.1 – Predictions for the total $pp \to pK^0\Sigma^+$ cross section at $p_{beam} = 2.95 GeV/c$ obtained with different models.

The calculation of Li [5] considered the reaction $BB \to NYK$ with proton, neutron and Δ-resonances in the entrance channel. Both pion and kaon exchange were taken into account. Coupling constants and cut-off parameters were taken from Ref. [2].

As a conclusion, the resonance model is able to describe the available data, however, the free parameters of the model, namely coupling constants and cut-off parameters, are not well constrained by the measured total cross sections. A similar agrement is obtained with different combinations of coupling constants deduced from different input data and different cut-off parameters (see e.g. Refs. [13], [5]).

8.2 Dalitz Plot

Projections of the Dalitz plot (Sec. 7.1.2) are shown in Fig. 8.3. The measured distributions clearly deviate from the phase space dependence at low $K^0\Sigma^+$ masses and at high $p\Sigma^+$ masses.

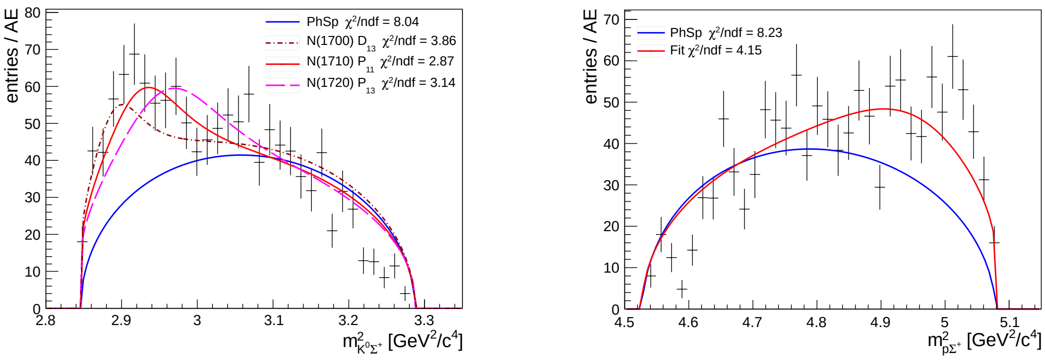

Figure 8.3 – Projections of the Dalitz plot on the $K^0\Sigma^+$ (left) and the $p\Sigma^+$ (right) axis (See also Tab. I and Tab. II in Add. 4). The blue line denotes the phase space distribution. The other lines in $m_{K^0\Sigma^+}$ spectrum (left) correspond to fits using the coherent sum of phase space and Breit-Wigner functions. As the Breit-Wigner resonances N(1700) D_{13} (dot-dashed grey line), N(1710) P_{11} (solid red line), N(1720) P_{13} (dashed magenta line) were taken. The red solid line in $m_{p\Sigma^+}$ spectrum (right) is obtained from a fit to the kinematical reflection of the N(1710) P_{11} contribution.

The enhancement at low $K^0\Sigma^+$ masses may be due to nucleon resonance contribution. According to the resonance model the reaction can proceed in two steps, namely $pp \to pN^*$ and $N^* \to K^0\Sigma^+$, where the N^* resonance is responsible for the production of the $K^0\Sigma^+$ pair.

The list of resonances which may contribute is presented in Tab. 8.2. As the most simple approach it is studied whether the measured distribution can be described by a

Particle	$L_{2I \cdot 2J}$	Mass [MeV]	Width [MeV]	Overall status	Status as seen in ΣK
N(1650)	S_{11}	1645-1670	145-185	****	**
N(1675)	D_{15}	1670-1680	130-165	****	-
N(1680)	F_{15}	1680-1690	120-140	****	-
N(1700)	D_{13}	1650-1750	50-150	***	*
N(1710)	P_{11}	1680-1740	50-250	***	*
N(1720)	P_{13}	1700-1750	150-300	****	*
Δ(1600)	P_{33}	1550-1700	250-450	***	-
Δ(1700)	D_{33}	1670-1750	200-400	****	*

Table 8.2 – The nucleon resonances coupled to ΣK channels [78]. The stars indicate the evidence of existence according to the classification of Ref. [78]: **** - certain; *** - very likely; ** - fair; * - poor.

contribution of a single resonance.

For each of the resonances listed in Tab. 8.2 the $K^0\Sigma^+$ squared mass spectrum is fitted with the coherent sum of a Breit-Wigner and a phase space distribution. For the peak position of the Breit-Wigner distribution the nominal value of the resonance is taken, for the width the central value of the range given in table is used. The obtained result is shown in Fig. 8.3 (left) for N(1700) D_{13}, N(1710) P_{11} and N(1720) P_{13}. The best agrement is found for the N(1710) P_{11} resonance.

The enhancement at high $p\Sigma^+$ masses can be simply a kinematical reflection of the resonance contribution. To investigate whether this assumption is correct, the $pK^0\Sigma^+$ final state is simulated based on the phase space distribution with an additional contribution of the N(1710) P_{11} resonance with $m_{P_{11}} = 1710$ MeV and $\Gamma_{tot} = 150$ MeV. The following parametrization is used:

$$\frac{d^2\sigma}{dm^2_{K\Sigma^+}dm^2_{p\Sigma^+}} = N\left|-\frac{\sqrt{s_{K\Sigma^+}}\,\Gamma_{tot}}{s_{K\Sigma^+} - m_R^2 + \Im m(\sqrt{s_{K\Sigma^+}}\,\Gamma_{tot})} + C\right|^2 \tag{8.3}$$

where N is a normalizing factor. The first term corresponds to the Breit-Wigner resonance, and second term correspond to the phase space contribution.

The result of this study is shown in Fig. 8.4. The upper part shows the pure phase space without resonance contribution. As expected, the Dalitz plot is uniformly filled, demonstrating the proper functionality of the event generator. The enhancement at low $K^0\Sigma^+$ masses in the lower part is due to the resonance contribution. The projections of the simulated Dalitz plots on the $K^0\Sigma^+$ and $p\Sigma^+$ axes are shown in Fig. 8.5. In the obtained $K^0\Sigma^+$ mass distribution the resonance contribution is fitted with the same Breit-Wigner parameters as used for the experimental data. The resulting deviation of the distribution from the phase space in the $p\Sigma^+$ projection is due to the kinematical reflection of the simulated N^* contribution. As shown in Fig. 8.3 (right) the fit curve to the distribution in Fig. 8.5 (right) is in fair agrement with the measured data.

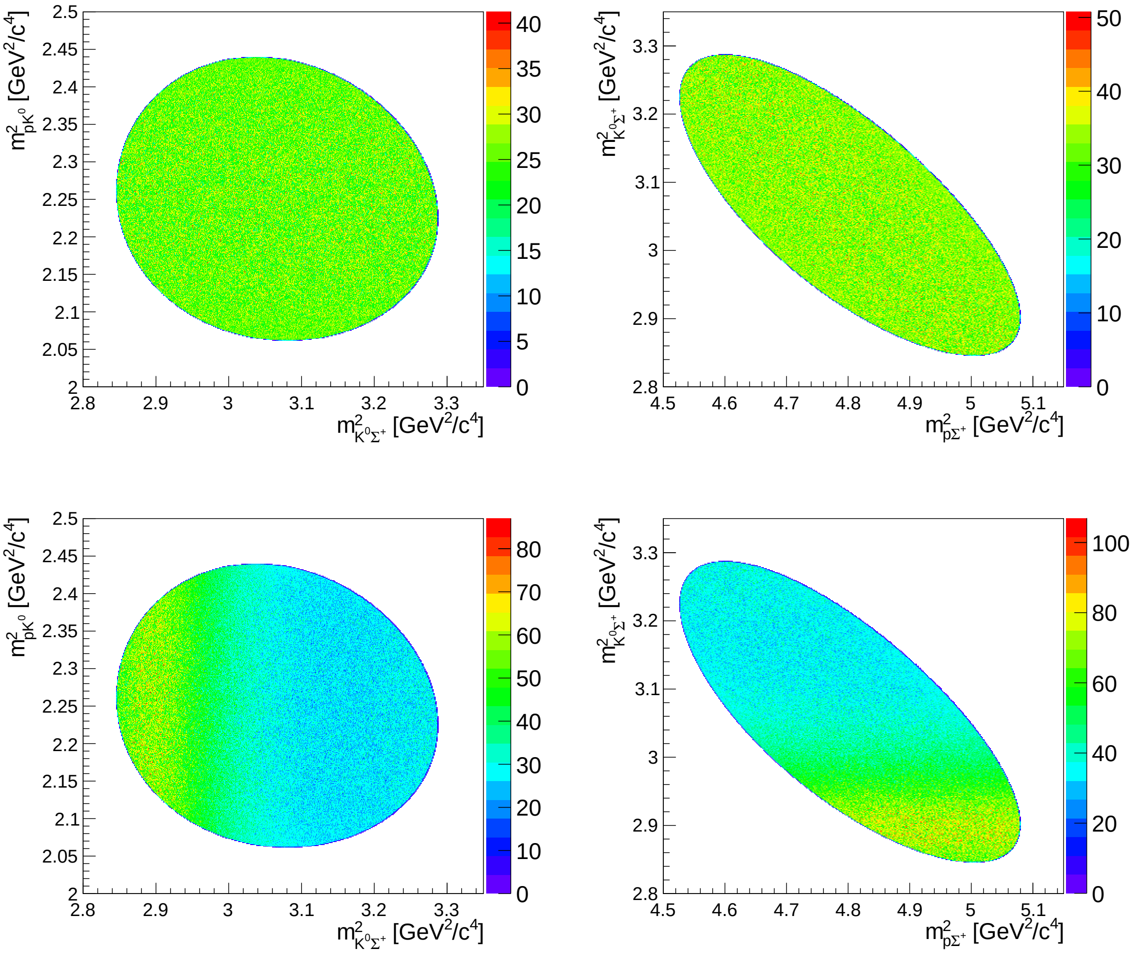

Figure 8.4 – The uniform Dalitz plots distributions in the upper row are generated by a MC simulations based on pure phase space. The Dalitz plots in the lower row are obtained from the coherent sum of phase space and a Breit-Wigner resonance.

Final State Interaction (FSI) between p and Σ^+ also causes a deviation from a uniform Dalitz plot. However, the FSI only contributes at small relative energies as observed for the $pK^+\Lambda$ final state [26]. An attractive interaction would therefore result in an enhancement at low $p\Sigma^+$ masses. The shape of the measured $p\Sigma^+$ mass distribution (Fig. 8.3 (right)) could be also explained by suppression at low masses instead of an enhancement at high masses. This could be a consequence of repulsive final state interaction. However, a strongly repulsive interaction between the two baryons is not expected (see Tab. 3 in Ref. [45] and references therein). A strongly attractive $p\Sigma^+$ final state interaction can be excluded from the non-observation of an enhancement at low $p\Sigma^+$ masses.

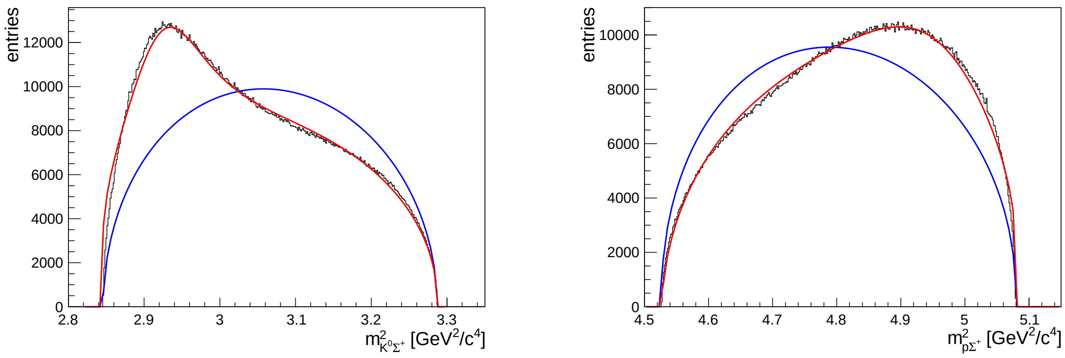

Figure 8.5 – Projections of the simulated Dalitz plots on the $K^0\Sigma^+$ (left) and the $p\Sigma^+$ (right) axes. The blue line denotes the phase space distribution. The red line corresponds to the fit with a convolution of phase space and Breit-Wigner functions.

The previous COSY-TOF measurement at $p_{beam} = 3.015$ GeV/c beam momentum [28] (Fig. 1.11) also shows no significant contribution of $p\Sigma^+$ final state interaction.

8.3 Σ^+ Polarization

As there are no data on Σ^+ polarization in the reaction $pp \rightarrow pK^0\Sigma^+$, the results determined in this work are compared to that from inclusive high energy Σ^+ production. The high energy data have been presented as a function of transverse momentum p_t. Therefore the $pK^0\Sigma^+$ data sample is subdivided in two bins of the Σ^+ transverse momentum (Sec. 7.2.1). The resulting polarization values are shown together with high energy data in Fig. 8.6 with red up-pointing triangles. The high energy data points are from the Fermilab experiments E497, E620 at 400 GeV and E761 at 800 GeV [32], [33](see also Sec. 1.4.3). They indicate an increase of the Σ^+ polarization with p_t to about 20% in the range $p_t \in [0, 0.8]$ GeV/c and further on a decrease to about 10% at $p_t \simeq 2$ GeV/c.

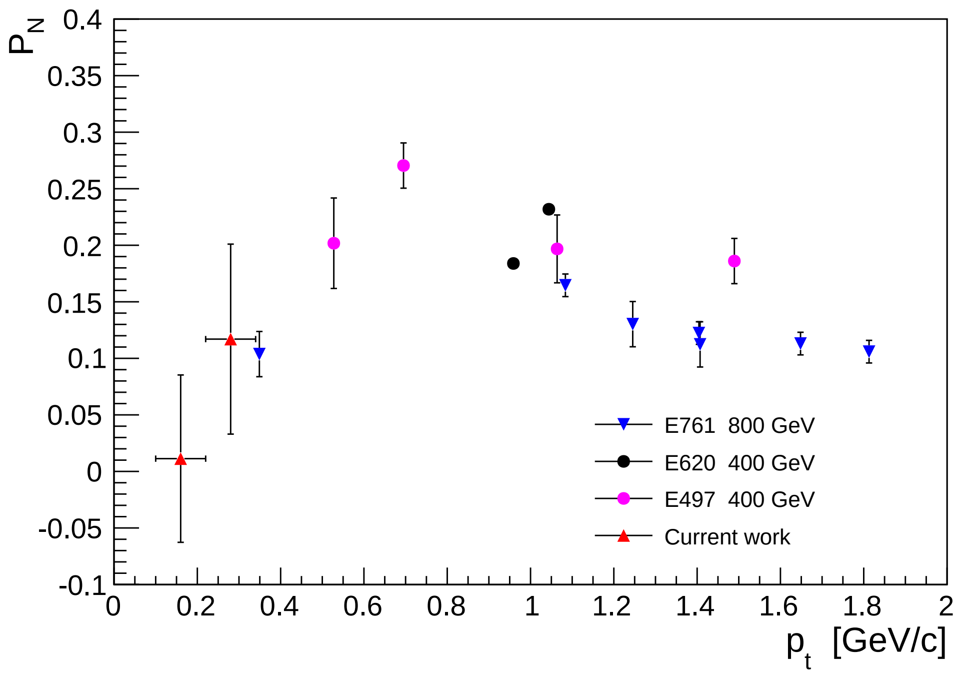

Figure 8.6 – Σ^+ production polarization as a function of the Σ^+ transversal momenta p_t. The red up-pointing triangles indicate the result of this work. Other data points represent the inclusive measurements made in Fermilab.

The error bars of the current measurement only include the statistical uncertainty. Within the errors the obtained Σ^+ polarization is in agrement with the p_t dependance of the high energy data.

It should be taken into account that the current measurement was done with a polarized beam. The Σ^+ polarization is obtained from the average of two spin orientations. Due to the full azimuthal symmetry of the COSY-TOF detector, the influence of the beam polarization to the Σ^+ polarization is canceled.

The polarization of the Σ^+ as a function of its polar angle in the CMS is shown in Fig. 8.7 by red down-pointing triangles together with the polarization of the Λ hyperon measured by COSY-TOF at 2.95 GeV/c beam momentum. Green triangles correspond to the previous studies of the reaction $pp \to pK^+\Lambda$ of COSY-TOF [54], while the blue triangles correspond to the Λ polarization evaluated in Ref. [26] from the same data sample as used in this work. In forward and backward directions corresponding to $\cos\theta^*_{hyperon} = \pm 1$ the polarization has to be zero for symmetry reasons. The positive shift of the Σ^+ polarization in the backward region is most probably due to a systematic effect to be further studied. It can be caused by a contribution of background channels

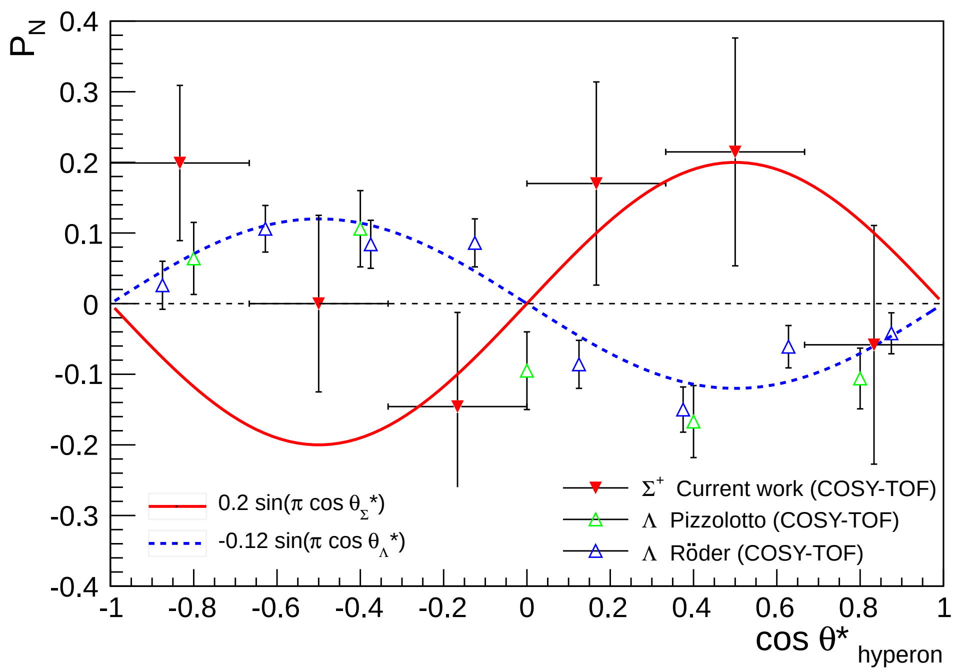

Figure 8.7 – Hyperon polarization as a function of hyperon polar angle in the CMS. The red down-pointing triangles indicate the Σ^+ polarization as the result of the current work, while the green [54] and blue [26] up-pointing triangles correspond to the Λ hyperon polarization measured by COSY TOF at 2.95 GeV/c beam momentum.

and by the selection criteria for the $\Sigma^+ \to p\pi^0$ decay channel. At $\cos\theta^*_{hyperon} = 0$ the polarization changes sign which is a consequence of the forward-backward symmetry of the entrance channel.

The Σ^+ and Λ polarization distributions appear to have the same shape but with opposite sign. This is illustrated in Fig. 8.7 by a fit to the data with a sine function: the red solid line for P_{Σ^+} and the blue dashed line for P_Λ. The amplitude of the sine function determines the maximum value of the polarization, which is about 20% for Σ^+ and 12% for Λ.

8.4 Σ^+ Analyzing Power A_N

The Σ^+ analyzing power (A_N) as it was deduced in Sec. 7.2.2 is shown in Fig. 8.8 by the red down-pointing triangles together with the A_N of the Λ measured by COSY-TOF [26] and DISTO [25] at the same beam momentum. In the backward direction,

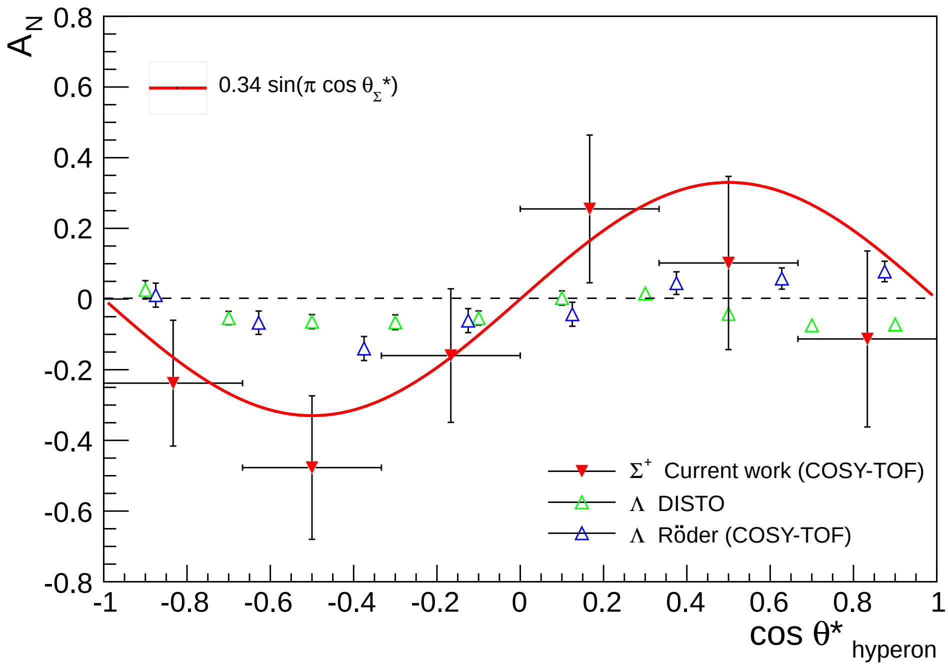

Figure 8.8 – Hyperons analyzing power as a function of hyperon polar angle in CMS. The red down-pointing triangles indicate the A_N of Σ^+ as the result of the current work; the green and blue up-pointing triangles are the A_N of Λ from the DISTO [25] and the COSY-TOF [26] measurements, respectively.

$\cos\theta^*_{hyperon} = -1$, the analyzing power of both hyperons is zero, while in the forward direction, $\cos\theta^*_{hyperon} = +1$, only A_N of Σ^+ is compatible with zero within the errors. At $\cos\theta^*_{hyperon} = +1$ the Λ analyzing power measured by COSY-TOF and DISTO is inconsistent with each other and in both cases deviates from zero. At $\cos\theta^*_{hyperon} = 0$ A_N changes sign.

The Σ^+ analyzing power appears to be a factor of two larger than that of Λ. The sine function fits the A_N of the Σ^+ distribution well in the whole range, as illustrated by the red line in Fig. 8.8, and has a maximum value of $(34 \pm 13)\%$.

8.5 Spin Transfer Coefficient

The Σ^+ polarization calculated for the two cases of beam and Σ^+ polarization pointing into the same ($P^{\uparrow\uparrow}$) and pointing into opposite ($P^{\uparrow\downarrow}$) hemispheres is shown in Fig. 8.9 (left) with the red down-pointing and the blue up-pointing triangles, respectively. The polarization of the Λ hyperons [26] deduced from the same data sample as used in the current work is shown for comparison in Fig. 8.9 (right). Due to the much larger statistics the P_N of Λ was evaluated for four samples as shown in the figure. The values of $P^{\uparrow\uparrow}$ and $P^{\downarrow\downarrow}$ as well as the values of $P^{\uparrow\downarrow}$ and $P^{\downarrow\uparrow}$ expected to be identical for symmetry reasons. The depolarization is defined by the difference of $P^{\uparrow\downarrow}$ and $P^{\uparrow\uparrow}$

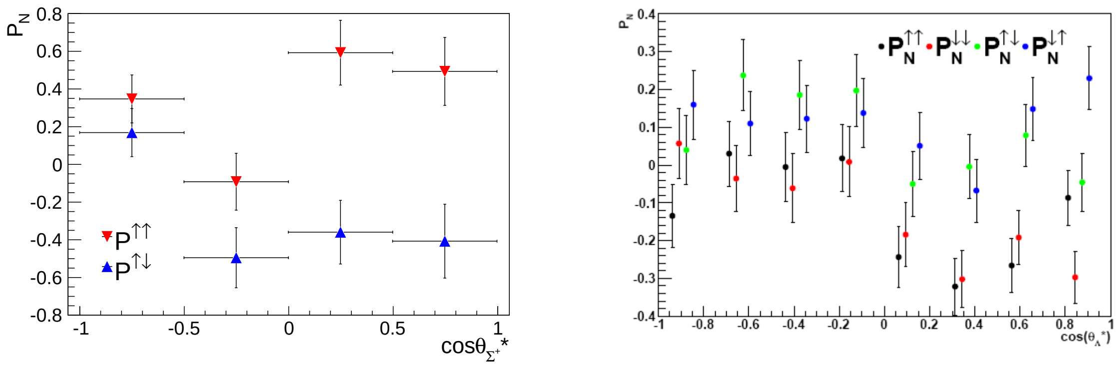

Figure 8.9 – The polarization of Σ^+ (left) and Λ (right) as a function of the CMS polar angle. Black and red points correspond to the sample with hyperon and beam polarization pointing into the same hemisphere ($P^{\uparrow\uparrow}$, $P^{\downarrow\downarrow}$); green and blue points are for the the polarization vectors pointing into opposite hemispheres ($P^{\uparrow\downarrow}$, $P^{\downarrow\uparrow}$). The right figure from Ref. [26].

as shown in Eq. (7.18). Comparing these quantities for Σ^+ and Λ, it can be therefore concluded that they result in an opposite sign of D_{NN} for the two hyperons.

The depolarization of hyperons as a function of $\cos\theta^*_{hyperon}$ and the Feynman variable x_f is shown in Figs. 8.10, 8.11. The red down-pointing triangles denotes the Σ^+

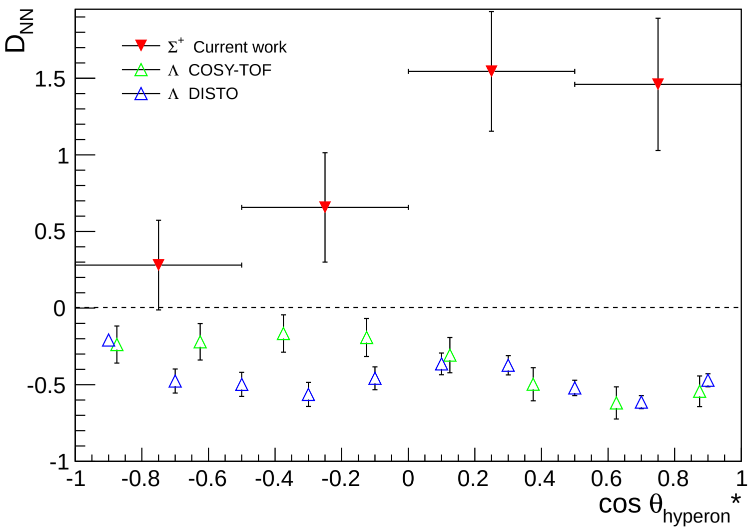

Figure 8.10 – Depolarization as a function of hyperon polar angle in the CMS. The red down-pointing triangles indicate the D_{NN} of Σ^+ obtained in the current work; the green and blue up-pointing triangles are the D_{NN} of Λ from the DISTO [25] and the COSY-TOF [26] measurements, respectively.

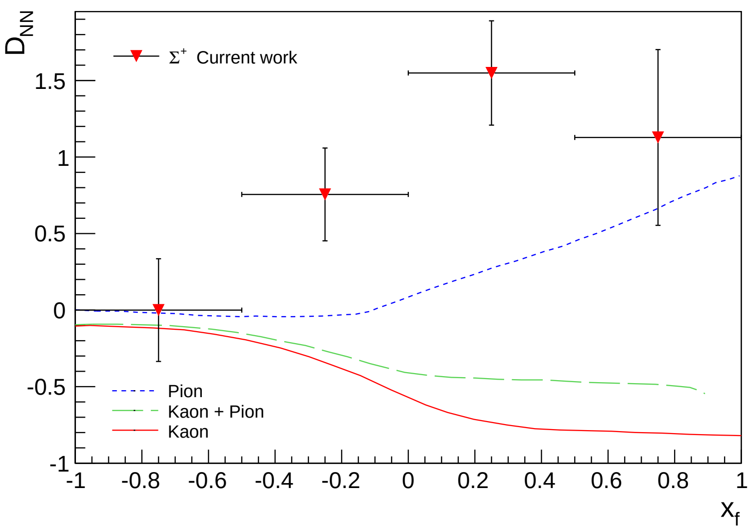

Figure 8.11 – Σ^+ depolarization as a function of the Feynman variable x_f. The lines represent the model calculation by Laget (Sec. 1.4.4). The blue short-dashed and red solid lines indicate pure pion exchange and kaon exchange, respectively, the green long-dashed line represents the mixed pion and kaon exchange.

depolarization while green and blue up-pointing triangles shows the D_{NN} of Λ measured by DISTO [25] and COSY-TOF [26], respectively. The allowed range of D_{NN} is limited to $[-1, 1]$, however some data points are outside of this range which is an indication of a systematic contribution not taken into account in the present analysis.

In the backward direction ($x_f \simeq -1$, $\cos\theta^*_{hyperon} \simeq -1$) the measured spin transfer is consistent with zero. This is well explained by the fact that the hyperon in this case is more connected with unpolarized target proton. In the forward direction ($x_f \simeq +1$, $\cos\theta^*_{hyp} \simeq +1$) D_{NN} is large and positive ($D_{NN} \simeq +1$) for Σ^+. According to the Laget model [2] (see also Sec. 1.4.4) this clearly indicates the dominant pion exchange in the production mechanism as illustrated by the blue short-dashed line in Fig. 8.11. The Λ depolarization is, however, negative in the forward region with a value of about -0.5 which can be interpreted as a result of mixed pion and kaon exchange shown by the green long-dashed line.

The theoretical interpretation on the basis of the Laget model should be taken with a caveat since it misses an important ingredient of the production mechanism, namely the resonance contribution. As was shown from the analysis of the Dalitz plot, N^* resonances play a significant role in associated strangeness production and should, therefore, be included in the theoretical models.

Summary and Conclusion

In 2010 the first physical experiment with the upgraded COSY-TOF detector was performed. To study the hyperon production a polarized proton beam at momentum $p = 2.95$ CeV/c was focused on a liquid hydrogen target. In this work the reaction $\vec{p}p \to pK^0\Sigma^+$ was investigated including polarization observables. The $pK^0\Sigma^+$ final state was identified based on the analysis of the delayed decays of the strange hadrons $K_s \to \pi^+\pi^-$ and $\Sigma^+ \to p\pi^0$, $n\pi^+$. Independent of the Σ^+ decay mode, this results in four charged particle tracks which need to be detected by the COSY-TOF detector. Two track reconstruction algorithms, the Global Track Finder and the Hough Track Finder were tested. Both of them use hit information from all subdetectors including the newly installed Silicon Quirl Tracker SQT and Straw Tube Tracker STT. The developed Global Track Finder algorithm is fast and efficient for two-track events and can be used for online reconstruction of elastic events. Events with higher track multiplicity are more efficiently reconstructed by the Hough Track Finder algorithm.

To achieve the best possible precision in the reconstruction of the track parameters the whole detector setup was calibrated. Most attention was devoted to the calibration of the SQT and the STT since they provide the most accurate hit information. Both the position and the orientation of the SQT and of each double-layer of the STT were adjusted. With these correction the "TDC-to-radius" curve for each single straw tube was obtained.

The parameters of the target and the polarized proton beam were determined from the analysis of elastic scattering events $\vec{p}p \to pp$. Due to the excellent tracking capability of the SQT and the STT the interaction point coordinate (x,y,z) of each scattering process is determined with a precision $(435 \pm 1,\, 444 \pm 1,\, 569 \pm 5)\ \mu m$. The polarization of the proton beam is deduced to be $(61.5 \pm 1.2)\%$.

Events satisfying the topology and the kinematic condition of the reaction $\vec{p}p \to pK^0\Sigma^+$ were selected from the collected data and analyzed. Two new reconstruction algorithms of the reaction $\vec{p}p \to pK^0\Sigma^+$ were developed. The combination of these two algorithms based on the tracking information of the new subdetectors SQT and STT yield a reconstruction efficiency $\varepsilon_{reco} = 0.027 \pm 0.001$ which is more than two times better than that of previous COSY-TOF measurements.

A new COSY-TOF analysis framework was developed. It incorporates the best features of modern analysis frameworks and allows for straightforward implementation of reconstruction and analysis algorithms.

To control the reconstruction and analysis procedure, Monte Carlo simulations were used. To achieve that, the existing TOFMC simulation software was extended by implementing the new subdetectors and by adding detector inefficiencies to obtain a more realistic detector response. An interface for EvtGen as an alternative particle generator was added to gain more flexibility in the generation of angular distributions.

From about one week of data taking 905 events of the reaction $\vec{p}p \to pK^0\Sigma^+$ were reconstructed. The fraction of background in this data sample is estimated to be at most 5.9%. Based on this, the total cross section of the reaction $\vec{p}p \to pK^0\Sigma^+$ was determined to be $\sigma = (2.95 \pm 0.11_{stat} \pm 0.22_{syst})\ \mu b$. This result is consistent with the energy dependence of the total cross section for this reaction measured by previous experiments. Within the error it confirms a previous COSY-TOF measurement at the same beam momentum. All total cross section data together are well reproduced by the so-called resonance model.

The Dalitz plot of the $pK^0\Sigma^+$ final state was analyzed. The $K^0\Sigma^+$ mass spectrum shows a clear enhancement at low masses. This can be interpreted as a significant contribution of nucleon resonances to the production mechanism. Under the assumption that only a single resonance contributes, the best agreement is obtained for a contribution of the N(1710) P_{11} resonance. Very different from the $p\Lambda$ case, a strongly attractive $p\Sigma^+$ final state interaction is clearly excluded due to the non-observation of an enhancement at low $p\Sigma^+$ masses.

For the first time, the polarization P_N of the Σ^+ hyperon in the reaction $\vec{p}p \to pK^0\Sigma^+$ was determined. For that the spin-average beam was used. Within the errors the obtained Σ^+ polarization as a function of the transverse momentum p_t is in agrement with high energy data from inclusive measurements. Σ^+ polarization as a function of $\cos\theta^*_{\Sigma^+}$ was compared with Λ hyperon polarization at the same conditions.

For the first time, the analyzing power A_N of the Σ^+ hyperon was deduced. As a function of $\cos\theta^*_{\Sigma^+}$ it has a sine-like distribution with an amplitude of $(34 \pm 13)\%$.

Furthermore, the spin transfer coefficient D_{NN} of the Σ^+ hyperon was determined. At large Σ^+ backward center-of-mass momentum the value of D_{NN} is compatible with zero while at large Σ^+ forward center-of-mass momentum it is $+1$ within the errors. Based on the model of Laget the found behavior requires dominant pion exchange in the production mechanism.

Addendum

Add. 1 Kinematics of $K_s \to \pi^+\pi^-$ Decay

Let use

$$\vec{p'}_K = \begin{pmatrix} 0 \\ 0 \\ p_K \end{pmatrix}, \quad \vec{p'}_{\pi^+} = \begin{pmatrix} p_0 \sin\theta' \\ 0 \\ p_0 \cos\theta' \end{pmatrix}, \quad \vec{p'}_{\pi^-} = \begin{pmatrix} -p_0 \sin\theta' \\ 0 \\ -p_0 \cos\theta' \end{pmatrix} \tag{.1}$$

as the momenta of the K_s, π^+ and π^- in the CMS. Here $p_0 = \sqrt{m_K^2/4 - m_\pi^2}$. The Lorentz transformation boosts the pions momenta in the laboratory frame as follow:

$$\vec{p}_{\pi^+} = \begin{pmatrix} p_0 \sin\theta' \\ 0 \\ \gamma(p_0 \cos\theta' + \beta m_K/2) \end{pmatrix}, \quad \vec{p}_{\pi^-} = \begin{pmatrix} -p_0 \sin\theta' \\ 0 \\ \gamma(-p_0 \cos\theta' + \beta m_K/2) \end{pmatrix} \tag{.2}$$

The tangent of the pion lab angle is defined as:

$$\tan\theta_{\pi^+} = \frac{p_{\pi^+ x}}{p_{\pi^+ z}}, \qquad \tan\theta_{\pi^-} = \frac{p_{\pi^- x}}{p_{\pi^- z}} \tag{.3}$$

Solution of this system gives:

$$(\beta\gamma)^2_{1/2} = -\frac{AB + A - C}{2A} \pm \sqrt{\left(\frac{AB + A - C}{2A}\right)^2 + \frac{C}{A}} \tag{.4}$$

where A,B,C are defined as:

$$\begin{aligned} A &= \left(\frac{m_K}{p_0}\right)^2 \\ B &= \frac{1}{4}\left(\cot\theta_{\pi^+} + \cot\theta_{\pi^-}\right)^2 \\ C &= \left(\cot\theta_{\pi^+} - \cot\theta_{\pi^-}\right)^2 \end{aligned} \tag{.5}$$

Then the K_s momentum is given as: $p_K = \beta\gamma m_K$

Add. 2 Example of the Analysis Macro in the COSY-TOF Analysis Framework

```
void run(Int_t se=0,Int_t ee=1000000){  // setting the range of analyzed events
  TofRunAna *analysis = new TofRunAna(0);      // creating an object of the
                                               // analysis manager
  analysis->SetInputFile("detresponce.root"); // adding input file
  analysis->SetOutputFile("events.root");      // adding output file

  TVector3 pbeam = TVector3(0,0,2.95);         // setting the beam momentum
  Double_t accuparam[] = {0.2,2.8,220,-40,40,160}; // setting the parameters of
                                          // Hough space

  TofHitFinderTask *hitfinder = new TofHitFinderTask(0); // creating an object
                                          // of the hit finder task
  hitfinder->SetSttCalibFile("TDCradiuscalib.root");     //
  hitfinder->SetSttCorrFile("STTposcorrection.root");    // adding calibration
                                          // files
  analysis->AddTask(hitfinder);           // adding hit finder task
                                          // to the analysis manager

  TofTrackFinderH *houghFinder = new TofTrackFinderH(accuparam); //
                                          // Hough track finder
  TofTrackFinderHTask *trackfinder = new TofTrackFinderHTask(houghFinder,0);
  analysis->AddTask(trackfinder);

  TofTrackFitterTask *trackfitter = new TofTrackFitterTask(0);  //
                                          // track fitter task
  analysis->AddTask(trackfitter);

  TofHitFinderTask *hitassigner = new TofHitFinderTask(*hitfinder);
                                          // hit finder task to assign pixel hits
  analysis->AddTask(hitassigner);

  TofEventFinderTask *eventfinder = new TofEventFinderTask(0,pbeam,2); //
                                          // event  finder task
  analysis->AddTask(eventfinder);

  TofEventGeomFitterTask *geomfitter = new TofEventGeomFitterTask(0); //
                                          // geometrical fitter task
  analysis->AddTask(geomfitter);

  TofEventKinKFitterTask *kinfitter = new TofEventKinKFitterTask(0);  //
                                          // kinematical fitter task
  analysis->AddTask(kinfitter);

  analysis->Init();      // initialization of all tasks
  analysis->Run(se,ee);  // executing all task for specified range of events
}
```

Add. 3 Solution of Eq. (6.7)

$$l = \frac{N}{\left((-p_b + p_{K_z})\,y_p - p_{K_y} z_p\right) x_{ch} + \left((p_b - p_{K_z})\,x_p + p_{K_x} z_p\right) y_{ch} + z_{ch}\left(p_{K_y} x_p - p_{K_x} y_p\right)}$$

$$p_p = \frac{1}{D}\Big(\left((V_z - A_z)\,p_{K_y} - (p_b - p_{K_z})\,(A_y - V_y)\right) x_{ch} + ((-V_z + A_z)\,p_{K_x} + (p_b - p_{K_z})\,(A_x - V_x)) \times y_{ch} + \left((-A_y + V_y)\,p_{K_x} + p_{K_y}\,(A_x - V_x)\right) z_{ch}\Big)$$

$$p_\Sigma = \frac{N}{D}$$

where:

$$N = -\Big(((b^2 {z_{ch}}^2 + (-V_z + A_z)^2){p_{K_y}}^2 + 2\,(p_b - p_{K_z})((-V_z + A_z)A_y + (V_z - A_z)V_y + b^2 z_{ch} y_{ch})p_{K_y} + (p_b - p_{K_z})^2(-2\,A_y V_y + {y_{ch}}^2 b^2 + {V_y}^2 + {A_y}^2)){x_p}^2 + ((((-2\,b^2 {z_{ch}}^2 - 2\,(-V_z + A_z)^2)p_{K_y} - 2\,(p_b - p_{K_z})((-V_z + A_z)A_y + (V_z - A_z)V_y + b^2 z_{ch} y_{ch}))p_{K_x} - 2\,(p_b - p_{K_z})(((-V_z + A_z)A_x + (V_z - A_z)V_x + b^2 z_{ch} x_{ch})p_{K_y} + ((A_y - V_y)A_x + V_x V_y + b^2 y_{ch} x_{ch} - A_y V_x)(p_b - p_{K_z})))y_p - 2\,z_p((((V_z - A_z)A_y + (-V_z + A_z)V_y - b^2 z_{ch} y_{ch})p_{K_y} - (-2\,A_y V_y + {y_{ch}}^2 b^2 + {V_y}^2 + {A_y}^2)(p_b - p_{K_z}))p_{K_x} + p_{K_y}(((-V_z + A_z)A_x + (V_z - A_z)V_x + b^2 z_{ch} x_{ch})p_{K_y} + ((A_y - V_y)A_x + V_x V_y + b^2 y_{ch} x_{ch} - A_y V_x) \times (p_b - p_{K_z}))))x_p + ((b^2 {z_{ch}}^2 + (-V_z + A_z)^2){p_{K_x}}^2 + 2\,(p_b - p_{K_z})((-V_z + A_z)A_x + (V_z - A_z)V_x + b^2 z_{ch} x_{ch})p_{K_x} + (p_b - p_{K_z})^2({V_x}^2 - 2\,A_x V_x + {x_{ch}}^2 b^2 + {A_x}^2)){y_p}^2 + 2\,z_p((((V_z - A_z)A_y + (-V_z + A_z)V_y - b^2 z_{ch} y_{ch}){p_{K_x}}^2 + (((-V_z + A_z)A_x + (V_z - A_z)V_x + b^2 z_{ch} x_{ch})p_{K_y} - ((A_y - V_y)A_x + V_x V_y + b^2 y_{ch} x_{ch} - A_y V_x)(p_b - p_{K_z}))p_{K_x} + p_{K_y}({V_x}^2 - 2\,A_x V_x + {x_{ch}}^2 b^2 + {A_x}^2)(p_b - p_{K_z}))y_p + {z_p}^2((-2\,A_y V_y + {y_{ch}}^2 b^2 + {V_y}^2 + {A_y}^2){p_{K_x}}^2 - 2\,((A_y - V_y)A_x + V_x V_y + b^2 y_{ch} x_{ch} - A_y V_x)p_{K_y} p_{K_x} + {p_{K_y}}^2({V_x}^2 - 2\,A_x V_x + {x_{ch}}^2 b^2 + {A_x}^2)))\Big)^{1/2}$$

$$D = ((-V_z + A_z)\,y_p - z_p\,(A_y - V_y))\,x_{ch} + ((V_z - A_z)\,x_p + z_p\,(A_x - V_x))\,y_{ch} - ((-A_y + V_y)\,x_p + y_p\,(A_x - V_x))\,z_{ch}$$

Add. 4 Data Tables

$m^2_{K^0\Sigma^+}$	N/AE	$\Delta N/AE$	$m^2_{K^0\Sigma^+}$	N/AE	$\Delta N/AE$	$m^2_{K^0\Sigma^+}$	N/AE	$\Delta N/AE$
2.848	18	4.24	2.999	42.33	6.51	3.151	31.82	5.64
2.862	42.55	6.52	3.013	45.55	6.75	3.164	42.1	6.49
2.876	42.16	6.49	3.027	48.67	6.98	3.178	20.97	4.58
2.889	56.6	7.52	3.041	52.26	7.23	3.192	31.64	5.62
2.903	63.25	7.95	3.054	50.45	7.1	3.206	26.83	5.18
2.917	68.73	8.29	3.068	57.92	7.61	3.219	12.89	3.59
2.931	60.89	7.8	3.082	39.47	6.28	3.233	12.6	3.55
2.944	55.48	7.45	3.096	48.32	6.95	3.247	8.31	2.88
2.958	56.25	7.5	3.109	44.14	6.64	3.261	11.46	3.39
2.972	60.03	7.75	3.123	42.52	6.52	3.274	4	2
2.986	50.14	7.08	3.137	35.64	5.97			

Table I – Projections of the Dalitz plot on the $K^0\Sigma^+$ axis.

$m^2_{p\Sigma^+}$	N/AE	$\Delta N/AE$	$m^2_{p\Sigma^+}$	N/AE	$\Delta N/AE$	$m^2_{p\Sigma^+}$	N/AE	$\Delta N/AE$
4.541	8	2.83	4.736	45.65	6.76	4.931	55.34	7.44
4.557	18	4.24	4.752	43.72	6.61	4.947	42.42	6.51
4.573	12.44	3.53	4.768	56.52	7.52	4.963	41.69	6.46
4.589	4.799	2.19	4.784	37.09	6.09	4.979	56.07	7.49
4.606	14.24	3.77	4.801	49.09	7.01	4.996	47.59	6.9
4.622	26.91	5.19	4.817	45.86	6.77	5.012	61.03	7.81
4.638	26.82	5.18	4.833	38.38	6.19	5.028	53.01	7.28
4.654	45.94	6.78	4.849	42.55	6.52	5.044	42.86	6.55
4.671	33.14	5.76	4.866	52.82	7.27	5.061	31.24	5.59
4.687	24.16	4.91	4.882	46.61	6.83	5.077	16	4
4.703	32.52	5.7	4.898	29.44	5.43			
4.719	48.19	6.94	4.914	53.87	7.34			

Table II – Projections of the Dalitz plot on the $p\Sigma^+$ axis.

$\cos\theta_p^*$	N/AE	$\Delta N/AE$	$\cos\theta_p^*$	N/AE	$\Delta N/AE$	$\cos\theta_p^*$	N/AE	$\Delta N/AE$
-0.98	25.79	5.08	-0.3	23.3	4.83	0.38	29.84	5.46
-0.94	34.28	5.85	-0.26	21.58	4.65	0.42	27.73	5.27
-0.9	26.41	5.14	-0.22	21.07	4.59	0.46	26.15	5.11
-0.86	27.47	5.24	-0.18	19.73	4.44	0.5	25.9	5.09
-0.82	23.2	4.82	-0.14	26.69	5.17	0.54	27.37	5.23
-0.78	31.49	5.61	-0.1	14.67	3.83	0.58	22.87	4.78
-0.74	19.31	4.39	-0.06	27.52	5.25	0.62	39.93	6.32
-0.7	37.51	6.12	-0.02	21.43	4.63	0.66	24.72	4.97
-0.66	26.09	5.11	0.02	25.08	5.01	0.7	30.36	5.51
-0.62	26.55	5.15	0.06	31.43	5.61	0.74	26.16	5.11
-0.58	10.86	3.3	0.1	26.27	5.13	0.78	35.18	5.93
-0.54	24.72	4.97	0.14	28.1	5.3	0.82	25.04	5
-0.5	16.92	4.11	0.18	33.88	5.82	0.86	22.36	4.73
-0.46	22.92	4.79	0.22	22.21	4.71	0.9	32.58	5.71
-0.42	21.4	4.63	0.26	26.88	5.19	0.94	25	5
-0.38	25.92	5.09	0.3	35.11	5.93	0.98	34	5.83
-0.34	30.63	5.53	0.34	20.97	4.58			

Table III – Angular distribution of p in the CMS.

$\cos\theta_{K_s}^*$	N/AE	$\Delta N/AE$	$\cos\theta_{K_s}^*$	N/AE	$\Delta N/AE$	$\cos\theta_{K_s}^*$	N/AE	$\Delta N/AE$
-0.98	65.08	8.07	-0.3	32.05	5.66	0.38	28.49	5.34
-0.94	35.52	5.96	-0.26	35.61	5.97	0.42	30.21	5.5
-0.9	67.51	8.22	-0.22	25.91	5.09	0.46	18.67	4.32
-0.86	49.39	7.03	-0.18	31.42	5.61	0.5	26.2	5.12
-0.82	51.6	7.18	-0.14	13.53	3.68	0.54	23.73	4.87
-0.78	42.46	6.52	-0.1	21.21	4.61	0.58	21.77	4.67
-0.74	58.81	7.67	-0.06	32.85	5.73	0.62	34.9	5.91
-0.7	48.55	6.97	-0.02	23.06	4.8	0.66	24.64	4.96
-0.66	41.83	6.47	0.02	33.46	5.78	0.7	40.98	6.4
-0.62	46.18	6.8	0.06	24.16	4.92	0.74	27.51	5.24
-0.58	38.19	6.18	0.1	26.72	5.17	0.78	30.52	5.52
-0.54	47.11	6.86	0.14	23.22	4.82	0.82	44.13	6.64
-0.5	40.86	6.39	0.18	26.58	5.16	0.86	36.25	6.02
-0.46	39.71	6.3	0.22	21.36	4.62	0.9	34.46	5.87
-0.42	39.46	6.28	0.26	17.69	4.21	0.94	29.92	5.47
-0.38	21.72	4.66	0.3	20.68	4.55	0.98	28.41	5.33
-0.34	14.41	3.8	0.34	21.7	4.66			

Table IV – Angular distribution of K_s in the CMS.

$\cos\theta^*_{\Sigma^+}$	N/AE	$\Delta N/AE$	$\cos\theta^*_{\Sigma^+}$	N/AE	$\Delta N/AE$	$\cos\theta^*_{\Sigma^+}$	N/AE	$\Delta N/AE$
-0.98	22.73	4.77	-0.3	39.51	6.29	0.38	26.75	5.17
-0.94	31.3	5.59	-0.26	20.49	4.53	0.42	26.58	5.16
-0.9	38.78	6.23	-0.22	26.63	5.16	0.46	30.41	5.51
-0.86	40.93	6.4	-0.18	14.86	3.85	0.5	26.54	5.15
-0.82	40.56	6.37	-0.14	24.88	4.99	0.54	23.13	4.81
-0.78	17.54	4.19	-0.1	35.03	5.92	0.58	26.33	5.13
-0.74	28.91	5.38	-0.06	28.37	5.33	0.62	34.34	5.86
-0.7	31.29	5.59	-0.02	27.44	5.24	0.66	38.19	6.18
-0.66	27.45	5.24	0.02	21.6	4.65	0.7	24.16	4.92
-0.62	32.05	5.66	0.06	26.11	5.11	0.74	34.32	5.86
-0.58	26.12	5.11	0.1	34	5.83	0.78	30.06	5.48
-0.54	27.1	5.21	0.14	21.15	4.6	0.82	47.34	6.88
-0.5	24.44	4.94	0.18	30.97	5.57	0.86	22.68	4.76
-0.46	12.59	3.55	0.22	13.86	3.72	0.9	42.58	6.53
-0.42	22.26	4.72	0.26	31.89	5.65	0.94	38.87	6.23
-0.38	25.35	5.04	0.3	14.16	3.76	0.98	34.52	5.88
-0.34	22.82	4.78	0.34	27.6	5.25			

Table V – Angular distribution of Σ^+ in the CMS.

$\cos\theta^*_{\Sigma^+}$	P_N	ΔP_N	$\cos\theta^*_{\Sigma^+}$	P_N	ΔP_N	$\cos\theta^*_{\Sigma^+}$	P_N	ΔP_N
-0.83	0.2	0.11	-0.17	-0.15	0.13	0.5	0.21	0.16
-0.50	0	0.13	0.17	0.17	0.14	0.83	-0.06	0.17

Table VI – Polarization P_N of the Σ^+ hyperon as a function of its CMS polar angle.

x_f	P_N	ΔP_N	x_f	P_N	ΔP_N	x_f	P_N	ΔP_N
-0.83	0.29	0.13	-0.17	-0.27	0.12	0.5	0.14	0.15
-0.50	0.12	0.12	0.17	0.03	0.13	0.83	0.16	0.28

Table VII – Polarization P_N of the Σ^+ hyperon as a function of the Feynman variable x_f.

$\cos\theta^*_{\Sigma+}$	A_N	ΔA_N	$\cos\theta^*_{\Sigma+}$	A_N	ΔA_N	$\cos\theta^*_{\Sigma+}$	A_N	ΔA_N
-0.83	-0.238	0.178	-0.17	-0.16	0.189	0.5	0.102	0.245
-0.50	-0.477	0.203	0.17	0.255	0.209	0.83	-0.113	0.249

Table VIII – Analyzing power A_N of the Σ^+ hyperon as a function of its CMS polar angle.

x_f	A_N	ΔA_N	x_f	A_N	ΔA_N	x_f	A_N	ΔA_N
-0.83	-0.358	0.211	-0.17	0.060	0.169	0.5	0.128	0.222
-0.50	-0.679	0.197	0.17	0.215	0.191	0.83	-0.147	0.374

Table IX – Analyzing power A_N of the Σ^+ hyperon as a function of the Feynman variable x_f.

$\cos\theta^*_{\Sigma+}$	D_{NN}	ΔD_{NN}	$\cos\theta^*_{\Sigma+}$	D_{NN}	ΔD_{NN}
-0.75	0.28	0.29	0.25	1.54	0.39
-0.25	0.65	0.36	0.75	1.46	0.43

Table X – Spin transfer coefficient D_{NN} of the Σ^+ hyperon as a function of its CMS polar angle.

x_f	D_{NN}	ΔD_{NN}	x_f	D_{NN}	ΔD_{NN}
-0.75	0	0.34	0.25	1.54	0.34
-0.25	0.75	0.30	0.75	1.12	0.57

Table XI – Spin transfer coefficient D_{NN} of the Σ^+ hyperon as a function of the Feynman variable x_f.

Legend of Acronyms

A_N	Analyzing power
D_{NN}	Depolarization
P_b	Beam polarization
P_N	Polarization
x_f	Feynman variable
CMS	Center of Mass System
COSY	Cooler Synchrotron
FSI	Final State Interactions
GTF	Global Track Finder
HTF	Hough Track Finder
N	Nucleon
ndf	number of degrees of freedom
PWA	Partial Wave Analysis
QCD	Quantum Chromo Dynamics
SM	Standard Model
SQT	Silicon Quirl Tracker
STT	Straw Tube Tracker
TDC	Time Digital Converter
TOF	Time of Flight
Y	Hyperon

References

[1] E. Ferrari. *Phys. Rev. 120 988; Nuovo Cim. 15 652*, 1960. (Cited on pages 3, 129).

[2] J.M. Laget. Strangeness production in nucleon-nucleon collisions. *Phys. Lett. B 259 24*, 1991. (Cited on pages 3, 5, 13, 129, 139).

[3] A. Sibirtsev, K. Tsushima, W. Cassing, and A.W. Thomas. The role of the $P_{11}(1710)$ in the $NN \rightarrow N\Sigma K$ reaction. *Nucl.Phys.A646:427-443, arXiv:nucl-th/9810070v2*, Dec. 1998. (Cited on pages 3, 6).

[4] A. Deloff. *Nucl. Phys. A 505 583*, 1989. (Cited on page 3).

[5] G.Q. Li and C.M. Ko. *Phys. A 594 439*, 1995. (Cited on pages 4, 129, 130).

[6] A. Sibirtsev. *Phys. Lett. B 359 29*, 1995. (Cited on page 4).

[7] T. Yao. *Phys. Rev. 125 1048*, 1962. (Cited on page 4).

[8] J.Q. Wu and C.M. Ko. *Nucl. Phys. A 499 810*, 1989. (Cited on page 4).

[9] K. Tsushima, A. Sibirtsev, and A. W. Thomas. *Phys. Lett. B 390 29*, 1997. (Cited on pages 4, 6).

[10] A. Sibirtsev, K. Tsushima, and A.W. Thomas. A clue to the mechanism of ΛK^+ production in pp-reactions. *Phys. Lett. B 421 59*, 1998. (Cited on pages 4, 5, 6, 7).

[11] A.D. Martin. *Nucl. Phys. B 179 33*, 1981. (Cited on page 5).

[12] R.H. Dalitz, J. McGinley, C. Belyea, and S. Anthony. *Proc. Int. Conf. on hypernuclear and kaon physics Heidelberg ed. B.Povh.*, 1982. (Cited on page 5).

[13] A. Sibirtsev and W. Cassing. Strangeness production in proton-proton collisions. *arXiv:nucl-th/9802019v2*, Feb. 1998. (Cited on pages 5, 127, 128, 129, 130).

[14] R. Bilger et al. *Phys. Lett. B 420 217*, 1998. (Cited on pages 5, 15).

[15] S. Abd El-Samad et al. *Phys. Lett. B 632 27*, 2006. (Cited on pages 5, 15).

[16] K. Tsushima, S.W. Huang, and Amand Faessler. *Phys. Lett. B 337 (1994) 245; J. Phys. G21 (1995) 33; Australian. J. Phys. 50 (1997) 35.* (Cited on pages 5, 6).

[17] B.D. Lackey, M. Nayyar, and B.J. Owen. *arXiv:astro-ph/0507312; Phys. Rev. D 73 024021*, 2006. (Cited on page 7).

[18] H. Polinder, J. Haidenbauer, and U. G. Meissner. *arXiv:nucl-th/0605050; Nucl. Phys. A 779*, 2006. (Cited on page 7).

[19] J. Soffer. Is the riddle of the hyperon polariztion solved? *arXiv:hep-ph/9911373v1*, Nov. 1999. (Cited on page 7).

[20] B. Andersson et al. *Physics Reports 97 31 and references therein*, 1983. (Cited on page 8).

[21] J. Félix et al. *Phys. Rev. Lett. 76 22*, 1996. (Cited on page 8).

[22] T. De Grand et al. *Phys. Rev. Lett. D32 2445 and references therein*, 1986. (Cited on page 8).

[23] A. Bravar et al. *Phys. Rev. Lett. 75 3073*, 1995. (Cited on page 9).

[24] A. Bravar et al. *Phys. Rev. Lett. 78 4003*, 1997. (Cited on page 9).

[25] M. Maggiora. New results from DISTO for spin observables in exclusive hyperon production. *Nucl.Phys., A691:329335*, 2001. (Cited on pages 9, 136, 138, 139).

[26] M. Röder. Final state interaction and polarization variables in the reaction $\vec{p}p \to pK^+\Lambda$. *PhD thesis, Bochum*, 2011. (Cited on pages 9, 15, 23, 87, 93, 110, 121, 133, 135, 136, 137, 138, 139).

[27] A. Baldini et al. *Landolt-Börnstein, New Series, I/12b*, 1988. (Cited on pages 9, 128).

[28] M. Abdel-Bary et al. *Eur. Phys. J. A 48: 23, DOI: 10.1140/epja/i2012-12023-8*, 2012. (Cited on pages 9, 10, 15, 128, 133).

[29] E. Ferrari and S. Serio. *Phys. Rev. 167, 1298*, 1968. (Cited on page 9).

[30] K. Tsushima, A. Sibirtsev, A. W. Thomas, and G. Q. Li. Resonance model study of kaon production in baryon-baryon reactions for heavy-ion collisions. *Phys. Rev. C 59 1*, Jan 1999. (Cited on pages 10, 129).

[31] R.H. Dalitz. *Phil. Mag. Series 7, 44: 357, 1068*, 1953. (Cited on page 10).

[32] C. Wilkinson et al. Polarization and magnetic moment of the Σ^+ hyeron. *Phys. Rev. Let. 58, 855*, 1987. (Cited on pages 11, 12, 134).

[33] A. Morelos et al. *Phys. Rev. Lett. 71 14*, 1993. (Cited on pages 11, 134).

[34] A. Morelos. Measurement of the polarization and magnetic moment of Σ^+ and $\bar{\Sigma}^-$ hyperons. *Thesis*, 1992. (Cited on page 11).

[35] B. Lundberg et al. *Phys. Rev. D40, 3557*, 1989. (Cited on page 12).

[36] E.J. Ramberg et al. *Phys. Lett. B 338 403-408.*, 1994. (Cited on page 12).

[37] J. Duryea et al. *Phys. Rev. Lett. 67, 1193*, 1991. (Cited on page 12).

[38] Homer A. Neal and Eduard de la Cruz Burelo. Hyperon polarization in a quark-quark scattering model. *arXiv:hep-ph/0602079v1*, Feb 2006. (Cited on page 12).

[39] G.L. Kane et al. *Phys. Rev. Lett., 41, 1689*, 1978. (Cited on page 11).

[40] P. Cea et al. *Phys. Lett. B, 209, 333*, 1988. (Cited on page 11).

[41] R. Lawall. Messung der Reaktion $\gamma p \rightarrow K^0\Sigma^+$ für Photonenergien bis 2.65 CeV mit dem SAPHIR-Detector an ELSA. *PhD thesis, Bonn*, Nov. 2003. (Cited on page 12).

[42] S. Goers. Measurement of $\gamma p \rightarrow K^0\Sigma^+$ at photonenergies up to 1.55 GeV. *Phys. Lett. B 464 331*, 1999. (Cited on page 12).

[43] J. Caro Ramon, N. Kaiser, S. Wetzel, and W. Weise. Chiral SU(3) dynamics with coupled channels: Inclusion of p-wave multipoles. *arXiv:nucl-th/9912053v1.* (Cited on page 12).

[44] F. Balestra et al. Spin Observables for Λ Hyperons in pp scattering. *Nucl.Phys. B 93 58*, 2001. (Cited on page 13).

[45] The COSY-TOF Collaboration. Strangeness physiscs at COSY-TOF. `www2.fz-juelich.de/ikp/publications/PAC34/TOF_perspectives_final.pdf`. (Cited on pages 14, 133).

[46] S. Abd El-Samad et al. Influence of N*-resonances on hyperon production in the channel $pp \to K^+\Lambda p$ at 2.95, 3.20 and 3.30 GeV/c beam momentum. *Phys. Lett. B 688 142*, 2010. (Cited on page 15).

[47] W. Schroeder et al. Hyperon production in proton-proton collision at the time of flight spectrometer COSY-TOF. *Eur. Phys. J. A vol. 18 347-349*, 2003. (Cited on page 15).

[48] K. Ehrhardt. Measurement of the Reaction $pp \to pK^+\Lambda$ and its Analysis with a new Analysis Program: typeCase. *PhD thesis, Tübingen*, 2011. (Cited on page 15).

[49] M. Abdel-Bary et al. Production of Λ and Σ^0 hyperons in proton-proton collisions . *Eur. Phys. J. A 46 27*, 2010. (Cited on page 15).

[50] M. Abdel-Bary et al. Evidence for a narrow resonance at 1530 MeV/c^2 in the K^0p - system of the reaction $pp \to \Sigma^+K^0p$ from the COSY-TOF experiment. *Phys. Lett. B595 127*, 2004. (Cited on page 15).

[51] M. Abdel-Bary et al. Improved study of a possible Θ^+ production in the $pp \to pK^0\Sigma^+$ reaction with the COSY-TOF spectrometer. *Phys. Lett. B649 252*, 2007. (Cited on page 15).

[52] L. Karsch. Untersuchungen zu den Reaktionen $pp \to nK^+\Sigma^+$ und $pp \to pK^0\Sigma^+$. *PhD thesis, Dresden University of Technology*, 2005. (Cited on page 15).

[53] M. Wagner. Assoziierte Strangeness-Produktion in der Reaktion $pp \to K^0\Sigma^+p$ am COSY-Flugzeitspektrometer. *PhD thesis, University of Erlangen-Nuernberg*, 2002. (Cited on page 15).

[54] C. Pizzolotto. Measurement of lambda polarisation observables at the COSY-TOF spectrometer. *PhD thesis, Universität Erlangen*, 2007. (Cited on pages 15, 135).

[55] R. Maier. *Nucl. Instr. and Meth. A390, 1 ; Nuclear Physics News International 7, 5; R. Maier et al., Nucl. Phys. A626, 395c*, 1997. (Cited on page 17).

[56] The COSY-TOF Collaboration. AutoCAD drawings of the TOF setup. `http://www2.fz-juelich.de/ikp/COSY-TOF/detektor/index_e.html`. (Cited on page 19).

[57] W. Gast. The silicon microstrip quirl telescope. *FZ-Jülich IKP Annual report*, 2008. (Cited on page 21).

[58] The COSY-TOF Collaboration. Commissioning of the COSY-TOF Straw Tracker. *FZ-Jülich IKP Annual reports highlights p. 10*, 2008. (Cited on page 23).

[59] Application Software Group. Geant 3.2.1 detector description and simulation tool. *CERN Program Library Long Writeup W5013*, 1993. (Cited on page 25).

[60] A. Ryd. Evtgen v00-10-02. *BAD 522 V6*, 2003. (Cited on pages 26, 30).

[61] R. Dzhygadlo et al. Implementation of the Silicon Quirl Telescop in the COSY-TOF Monte Carlo Program. *FZ-Jülich IKP Annual report*, 2009. (Cited on page 27).

[62] E.Borodina. Event Display and Online Control Package for the upgraded COSY-TOF Experiment. *FZ-Jülich IKP Annual report*, 2009. (Cited on page 31).

[63] E.Borodina. Online system for data monitoring, visualisation and control at the COSY-TOF experiment. *PhD dissertation, MIEM, Moscow*, 2012. (Cited on page 31).

[64] M. Tadel. ALICE ESD track visualization software. `http://root.cern.ch/root/html/tutorials/eve/alice_esd.C.html`. (Cited on page 31).

[65] R. Brun et al. An object-oriented data analysis framework. `http://root.cern.ch`. (Cited on pages 31, 77).

[66] R. Brun and F. Rademakers. g2root - converter. `http://linux.die.net/man/1/g2root`. (Cited on page 32).

[67] Peter Wintz. *Private communications.* (Cited on page 51).

[68] R. Dzhygadlo and A. Gillitzer. Global track finder for the upgraded COSY-TOF detector. *FZ-Jülich IKP Annual report*, 2010. (Cited on page 56).

[69] P.V.C. Hough. Method and means of recognizing complex patterns. *U.S Patent 3,069,654*, December 1962. (Cited on page 57).

[70] Richard O. Duda and Peter E. Hart. Use of the hough transformation to detect lines and curves in pictures. *Communications of the ACM, v.15 n.1, p.11-15*, Jan. 1972. (Cited on page 57).

[71] The COSY-TOF Collaboration. *COSY-TOF Jülich Internal Note*, July 2006. (Cited on pages 76, 78).

[72] Denis Bertini, Mohammad Al-Turany, Ilse Koenig, and Florian Uhlig. The FAIR simulation and analysis framework. *Journal of Physics: Conference Series 119*, 2008. (Cited on page 77).

[73] Ralph Castelijns. Tof-straw software. `http://www2.fz-juelich.de/ikp/COSY-TOF/manuals/index_e.html`. (Cited on page 78).

[74] Richard A. Arndt, Igor I. Strakovsky, and Ron L. Workman. Nucleon nucleon elastic scattering to 3 GeV. *Phys.Rev., C62:034005*, 2000. (Cited on pages 91, 93).

[75] V. Flaminio. Compilation of cross sections iii: p and $\overline{p}$ induced reactions. *CERN-HERA 84-10*, 1984. (Cited on page 109).

[76] E. Roderburg and D. Grzonka. *Private communications.* (Cited on page 114).

[77] J. Lach. Hyperons: Insights into the baryon structure. *FERMILAB-Conf-92/378*, 1992. (Cited on page 116).

[78] K. Nakamura et al. (Particle Data Group). Particle kinematics. *J. Phys. G 37, 075021*, 2010. (Cited on pages 117, 131).

[79] E. Byckling and K. Kajantie. Particle kinematics. *John Wiley and Sons, p. 163*, 1972. (Cited on page 129).

[80] A. Sibirtsev, J. Haidenbauer, H.-W. Hammer, and U.-G. Meißner. *Eur. Phys. J. A 32, 229-241*, 2007. (Cited on page 129).

Acknowledgements

Here I would like to express my gratitude to the people who gave me unforgettable experience and made this thesis possible.

Firstly, I want to thank Jim Ritman for giving me opportunity to make my PhD in Forschungszentrum Jülich, and for his personal involvement into the most detailed parts of my work.

Especially, I would like to express my deeply-felt thanks to my supervisor Albrecht Gillitzer for his invaluable advising during this work, for his lectures on experimental methods and theory, and for increasing readability of my thesis.

I am grateful to Jens Bisplinghoff and Kai Brinkmann for being my supervisors from Bonn university.

Thank you to all members of the COSY-TOF collaboration, especially, to Eduard Roderburg, Juergen Uehlemann, Peter Wintz, Werner Gast, Norbert Paul, Dieter Grzonka, Wolfgang Eyrich, Ekaterina Borodina, Pawel Klaja, Florian Hauenstein for the analysis meetings and discussions. Peter and Florian, thank you for reading my thesis.

Thank you to Shasha Sibirtsev for discussion about Resonance Model.

Thank you very much to Kurt Kilian for his enthusiasm and useful and detailed discussions.

Thanks to Matthias Röder, my officemate, for numerous discussions and reading my thesis.

Also thank you to all my PANDA colleagues from FZ Jülich and beyond.

Finally, I want to thank my family for continued encouragement and support. There would be nothing without you).

And that the message to the universe)): Fil ar gobe ratu de, hli larm fe boru ke volar. Sif di gobe lu 327.